

**Modelling microbial processes of soil organic matter
mineralization and methane production**

by

Pablo Venegas Garcia

A thesis submitted in partial fulfillment of the requirements for the degree of

Doctor of Philosophy

in

Applied Mathematics

Department of Mathematical and Statistical Sciences

University of Alberta

Abstract

Increased anthropogenic greenhouse gas emissions have gained attention from researchers and world leaders due to the potential for global warming. Part of the primary greenhouse gas emitters come from the agriculture and oil and gas industrial sectors. The sources of two prioritized greenhouse gases, carbon dioxide and methane, are now the subject of extensive research because of the adverse effects of such gases on a global scale. Particularly, microbial biodegradation of organic compounds is under consideration due to microbial capacity to produce different greenhouse gases at high rates or scales, including carbon dioxide and methane, depending on environmental or soil features. For example, rapid soil organic matter (SOM) mineralization derived from increased microbial degradation activities due to labile substrate availability in soils can elevate atmospheric carbon dioxide in short periods. Also, under anaerobic conditions, specific microbial communities can slowly degrade hydrocarbons found in oil sand tailing ponds, increasing atmospheric methane concentrations over a long time.

In this thesis, we formulated data-validated mathematical models to estimate carbon dioxide and methane emissions from microbial organic matter biodegradation processes in soils. Under aerobic conditions, a base model captures the biodegradation kinetics of labile compounds and soil organic matter under carbon and nitrogen stoichiometric constraints. The model quantifies the necessary labile carbon-to-nitrogen to increase microbial SOM mineralization and time to achieve a maximum degradation rate for different nutrient-rich soils. An extended version of this model allows us

to include soil health indicators to understand the dynamic interaction between plant microbes and soils. Our theoretical results for this specific approach reveal a threshold for which the input of fertilizers would be needed for plant growth, providing insightful information that might benefit the agricultural sector for agricultural soil management. Considering anaerobic conditions, a mechanistic mathematical model allowed us to quantify hydrocarbon degradation kinetics and methane emissions from oil sands tailings. We collected experimental data to evaluate hydrocarbon degradation rates subject to different temperatures to capture a broad spectrum of degradation kinetics, which are required to incorporate the temperature variations in oil sands tailing ponds and end pit lakes into the model. Our results quantify the differences between the model's predictions and governmental reports, showing a significant discrepancy. Furthermore, the model predicts that hydrocarbon concentration in oil sands tailing ponds would reach a steady state when a constant input of tailings and diluents into ponds is assumed, implying a constant methane biogenesis rate.

Preface

The structure of this thesis is based on original research work encompassing Chapters 2-4. Part of these research efforts to build this thesis was conducted as part of collaborations with Hao Wang as a supervisory author through all chapters and Tariq Siddique as a supervisory author for Chapter 4. Now, Chapter 4 encompasses a critical multidisciplinary effort by distributing my research simultaneously into the experimental set-up, laboratory data collection, and mathematical modelling. Working closely with soil microbiology researchers in the laboratory allowed me to comprehend experimental circumstances and understand the methane biogenesis process from an empirical perspective, which is explicitly lost in theoretical research that relies only on the literature. In this way, my work gained a fundamental understanding of microbial methane formation that I use to bridge the gap between the biological and mathematical sciences to generate a mathematical model suitable for predicting methane emissions using a laboratory-verifiable mechanistic approach, which is unique.

Chapter 2 of this thesis is an original work that has been published as Pablo V. Garcia, Hao Wang. “A Data-Validated Stoichiometric Model for the Priming Effect”. *Bull Math Biol* 85, 53 (2023). Pablo V. Garcia was responsible for the model development, analysis and manuscript composition. Hao Wang was the supervisory author and assisted in the model development, and contributed to manuscript edits.

Chapter 3 of this thesis is an original work in a review process prior to publication as Pablo V. Garcia, Tianxu Wang and Hao Wang. “Rhizosphere dynamics under simplified soil health indicators”. Pablo V. Garcia was responsible for the model development, analysis and manuscript composition. Tianxu Wang was responsible for model analysis and manuscript edits. Hao Wang was the supervisory author and assisted with

the model development, and contributed to manuscript edits.

Chapter 4 of this thesis is an original work that will soon be submitted for publication as Pablo V. Garcia, Alsu Kuznetsova, Tariq Siddique and Hao Wang. “Temperature dependent mechanistic model to predict methane biogenesis from an oil sands tailings settling basin”. Pablo V. Garcia was responsible for laboratory work, experiment setup, sampling, data analysis, model development, numerical simulations, and manuscript composition. Alsu Kuznetsova assisted with the experiment setup and data analysis and contributed to manuscript edits. Tariq Siddique was a supervisory author who assisted in model conceptualization, model development, and experimental design and contributed to manuscript edits. Hao Wang was a supervisory author who assisted in model conceptualization and model development and contributed to manuscript edits.

To my family and friends.

Acknowledgements

I will start by thanking my parents, Claudia Moncerrat Garcia Irla and Saul Venegas Salgado, for all their support. I also want to thank my brothers Saul Venegas Garcia and Claudia Montserrat Venegas Garcia, whom I know I can count on, and Dr. Yuriy Salmaniw for his lifelong friendship and wisdom. To all my friends, including my biking friends, for their invaluable time and support, which have made Edmonton a place I can call home. I want especially to thank professor Hao Wang for providing me with support, guidance and courage to keep myself trying to reach new horizons. To professor Tariq Siddique, and all the laboratory crew, who showed me patience and guidance, allowing me to work closely with reality. To the Interdisciplinary Lab for Mathematical Ecology & Epidemiology (ILMEE) crew for keeping me engaged in academic work and allowing me to keep myself learning from others. Also, I want to thank Guillermina Garcia Avila for providing me with the artwork that displays briefly the nutrients cycle.

I want to also thank CONACyT for providing a financial support. To the University of Alberta and the Department of Mathematical and Statistical Sciences, which provided solid ground for my research. To my dear professors Thomas Hillen, Jay Newby, Gerda de Vries, and Mark Lewis, who have shared their knowledge. To Kimberly Wike-Budinski for carrying administrative management of the Collaborative Mathematical Biology Group (CMB) and sharing smiles. To all my friends and colleagues at the university.

Thank you, all of you.

Contents

1	Introduction	1
1.1	Motivation	1
1.2	Preliminaries	3
1.2.1	Redox potential	3
1.2.2	Canadian oil sands territories	4
1.2.3	Mathematical approach	5
1.3	Temperature-dependent methane biogenesis in fluid fine tailings experiments	6
1.4	Thesis overview	6
2	A Data-validated stoichiometric model for the priming effect	8
2.1	Introduction	8
2.2	Model formulation	10
2.3	Material and methods	14
2.3.1	Laboratory experiment	14
2.3.2	Data fitting	15
2.4	Numerical simulations	18
2.4.1	Sensitivity analysis	19
2.4.2	Numerical experiment: impact of Exogenous Labile C and N in SOM decomposition	20
2.4.3	Numerical experiment: positive and negative priming effect	23
2.5	Discussion	24
3	Rhizosphere dynamics under simplified soil health indicators	27
3.1	Introduction	27
3.2	Mathematical model	30
3.3	Model analysis	33
3.3.1	Positivity and boundedness	34
3.3.2	Equilibria	38
3.3.3	Stability analysis	40
3.3.4	Persistence-extinction criteria	44
3.4	Numerical experiments	47
3.4.1	Soil health	47
3.4.2	Bifurcation analysis	50
3.4.3	Rhizodeposition, mineralization and immobilization	54
3.5	Discussion	58

4	Temperature-dependent mechanistic model to predict methane biogenesis from an oil sands tailings settling basin	60
4.1	Introduction	60
4.2	Material and methods	63
4.2.1	Fluid fine tailings source	63
4.2.2	Experiment set up	63
4.2.3	Analytical measurements	64
4.2.4	Microbial analyses	65
4.2.5	Laboratory results	65
4.3	Mechanistic methane biogenesis model	69
4.3.1	Model development	69
4.3.2	Qualitative methane biogenesis predictors	73
4.4	Model validation	75
4.4.1	Data-fitting and parameter estimation	75
4.5	Numerical experiments	81
4.5.1	Predictions on measurable variables	81
4.5.2	Zero- and first-order kinetic model predictions revisited	84
4.5.3	Methane biogenesis simulations in OSTP and EPL	86
4.5.4	Comparison between reported methane emissions and model predictions in Alberta’s oil sands territories.	90
4.6	Discussion	91
5	Conclusion	97
5.1	Discussion of main results	97
5.2	Limitations and future work	99
	References	100

List of Tables

2.1	Experimental design. Table adapted from [14].	15
2.2	List of parameters used for the numerical simulation. H.S.C stands for half-saturation constant. C.I. stands for Confidence Interval.	16
2.3	Initial conditions.	16
3.1	Steady states and stability conditions summary. Each column represents the steady state $E_i = (B_i^*, C_i^*, N_i^*)$ and how each term is computed. If an expression is in terms of an equation, then the value must be computed implicitly. Otherwise, the value is given explicitly. The local asymptotically stable (L.A.S.) conditions are given in terms of variables defined in section 3.3.3.	44
3.2	List of parameters used for the numerical simulation. H.S.C. (S.H.I.) stands for half-saturation constant (soil health indicator). The plant's rhizodeposits depend on different soil features, including soil nutrients bioavailability, pH, temperature, moisture, etc. These delimiting rhizodeposits features are simplified in terms of free parameters but remain fixed through the simulations unless stated otherwise.	48
4.1	Zero-order HC kinetics table and function fit (Fitting). The rows below the K_0 kinetics (median) show median zero-order kinetics for different HC subsets T_τ^s , where τ is the temperature, and s is the number of HC spikes added. Zero-order HC kinetics for 10°C was estimated by modelling data adapted from [48] (see Fig.4.6). The last column contains the zero-order temperature-dependent functional representation.	89
4.2	First-order HC kinetics table and function fit (Fitting). The rows below the K_1 kinetics (median) show median first-order kinetics for different HC subsets T_τ^s , where τ is the temperature, and s is the number of HC spikes added. First-order HC kinetics for 10°C was calculated as in Table 4.1.	89
4.3	First-order mechanistic (FOM), zero- and first-order kinetic models cumulative methane predictions in MLSB during 2016-2017 using HC temperature-dependent kinetics and HC input assumption in previous years. The total methane reported from this period was 2182.1 t mol [47]. Each assumed year before 2016, assumes 60% of 2016 unrecovered diluent, simulating smaller-scale HC input. Methane predictions reach a fixed percentage of the cumulative methane reported by increasing the years of assumed HC input before 2016.	90

List of Figures

2.1	Data adapted from [14]. (Left panel): Cumulative CO ₂ emissions from four different soil treatments in the ninth day. (Right panel): Cumulative CO ₂ emissions over nine days for each experiment.	15
2.2	Model validation using the data adapted from [14] and parameters from Tables 2.1, 3.2, and 2.3. Each panel represents a different soil treatment. It is shown when labile C or N limits the CO ₂ emissions. The system is mostly C -limited because it is not considered an external sink of labile nutrients such as plants.	17
2.3	Numerical simulations of the model (2.6) and (2.9) using Tables 3.2, 2.3, and 2.1. (First column): Cumulative SOM decomposed and CO ₂ emissions. (Second column): CO ₂ production and percentage of SOM decomposed with respect to time. (Third and fourth column): Simulated microorganisms biomass subject to different SOM decomposition mechanisms.	18
2.4	Sensitivity Index (S.I.) for $u = 1 - \Gamma_i^j/C_s(0)$ for $i = \{0, 100\}$ and $j = \{0, 500\}$ of SOM decomposition when different treatments are considered. (Left panel): S.I. using parameters in Table 3.2. In this case, the system is C_s -Limited ($K_{f_s} < K_{g_s}N_s(0)/C_s(0)$). (Right panel): S.I. when the system is N_s -Limited, i.e., we choose K_{f_s} such that $K_{f_s} > K_{g_s}N_s(0)/C_s(0)$	20
2.5	Impact of adding an initial single dose of labile N and C to soils during SOM decomposition. (Left panel): Relative SOM decomposition increment when the combination of $C(0) = j$ and $N(0) = i$ is considered and compared to when only $C(0) = 500$ is added as $1 - \Gamma_i^j/\Gamma_0^{500}$. (Right panel): Different curves generated by $1 - \Gamma_i^j/\Gamma_0^{500}$ when $i \in [0, 30]$ and $j = \{0, 100, 200, \dots, 500\}$. The red line in both panels is given by $N(C) = C/25.83$ and represents an optimal C:N initial ratio to maximize SOM decomposition in terms of efficiency and is generated by a linear regression using the points (i, j) such that $ \Gamma_i^j - \Gamma_{30}^j < \varepsilon\Gamma_0^{500}$ for $\varepsilon = 0.1$	21
2.6	Optimal initial C:N ratio to decompose SOM efficiently with respect to the SOM nutrient-richness ratio. The experimental reference is $C_s(0) : N_s(0) = 15$, and the labile C:N ratio for labile substrates in the laboratory experiment was approximately 4.5. The optimal labile C:N ratio is constant for nutrient-rich soils, and it increases linearly for nutrient-poor soils.	22

2.7	(Left panel): Time expected for the priming effect to occur, i.e., when microbial communities decompose SOM at its maximum rate. (Right panel): Percentage of decomposed SOM by different treatments by the ninth day.	23
2.8	Difference of cumulative decomposed SOM between soil treated with $C(0) = 500, N(0) = 0$ (Γ_0^{500}), and with $C(0) = 500, N(0) = 20$ (Γ_{20}^{500}) varying K_{f_s} (left panel) and K_{g_s} (right panel) on the ninth day. The parameters are taken as in Table 3.2. The initial conditions for other variables are considered as in Table 2.3. The model is capable to reproduce positive (negative) priming effects depending on the value for the half-saturation constant for f_s and g_s	24
3.1	Numerical simulations from equation (3.4) with initial condition $(B(0), C(0), N(0)) = (0.033, 2.603, 0.498)$. The soil infiltration (d_1) and the SOM degradation rate (μ_s) are varied as indicators for soil quality status, and other parameters are fixed as in Table 3.2. (Top panels): Simulation reached the boundary steady state with $d_1 = 0.02$ top-left ($d_1 = 0.062$ top-right) and $\mu_s = 2.5$. (Bottom panels): Simulation reached a periodic solution and to an internal steady state with $d_1 = 0.02$ bottom left ($d_1 = 0.062$ bottom right) and $\mu_s = 2.8$. Note: The nitrogen transients are shown as $\theta^{-1}N(t)$ for comparison with $B(t)$ and $C(t)$ only in this case.	49
3.2	Three-dimensional transient dynamics. The parameters and initial condition (white triangle) are used as in Figure 3.1 (bottom-left panel). The nullsurfaces are represented in blue (B -nullsurface), red (C -nullsurface) and yellow (N -nullsurface). The time series is represented in blue dots, and the internal and boundary steady states are in stars (blue and green, respectively). The solution $(B(t), C(t), N(t))$ for $t > 0$ reaches close to E_0 at the beginning of the simulation, goes away from it and finalizes orbiting around E_1	50
3.3	Bifurcation diagram for model (3.4), fixing the parameters as in Table 3.2 and varying μ_s a soil health indicator. Three panels represent the bifurcation diagram for microbial communities (B), labile carbon in soil (C), and labile nitrogen in soil (N), and E_i for $i = 0, 1, 2$ denotes the stable (red) or unstable (black) system equilibria. A transcritical bifurcation occurs (TC) and corresponds to the boundary steady state E_0 at $\mu_s = 2.525$. The emergence of internal steady states occurs around $\mu_s = 2.381$ and a bistability region with it between E_0 and E_1 . Furthermore, a Hopf-Bifurcation (HB1 for the left branch and HB2 for the right branch) also emerges on the interval $\mu_s = [2.522, 3.02]$ and the maximum and minimum of the orbits are represented in blue.	51

3.4	Two-parameter bifurcation diagram for d_1 and μ_s as soil health indicators, where TC (S.B) stands for Transcritical (Stable Boundary). In Figure 3.4a, the stability of internal steady-state E_1 is represented in blue (stable) and red (unstable). The E_0 TC bifurcation divides the region into a stable (left) and unstable (right) steady state. The steady-state E_2 remains unstable, and a scatter plot in yellow approximately represents its region, avoiding a complete colour overlap. Figure 3.4b simplifies the region and rescales the magenta region in Figure 3.4a, representing only the contour of the stable steady-state E_1 and the TC bifurcation for reference to other numerical experiments. The dashed line $d_1 = 0.022$ indicates the fixed parameter during some of our simulations.	53
3.5	Two-parameter Bifurcation diagram for θ_p and μ_s , representing the N/C rhizodeposition ratio and a soil health indicator, respectively. The qualitative behaviour of steady states is similar and fully described in Figure 3.4a. However, the unstable steady state region for E_2 (a scatter plot in yellow represents the region and avoids colour overlap) is now contained in the bistability and the intersection of the unstable E_1 and microbial extinction region. The dashed line $\theta_p = 0.1$ indicates the fixed parameter for other simulations as reference. Note that high values used for θ_p ratios may be unrealistic regarding rhizodeposits but can be assumed if fertilizers input is also considered and is only used for numerical prediction purposes.	54
3.6	Plants rhizodeposits may increase overall N bioavailability by promoting microbial biomass and SOM mineralization depending on soil health indicators. The positive (negative) feedback denotes a cumulative increase of bioavailable N surplus from SOM mineralization (rhizodeposits) as the main source. The time interval to quantify such measurements is taken by the periodic limit cycles correspondent to the Hopf-bifurcation in Figure 3.3. The radius of each bubble denotes $ \lambda_{\mu_s} $, where λ_{μ_s} is defined in equation (3.32), representing the absolute cumulative rhizodeposition trade-off and its scale is given by the panel on the right. The cumulative microbial N -immobilization is represented in black and is given by integrating the N uptake rate by microbes over the specified period.	56
3.7	Comparison between N -rhizodeposition (red) versus N -mineralization (blue) subject to soil quality indicators d_1 and μ_s . The two-parameter bifurcation diagram from Figure 3.4b (grey) is on the background to show the cumulative N surplus given different stability regions. The threshold by which N -rhizodeposition equals N -mineralization over a period τ (see Figure 3.6) is plotted as a line with black circles in terms of the soil quality indicators. This threshold separates the region where the cumulative N -mineralization (right region) and N -rhizodeposition (left region) increases with respect μ_s . The panel on the right represents the N scales for each mechanism.	57

4.1	Experiment results for the short chain n-alkanes group. Red, black, blue and green colours distinguish experiment results between different temperature conditions. 5°C experiment is distinguished by the navy blue colour, black for 20°C, red for 30°C and green for the control experiment. The date of the DNA sample is shown in light blue. (a) Methane biogenesis derived from the biodegradation of short-chain n-alkane (pentane, C ₅ ; hexane, C ₆ ; heptane, C ₇ ; octane, C ₈ ; decane, C ₁₀). The cumulative theoretical maximum for both spikes is shown in dotted orange lines, and dotted stems (vertical lines) represent hydrocarbon spikes. Solid lines show the mean CH ₄ data trend. Panels (b) to (f) show the hydrocarbon degradation kinetics for each n-alkane compound. Simultaneous re-spikes for both temperature treatments are in orange.	67
4.2	Experiment results for the BTEX group. See Fig. 4.1 caption for more figure details. (a) Methane biogenesis derived Ethylbenzene, Toluene, mp-xylene and o-xylene biodegradation. The cumulative theoretical maximum for diverse spikes is in dashed black and red lines. Solid lines show the mean CH ₄ data trend and dotted stems represent hydrocarbon spikes. Panels (b) to (f) show the hydrocarbon degradation kinetics for each chemical compound labelled on the y-axis. Stems show an event such as spiking or DNA sample.	68
4.3	Experiment results for the iso-alkanes group. See Fig. 4.1 caption for more specific details. (a) Methane biogenesis derived from 2-MC ₅ , 3-MC ₆ , and 2M-C ₇ biodegradation for the first spike with additional 4-MC ₇ and 2-C ₉ for the second. The cumulative theoretical maximum for diverse spikes is orange (the first spike is in both treatments) and red. Solid lines show the mean CH ₄ data trend. Panels (b) to (f) show the hydrocarbon degradation kinetics for each chemical compound labelled on the y-axis. Stems show an event such as spiking or DNA sample.	70
4.4	Normalized Mean Square Error (NMSE) summary from subsample data set fitting. The distribution of the NMSE calculated contains degradation kinetics accuracy of n-pentane (C ₅), n-hexane (C ₆), n-octane (C ₈), n-decane (C ₁₀), toluene, ethylbenzene, xylene isomers, 2-MC ₅ , 3-MC ₆ , 2-MC ₇ , 4-MC ₇ , 2-MC ₈ , and 4-MC ₉ at different temperature (20°C and 30°C) and spikes. The NMSE quantifies the model accuracy from (∞, 1], where if NMSE= 1, then a perfect fit is achieved. The median NMSE value achieved is ≈ 0.9. The three different outliers belong to NMSE(C ₇ (T ₂₀ ¹))=0.52 NMSE(2-MC ₅ = 0.55 (T ₂₀ ¹)) and NMSE(2-MC ₅ = 0.69 (T ₃₀ ²))	77
4.5	Model (4.8) methane predictions against laboratory data (first column) and the sum of hydrocarbon data fitting results (second column) against hydrocarbon degradation experiments at 20°C (30°C) coloured in black (red). For simplified visual purposes, the sum of all hydrocarbon data points is shown and compared with model fitting. Panels (a) and (b) show the cumulative CH ₄ prediction compared to data and the cumulative n-pentane (C ₅), n-hexane (C ₆), n-heptane (C ₇), n-octane (C ₈) and n-decane (C ₁₀) degradation fitting. Panels (c) and (d) show the results obtained for toluene, ethylbenzene, and xylene isomers experiments. Panels (e) and (f) for iso-alkanes experiments, composed of 2-MC ₅ , and 2-MC ₇ for the first spike and an additional 4-MC ₇ and 2MC ₉ for the second spike for the 30°C experiment.	78

4.6	Model (4.8) predictions against laboratory data and CH ₄ data fitting. Panels (a) and (c): methane prediction against laboratory data and HC degradation sum model fitting at 20°C (3-MC6, 2-MC7, 4-MC7, 2-MC8) (data adapted from [80]). We added all hydrocarbon data points and model fittings for visual purposes. Panels (b) and (d): CH ₄ data fitting and sum HC degradation modelling (n-decane, n-octane, toluene, o-xylene, 3-MC6, 2-MC5) (data adapted from [48])	79
4.7	Degradation rate and lag phase estimation summary. The figure is divided into two columns, and each hydrocarbon group is arranged for each row, where the y-axis title in the first column determines the hydrocarbon group. Each column title indicates the estimated parameter. The x-axis for each panel represents the data subgroup (T_τ^s), where τ is the temperature (°C) and $s \in \{1, 2, 3\}$ is the number of spikes in each experiment hydrocarbon group. The first panel's row shows the n-alkanes degradation kinetics and lag phase at different temperatures subject to each experimental spike. The second panel's row is for TEX, and the third is for iso-alkanes. The degradation rate kinetics are expressed in a logarithm scale to improve its visualization, and box plots show the parameter dispersal, including outliers. The variation on T_20^1 experiments for iso-alkanes is derived by incorporating data from [80]	82
4.8	Conversion efficiency summary. Each panel title shows the calculated conversion efficiency for each HC group at different temperatures (τ) and spikes (s) T_τ^s . A boxplot for iso-alkanes conversion efficiency at 20°C was used to show the dispersed estimations and average related to two separated experiments for the first spike. The lowest value was attained in our experiment, and the highest was calculated from data adapted in [80].	83
4.9	Model parameter estimation summary. The parameter $0 \leq r_1 \leq 1$ determines CO ₂ flow from HC degradation, whereas $0 \leq r_4 \leq 1$ determines acetoclastic methanogen weight during CH ₄ production. The acetates degradation (CO ₂ reduction) rate is measured by r_2 (r_3). More accurate values for parameters r_2 and r_3 require measuring CO ₂ , acetates and/or hydrogen during HC degradation. Parameter dispersion for r_4 proportionally represents acetoclastic methanogens based on the DNA analysis.	83
4.10	Model (4.8) predictions on acetates, CO ₂ , and hydrogen kinetics by degrading a group of short-chain n-alkanes, TEX, and some iso-alkanes at different temperatures during methane biogenesis. Panels (a), (c), and (e) represent predictions for distinctive HC group experiments at 20°C, whereas panels (b), (d), and (f) belong to experiments at 30 °C. The numerical predictions are shown in a logarithm scale for better visualization. Acetates and CO ₂ scale are represented on the left axis, and hydrogen on the right for each panel.	85
4.11	FOM and phenomenological models output comparison. k_0^i represents the zero-order hydrocarbon degradation rate. The RMS predictions for the FOM, zero- and first-order model are described as RMS _{FOM} , RMS ₀ and RMS ₁ , respectively.	86

4.12	First-order mechanistic (FOM), zero- and first-order kinetic models comparison on the methane biogenesis estimation in MLSB for 2016-2017 and EPL simulation from 2018 to 2021. Methane biogenesis predictions are in blue, and HC kinetics are in brown. Dotted lines represent the zero-order kinetic model outputs, dashed lines for the first-order kinetic model and solid lines for the model (4.8). Diluent input from 2013-2015 is considered as the 60% of diluent loss reported during 2016 per assumed year, simulating a lower HC input over these years to reach a possible HC steady state. Methane was numerically unmeasured until 2016 to compare model cumulative CH ₄ predictions to the reported in MLSB during 2016-2017 [47]. Red dashed lines represent reported cumulative methane. The zero-order kinetic model underestimates CH ₄ reported by a factor of 2.1, 2.04 for the first-order kinetic model and 2.18 for the FOM model. After 2018, zero HC input was assumed to simulate an EPL scenario after OSTP closure. Methane emissions and HC degradation kinetics are predicted in four consecutive years of the simulation.	88
4.13	Yearly methane emissions comparison between FOM model predictions and Alberta Energy Regulator reports. Each panel represents methane emission comparison between different companies (a)-Syncrude, (b)-CNRL, (c)-Shell and (d)-Suncor reports against model predictions. Each bubble represents the ratio of methane FOM predictions and yearly reports for each company. The left axis represents the reported yearly diluent loss and localizes the center of each bubble. Green (red) bubbles represent an underestimation (overestimation) of methane predicted by the FOM model in percentage. The right axis represents the cumulative hydrocarbon kinetics over the years simulated by the FOM model. . . .	92

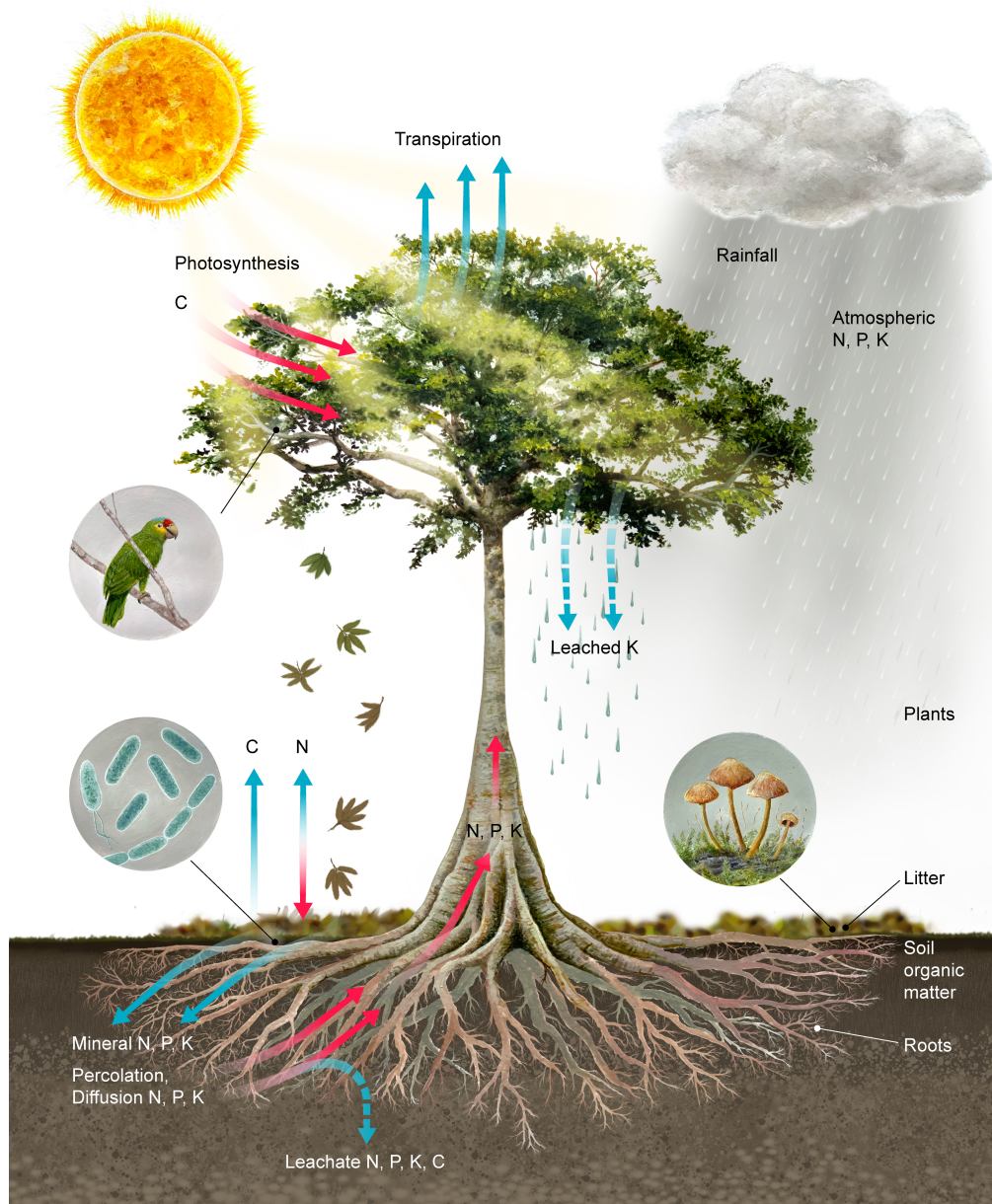


Figure adapted from: S. O.L., "Soil microbiology: a model of decomposition and nutrient cycling". CRC press, Inc., 1982.

Chapter 1

Introduction

1.1 Motivation

Interest in mitigating greenhouse gas (GHG) emissions from different anthropogenic sources is still rising due to their global warming potential [52], [89]. Of the different GHGs currently emitted from agricultural and industrial sectors, carbon dioxide (CO_2) and methane (CH_4) are at the top of ongoing research efforts to find strategies and solutions that help their mitigation and, in consequence, reducing their severe adverse effects on Earth [13].

Since 1896, Svante Arrhenius, a Swedish scientist, was the first to claim that fossil fuel combustion would eventually increase global temperatures, predicting that the mean surface would increase about four to five degrees Celsius if the current atmospheric carbon dioxide concentrations doubled [72]. Atmospheric CO_2 estimations using extracted cores from ancient glaciers showed that CO_2 atmospheric concentration was about 300 ppm approximately 300,000 years ago. Since the 1950s, an observatory on Mauna Loa, Hawaii, almost uninterruptedly have monitored carbon dioxide concentrations in the atmosphere, and current trends show a steady increase over the years, with a current concentration of around 400 ppm in 2020 [23] and currently 420 ppm in 2023.

On the other hand, methane is the second most abundant atmospheric GHG, accounting for 23% of the climate change since the Industrial Revolution. Its increasing trend rate has alerted global politics since methane is 25 times more severe in short-

time scales compared to CO₂ warming potential [33]. Compared to natural methane sinks, which include atmospheric oxidation and soil, anthropogenic methane sources, encompassing industrial fossil fuels extraction, agricultural sector and landfill management, biomass burning and rice cultivation, have generated a surplus in the total methane flux, leading to a concentration increase of this GHG in the atmosphere. Current estimations show that global methane sources exceed global sinks by 6 Tg per year [33], [89].

Mitigating these greenhouse gases requires different strategies and innovative tools that help with future predictions and provide critical factors that may consolidate possible pathways. For example, regarding CO₂, there is an open question to understand when soils are the source or sinks of this chemical compound in the short term [29]. Soils are a non-renewable source subject to exploitation due to ore contents, such as in the oil sands territories, wood harvesting, deforestation for land change of use, food production, etc., contributing to CO₂ increase, and appropriate land management is required to use soils as a sink through tropical forests conservation or sustainable agricultural food production [54]. However, anthropogenic derived CH₄ requires direct solutions such as tailing managements to decrease its production, despite its value as a natural gas source benefits. Some oil companies flare controlled CH₄ production rate surplus, converting it into carbon dioxide. However, in massive post-processing bitumen tailings, there is no primary mechanism to reduce its production, not considering other GHG produced, such as H₂S, NO_x, etc <https://www.aer.ca/>. Either way, CO₂ or CH₄ mitigation strategies can greatly benefit by understanding the core of these GHG sinks and sources, which are intrinsically related to organic matter biodegradation processes [27].

The primary thesis goals are to provide insights into soil biodegradation processes, contribute to developing innovative tools, and provide insights into potentially helpful initiatives related to global warming. This thesis achieves different milestones, including constructing two data-validated models, one to estimate CO₂ and another for CH₄ emissions. A critical milestone included a laboratory experiment in which I measured and modelled the temperature-dependence degradation rate of different diluents com-

monly used during the bitumen separation from oil sands. The experiment included temperature effects on methane biogenesis using fluid fine tailings samples from the Base Mine Lake (BML) in Alberta, Canada. My data served as a core for validating my model; I modelled and predicted hydrocarbon kinetics in the Mildred Lake Settle using governmental reports on hydrocarbon estimation loss and compared CH_4 emissions estimations using FFT temperature features, an unprecedented result to my best knowledge.

In the following subsections, I briefly introduce crucial concepts used during this thesis, including biodegradation processes, redox potentials, ecological stoichiometry, soil health indicators, oil sands tailing ponds (OSTP) and end pit lakes (EPL), the mathematical background of stability and bifurcations, and monotone dynamic systems. In the final part of this chapter, I provide an overview of the thesis structure.

1.2 Preliminaries

Biodegradation is a natural process by microbes that degrade organic material to grow, releasing essential nutrients to the soil and benefiting plants. Microbial degradation of organic compounds remains under study due to their capacity to degrade soil pollutants, and the by-products depend on the system features. For example, if oxygen is available for microbes, then they will likely produce more CO_2 , and when oxygen is exhausted, and only CO_2 is available, they produce CH_4 . In the following subsections, I provide some useful definitions and tools used during this thesis.

1.2.1 Redox potential

According to [33], [89], microbes require different chemical species as terminal electron acceptors (TEA) as part of their metabolic process, and different reduction-oxidation (redox) potentials determine the relative thermodynamic preference during the production or consumption of trace gasses in soil. For example, microbes that use oxygen as a TEA yield more energy than those that are anaerobically adapted and use nitrate, oxidized iron, sulfate or CO_2 . Aerobic processes are more likely to occur in well-aerated soils because diffused oxygen is present through porous media zones. After oxygen

consumption, different microbes seek TEA alternatives based on thermodynamic favorability. When oxygen becomes limited, denitrification processes take place, releasing nitrogen gases. At the bottom of the microbial thermodynamical preference, CH_4 is produced using CO_2 after the exhaustion of more favourable TEA. For example, in oil sands territories, unrecovered diluents (carbon sources) are dumped into ponds after oil sands bitumen separation. Over the years, CH_4 production in these ponds proves that microbes use CO_2 as TEA and apparently have exhausted other potential chemical species they could use.

1.2.2 Canadian oil sands territories

Canada's Oil sands are the world's third-largest oil reserve, representing 166.3 billion barrels (<https://natural-resources.canada.ca/>). Bitumen extraction from oil sands relies on two methods depending on how deep the oil deposits are buried. In-situ production refers to deep bitumen recovery located 75 meters underground, in which human-created horizontal wells serve to inject steam and pump the liquified bitumen from the oil sands to the surface continuously. Open-pit mining operates similarly to mineral mining operations, in which oil sands reserves are closer to the surface or less than 75 meters underground. Large-scale machinery digs the surface, and the mined material is transported into crushers to process large clumps of earth. The crushed material, mainly formed by sand, clay, and bitumen, is mixed with hot water and light hydrocarbons as diluents to separate the bitumen before being upgraded into synthetic crude oil. Like any other mining operations, leftover material, or tailings, are stored in basins, called tailing ponds, allowing solid materials to settle and recover water used during the process. Different ponds, including the Mildred Lake Settle Basin and Base Mine Lake, started to become methane biogenesis active in early 1990, and subsequently, research proved that some of the diluent components, including short-chain n-alkanes and some BTEX compounds, support methane production [77]. Now, methane production can be beneficial in increasing water recovery from tailings [24]. However, depending on basins and tailings features, it is required to precisely estimate methane production periods and concentrations to fulfill methane-reducing strategies

implemented by the federal government of Canada in 2021.

[27], [35], [37], [75].

1.2.3 Mathematical approach

In this thesis, I used essential mathematical theories, including stability and bifurcation theories, to study soil biodegradation processes under aerobic and anaerobic conditions. Solving dynamical systems coupled to systems that consider different mechanisms between variables may represent a challenge. However, the system can be described qualitatively by studying equilibria and their stability, providing insights into the solution behaviour and possible prediction outcomes. Local stability criteria describe the nature of an equilibrium point, determining whether system solutions may be attracted, at least in a local neighbourhood. If all the solutions end in a steady state regarding different initial conditions, then this equilibrium is referred to as a globally stable steady state [62]. Studying local solutions behaviour in such equilibria requires system linearization and determining the nature of the characteristic polynomial the linear system provides [70].

Models coupled to natural phenomena usually depend on the parameters given, which may change over time or physical features such as temperature dependence. A bifurcation defines a change in the system's qualitative behaviour caused by a parameter variation. These variations encompass the creation or destruction of equilibria or alterations in their stability [70]. Studying bifurcation in soil biodegradation processes can provide insights into essential parameters representing specific processes, such as nutrient bioavailability. Bifurcation diagrams provide a full spectrum of how parameter variation affects a system qualitatively, which can be related to the linearized system. In Chapter 3, I use these mathematical tools to explore the symbiotic relationship between plants and microbes through rhizodeposits.

1.3 Temperature-dependent methane biogenesis in fluid fine tailings experiments

Methane emissions from oil sands tailing ponds in Alberta, Canada, are a topic of high research interest since provincial and federal governments are committed to capping methane emissions through new policies near 2030 (<https://www.alberta.ca/climate-oilsands-emissions>). Current methane monitoring methodologies are still under development, and creating accurate tools for in-situ methane predictions is a priority. It is known that fluid fine tailings (FFT), a by-product material formed by a mix of silt, clays, bitumen and diluents used to separate the ore from oil sands, supports methane biogenesis [27], [37], [75]. Still, different features present in in-situ scenarios have yet to be considered, including the temperature effects on methanogens.

In Chapter 4, we developed a new mechanistic model that is data-validated through a series of laboratory results measuring the hydrocarbon degradation kinetics under different temperatures. Our approach aims to create a model that considers how temperature plays a role during methane emissions and to construct a solid basis for reducing the in-situ methane emissions gap by incorporating new modelling features.

1.4 Thesis overview

The main chapters of this thesis encompass GHG estimation tools through a mathematical and experimental approach. Chapter 2 has been published, Chapter 3 is under review, and Chapter 4 will be submitted for publication soon. The synthesis of each chapter is described as follows:

Chapter 2 proposes and data-validate a stoichiometric mathematical model on the priming effect, i.e., increased soil organic matter turnover when adding labile substrates. This model was proven robust using a local sensitivity analysis, and different outcomes are presented depending on the soil organic matter nutrient-to-carbon ratio. This model is proposed as the basis for understanding soil biodegradation processes when nutrient limitations are present in aerobic conditions.

Chapter 3 extends the model in Chapter 2 and is adapted to the concept of soil

quality to explore the dynamic interactions between microbes and plants through rhizosphere depositions. This model considers soil health qualities related to implicit soil conditions such as carbon-to-nutrient ratio content and soil infiltration. The results show plants' engagement with microbes increases or decreases rhizodeposits depending on the soil nutrient availability.

Chapter 4 includes the laboratory experiment to determine different diluent degradation kinetics under different temperature setups. We analyzed the microbial composition through DNA analysis and determined the time required for bacteria to start degrading hydrocarbons, degradation rates, methane biogenesis and conversion efficiency. In this chapter, we construct a mechanistic model that incorporates two pathways for methane production, extending our capacity to model CH_4 and CO_2 , a link missing in the current models. Using the model and data sets, we validate our model and show prediction potentials against governmental data reported in the Mildred Lake Settle Basin incorporating fluid fine tailings features such as temperature gradients over the year.

Chapter 5 concludes this thesis by discussing the results' significance and future directions.

Chapter 2

A Data-validated stoichiometric model for the priming effect

2.1 Introduction

The potential effects of increased atmospheric carbon dioxide (CO_2) on global warming have been a matter of public interest since the industrial revolution [23], [53], [89]. Carbon sequestration in plant biomass and soil organic matter through appropriate management of cultivated soils is a process that can mitigate the atmospheric CO_2 . By understanding the dynamical exchange of carbon and nitrogen from the atmosphere into the terrestrial ecosystems, carbon sequestration may be improved [4], [5], [51], [93]. In particular, part of the soil scientists' efforts has been towards studying CO_2 emissions from soils due to their potential contribution to global warming. Different theories are being continuously developed to describe the linked interactions between organic matter and labile compounds as soil microbial activities [6], [14], [49], [51].

Soil Organic Matter (SOM) is a significant carbon reservoir and is a principal nutrient source for plant growth as it contributes to soil quality [29]. SOM is a complex biological residue formed over time due to the accumulation of undecayed, recalcitrant organic matter [14], [53], [89]. SOM carbon pool is about two or three times that in the atmosphere. Thus any changes will significantly affect the atmospheric carbon concentration levels [55], [89]. The input of fertilizers, organic substances and plant residues may increase the microbial activity in soils, enhancing the decomposition rate of SOM in short periods. Consequently, a sudden and increased release of CO_2 from

soil respiration would directly contribute to global warming[6], [14], [53].

The priming effect is defined as the sudden increase rate of SOM by the input of substrates in soils [51]. This natural phenomenon and its mechanisms have been an important topic in several European countries over the last decades [49]. Despite many theories and mechanisms proposed to describe the priming effect, in this work, we consider the ‘stoichiometric decomposition’ and ‘microbial nitrogen mining’ approach [14]. These mechanisms relate the SOM decomposition rate depending on the availability of labile carbon (C) and nitrogen (N) for different microbial communities. The ‘stoichiometric decomposition’ mechanism assumes that microbial SOM decomposition rate is at its highest when their demand of C and N is satisfied and decreases when the availability of N is limited [36]. On the other hand, the ‘microbial nitrogen mining’ mechanism assumes increased harvesting for N from SOM using labile C as an additional energy source to satisfy microbial growth requirements [17], [59].

Different microbial communities decompose SOM at different rates regarding the availability of substrates. The linkage between the mechanisms mentioned above is due to the dynamical interaction between these microbial communities, labile carbon and nitrogen sources, and SOM [14]. Soil microbial communities may be separated into two main groups despite the vast number of microbes capable of degrading SOM. Rapidly growing soil bacteria mainly involved in decomposing labile substrates are termed *zymogenous* bacteria. Now, slow-growing organisms predominantly associated with the decomposition of SOM are classed as *autochthonous* [93]. In this sense, the stoichiometric decomposition and microbial nitrogen mining mechanisms can be related to *zymogenous* and *autochthonous* bacteria respectively [14], [17], [36].

It is necessary to incorporate C and N dynamics into mathematical models to study the priming effect as the interaction between microbial communities, labile compounds, and SOM [8]. To achieve this, we develop a stoichiometrical mathematical model that simultaneously considers stoichiometric decomposition and microbial nitrogen mining mechanisms. The stoichiometrical framework for our system of ordinary differential equations allows us to incorporate C and N dynamics from labile substrates as the carbon and nutrient dynamics contained in the SOM. We validate our model using

a laboratory data set adapted from [14]. Part of the complete laboratory data set shows how different soil treatments based on labile C and N may induce different CO_2 emission rates from soils depending on the strength of the priming effect. Including different pools to track carbon and nutrient contents in SOM as labile substrates rely on the assumption that the priming effect is governed by the availability of resources, microbial biomass, and stoichiometric constraints [14], [21], [83].

Our approach considers the balance of soil substrates as their interaction with microbial communities during the SOM decomposition process, i.e., using stoichiometry theory [83]. We determine the robustness of the model and the crucial parameters for the priming effect with a sensitivity analysis. In this way, we investigate how soil features, such as nutrient content in SOM, delimit an optimized C:N of labile substrates to decompose SOM in terms of efficiency, the priming effect strength and the time of maximum SOM decomposition rate. Furthermore, we explore the impact of the SOM degradation efficiency on the system and how the acceleration or decrease of the priming effect is related. The model could provide insights into how using substances rich in C and N , such as green manure, for example, in different levels of nutrient richness in soils, may indirectly impact global warming by modifying the SOM degradation rates in short periods.

2.2 Model formulation

To study the decomposition of SOM under aerobic conditions, we propose the following stoichiometrical mathematical model. The ‘stoichiometric decomposition’ and ‘microbial N mining’ mechanisms are continuously subject to a system of non-linear differential equations and governed by the availability of labile compounds such as C and N . Such mechanisms are triggered implicitly by the microbial biomass growth rate and constrained by the availability of substrates. It is assumed that SOM decomposition rate increases with only adding labile C as the ‘microbial N mining’ mechanism suggest. Moreover, it is at its highest when the microbial biomass demand of labile C and N is satisfied as ‘stoichiometric decomposition’ mechanisms convey [14], [29]. In natural soil ecosystems, N is the limiting nutrient for microbial communities. To keep

the model as simple as possible, we consider only C , N found in organic substances as a necessary simplification [14], [53]. Finally, the CO_2 emissions from the decomposition of organic matter are described in terms of the microbial respiration rate [51].

The microbial biomass rate of change depends on the availability of easily degradable substrates as the ability to harvest the required nutrients from SOM [14]. Both microbial communities such as *zymogenous* and *autochthonous* decompose SOM at different efficiency levels, and their growth rates differ regarding the availability of labile resources [7], [14]. To mathematically consider this limitation, we consider Liebig's law of the minimum, which states that the microbial growth rate is limited by the most limiting resource [83]. To track the microbial biomass rate of change in terms of carbon units, we make use of the following equation:

$$B' = \underbrace{(\mu_c \min\{f(N), g(C)\} + \mu_s H(C) \min\{f_s(N_s), g_s(C_s)\})}_{\text{intrinsic growth}} B - \underbrace{\epsilon B}_{\text{death}} - \underbrace{lB}_{\text{respiration}}, \quad (2.1)$$

where $H(C)$ is a dimensionless saturating function that modulates the impact of a mechanism during the decomposition of SOM regarding the availability of labile C in soils. The first two terms on the right-hand side of the above equation correspond to the intrinsic microbial growth. In particular, the first term corresponds to the fast-growing *zymogeneous* bacteria, and the second term to the slow-growing *autochthonus* bacteria. The minimum function is related to Liebig's law which limits the maximal microbial growth rate in terms of the available resources in the system. The dimensionless functions $f(N)$ and $g(C)$ (or simply f , and g) corresponds to saturating functions which represents the N and C uptake rate respectively [97]. For simplicity, the SOM pool is divided into the amount of recalcitrant carbon C_s and nitrogen N_s , respectively. The dimensionless functions $f_s(N_s)$ and $g_s(C_s)$ (or simply f_s and g_s) are saturating functions which represents the SOM compounds degradation rates. The last two terms correspond to biomass loss by microbial death (ϵ) and respiration (l) rates.

The dynamics for the labile carbon pool are given by

$$C' = - \underbrace{\frac{\mu_c}{r_1} \min\{f(N), g(C)\} B}_{\text{labile carbon decomposition}} + \underbrace{\epsilon B}_{\text{carbon recycling}}. \quad (2.2)$$

In the above equation, the yield constant (r_1) is the proportional conversion of C to microbial biomass [46]. It is also considered the immediate carbon recycling in this model by the natural death of microorganisms at a rate (ϵ).

A simplified version of a more complex process for the nitrogen dynamics is represented as follows:

$$N' = - \underbrace{\theta \mu_c \min\{f(N), g(C)\}B}_{\text{labile nutrient uptake}} + \underbrace{\theta(\epsilon + l)B}_{\text{nutrient recycling}} + \underbrace{(\theta_s - \theta) \mu_s H(C) \min\{f_s(N_s), g_s(C_s)\}B}_{\text{nutrient exudation from SOM decomposition}}, \text{ where } \theta_s > \theta. \quad (2.3)$$

The first term corresponds to the microbial labile nutrient uptake rate to satisfy stoichiometric growth requirements. The second term represents nutrient recycling due to mass-specific microbial respiration loss and death rate [2], [46]. The constant parameter (θ) correspond to the microbial nitrogen:carbon ratio, and it is assumed constant since we are assuming a strict homeostasis [83], [98], [99]. The last term represents the nutrient exudation from SOM decomposition where (θ_s) is the nutrient:carbon ratio for SOM, which is assumed constant for simplicity [28], [85].

The dynamics for recalcitrant carbon in SOM are represented as

$$C'_s = - \underbrace{\frac{\mu_s}{r_2} H(C) \min\{f_s(N_s), g_s(C_s)\}B}_{\text{recalcitrant carbon decomposition}}, \quad (2.4)$$

where the yield constant r_2 is the proportional conversion of C_s to microbial biomass.

Finally, the dynamics of the recalcitrant nutrients found in SOM are described as

$$N'_s = \underbrace{-\theta_s \mu_s H(C) \min\{f_s(N_s), g_s(C_s)\}B}_{\text{nutrient uptake from SOM decomposition}}, \quad (2.5)$$

where is assumed that $\theta_s > \theta$. In this way, microbial harvest for SOM nutrients will increase the labile nutrients availability in soils. This assumption is supported by the findings on plants allocating rich labile C substrates to microbial communities through their roots in exchange nutrients found in SOM [89]. Therefore, we propose the whole

model as

$$\begin{aligned}
B' &= (\mu_c \min\{f(N), g(C)\} + \mu_s H(C) \min\{f_s(N_s), g_s(C_s)\}) B - \epsilon B - lB, \\
C' &= -\frac{\mu_c}{r_1} \min\{f(N), g(C)\} B + \epsilon B, \\
N' &= -\theta \mu_c \min\{f(N), g(C)\} B + \theta(\epsilon + l) B + (\theta_s - \theta) \mu_s H(C) \min\{f_s(N_s), g_s(C_s)\} B, \\
C'_s &= -\frac{\mu_s}{r_2} H(C) \min\{f_s(N_s), g_s(C_s)\} B, \\
N'_s &= -\theta_s \mu_s H(C) \min\{f_s(N_s), g_s(C_s)\} B,
\end{aligned} \tag{2.6}$$

where the saturating functions take the Monod form; i.e.

$$f(N) = \frac{N}{N + K_f}, \quad g(C) = \frac{C}{C + K_g}, \quad f_s(N_s) = \frac{N_s}{N_s + K_{f_s}}, \quad g_s(C_s) = \frac{C_s}{C_s + K_{g_s}}, \tag{2.7}$$

and $H(C)$ we will propose it as

$$H(C) = 1 - \frac{C}{C + K_h}. \tag{2.8}$$

The function $H(C)$ modulates the ‘microbial N mining’ and ‘stoichiometric decomposition’ mechanism depending on the availability of labile substrates. The microbial growth will increase at high rates when the microbial stoichiometric constraints are met, potentially increasing SOM decomposition. On the other hand, with sustained utilization of labile C , the nutrient exudation from SOM decomposition is continuously increasing and is proportional to the microbial biomass. Now, emissions of CO_2 in this model are directly related to the microbial respiration rate. To model the CO_2 rate of change we will use the following equation:

$$\text{CO}_2' = lB'. \tag{2.9}$$

Since we consider the model for short periods and the laboratory data used was based on a closed nutrient system, i.e. there is no loss or gain of N , we assume the conservation of law matter for N . Then, the total nitrogen (T_N) dynamics present in model (2.6) is given by

$$T'_N = \theta B' + N' + N'_s = 0, \tag{2.10}$$

for some $\theta_s > \theta$. Therefore, the total nitrogen in the system is fixed and

$$N = T_N - \theta B - N_s, \quad (2.11)$$

where

$$T_N = \theta B(0) + N(0) + N_s(0), \quad (2.12)$$

which evidently results in a simplification of system (2.6) if required.

2.3 Material and methods

The increased atmospheric CO₂ derived from the heavy use of crop fields has led soil scientists to study the priming effect over the last decades. Several mechanisms and theories have been developed to explain this natural phenomenon. However, the combination of stoichiometric decomposition as the microbial nitrogen mining mechanisms has been supported by laboratory experiments [14], [51]. The laboratory experiment used to validate this model is summarized as follows.

2.3.1 Laboratory experiment

The combination of the stoichiometric decomposition and microbial nitrogen mining mechanisms was experimentally supported to understand better the priming effect [14]. This experiment measured different microbial growth rates, extracellular enzyme production, and CO₂ emissions derived from the decomposition of labile substrates as from SOM. The experiment was based on adding different soil treatments to soil samples previously homogenized and stored in separated jars. Part of the soil treatments was based on adding only labile *C* or *N* or a combination of both. The CO₂ emissions from SOM decomposition were directly measured, and different priming effect intensities were identified depending on the soil treatment by the ninth day.

For this work, we consider the control sample and three soil treatments: added mineral *N* (min-N), sucrose (suc-C), and min-N with suc-C. A detailed description for each treatment used in four different jars is given in Table 2.1. The data adapted from [14] for these treatments is provided in Figure 2.1.

Treatment	Amount ($\mu\text{g C g soil}^{-1}$)	Applied N ($\mu\text{g N g soil}^{-1}$)
Control	0	0
min-N	0	110
Suc-C	500	0
Suc-C+min-N	500	110

Table 2.1: Experimental design. Table adapted from [14].

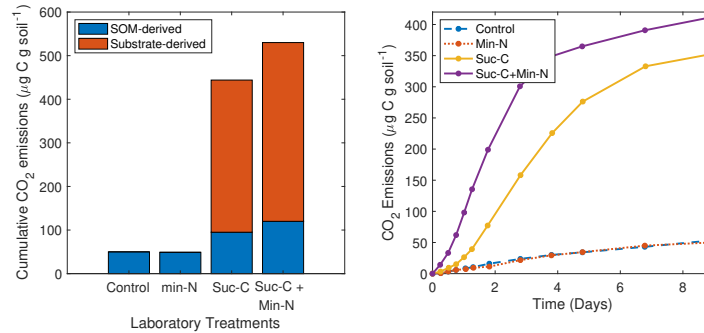


Figure 2.1: Data adapted from [14]. (Left panel): Cumulative CO₂ emissions from four different soil treatments in the ninth day. (Right panel): Cumulative CO₂ emissions over nine days for each experiment.

Mathematically speaking, different experimental treatments will correspond to different initial conditions $C(0)$, and $N(0)$ for our model. The data points represented in Figure 2.1 was used to validate the model (2.6) with equation (2.9).

2.3.2 Data fitting

The CO₂ data emissions from the laboratory experiment found in [14] were adapted using OriginPro 2020 software. The cumulative SOM degradation measured in terms of CO₂ was differentiated in the laboratory from labile C degradation using radioactive isotopes. Since our model tracks the cumulative CO₂ directly from microbial respiration, a discrepancy arises between the laboratory data set and the model predictions. This discrepancy leads to the unavailability of parameters for the system (2.1). However, some parameters are found in the literature, and the rest were fit.

We split the data into four groups corresponding to each treatment as in Table 2.1. Then, we simultaneously fit the equations (2.6) and (2.9) for each group with different

Param.	Definition	Value/Range	Unit	Ref.	95% C.I.
μ_c	Max. growth rate for labile C	8.31	day ⁻¹	Fitted	[7.35 - 9.27]
μ_s	Max. growth rate for C_s	6.62	day ⁻¹	Fitted	[6.21 - 7.04]
l	Respiration rate	3.05	day ⁻¹	Fitted	[2.94 - 3.12]
ϵ	Microbial death rate	0/[0.1056]	day ⁻¹	[62]	-
r_1	Yield constant	0.104/[0 - 1]	-	Fitted	[0.09 - 0.117]
r_2	Yield constant	0.103/[0 - 1]	-	Fitted	[0.067 - 0.14]
θ	Microorganisms N:C ratio	0.2	-	[83]	-
θ_s	SOM decomposition N:C ratio	0.3946	-	Fitted	[0.371 - 0.417]
K_f	N -dependent H.S.C. for microorganisms growth	2.9	$\mu\text{g N g soil}^{-1}$	[62]	-
K_g	C -dependent H.S.C. for microorganisms growth	30	$\mu\text{g C g soil}^{-1}$	[57], [62]	-
K_{fs}	N_s -dependent H.S.C. for microorganisms growth	1277.42	$\mu\text{g N g soil}^{-1}$	Fitted	1277.42
K_{gs}	C_s -dependent H.S.C. for microorganisms growth	19.1164×10^3	$\mu\text{g C g soil}^{-1}$	Fitted	[19145.7 - 19177.7]
K_h	C -dependent H.S.C. for microorganisms strategy	474.78	$\mu\text{g C g soil}^{-1}$	Fitted	[325.22 - 624.33]

Table 2.2: List of parameters used for the numerical simulation. H.S.C stands for half-saturation constant. C.I. stands for Confidence Interval.

Initial condition	Values	Unit	Reference	95% C.I.
$B(0)$	3.63	$\mu\text{g C g soil}^{-1}$	Fitted	[2.89 - 4.37]
$C(0)$	{0, 500}	$\mu\text{g C g soil}^{-1}$	[14]	-
$N(0)$	{0, 110}	$\mu\text{g N g soil}^{-1}$	[14]	-
$C_s(0)$	1.47×10^4	$\mu\text{g C g soil}^{-1}$	[14]	-
$N_s(0)$	980	$\mu\text{g N g soil}^{-1}$	[14]	-

Table 2.3: Initial conditions.

initial conditions corresponding to each treatment. We predict the four data groups with fixed parameters and different initial conditions. Full description of the used parameters, as its references, can be found in Tables 3.2, and 2.3. For this particular case, we consider the death rate $\epsilon = 0$ given the short period of the experiment.

To avoid over-fitting, the ratio #(data points):#(free parameters) is 4.8. The free parameters are estimated using a nonlinear regression function in MATLAB (*nlinfit*). We determine the goodness of fitness from predictions given by equation (2.9) by using

the Normalized Mean Square Error (NMSE) function defined in MATLAB as

$$\text{NMSE} = 1 - \frac{\|x_0 - x_1\|^2}{\|x_0 - \bar{x}_0\|^2}, \quad (2.13)$$

where $\|\cdot\|$ is the euclidean norm, x_0 is a vector that contains data points, x_1 is the predictions from the model and \bar{x}_0 is the mean of the experimental data points. The function NMSE defined in MATLAB measures the goodness of fitness predicted in the interval $(-\infty, 1]$ where the perfect fit is if the function is equal to one. The minimum value we achieved using the NMSE function was about 0.9, and the numerical simulation is shown in Figure 2.2. We estimate the 95% confidence intervals using the MATLAB function (*nlparci*) and the coefficient estimates, residuals and the estimated covariance matrix from *nlinfit*.

The data fitting reveals that SOM decomposition dynamics are governed primarily by C_s transients for this particular data set. The degradation efficiency for the nutrients uptake in SOM (K_{f_s}) determines if C_s or N_s dynamics govern SOM decomposition. If $K_{f_s} < K_{g_s} N_s(t)/C_s(t)$, for some t , then SOM dynamics are governed by C_s , otherwise it will be governed by N_s . By choosing $K_{f_s} \approx K_{g_s} N_s(0)/C_s(0)$, we discard the possibility that SOM decomposition is governed by C_s limitation only.

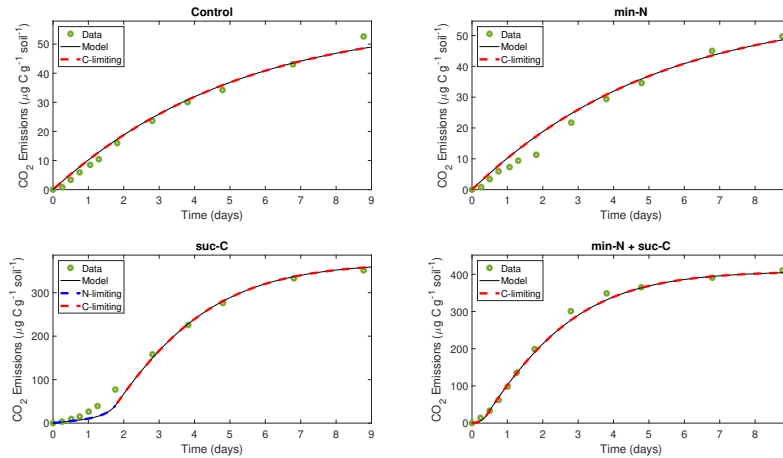


Figure 2.2: Model validation using the data adapted from [14] and parameters from Tables 2.1, 3.2, and 2.3. Each panel represents a different soil treatment. It is shown when labile C or N limits the CO_2 emissions. The system is mostly C -limited because it is not considered an external sink of labile nutrients such as plants.

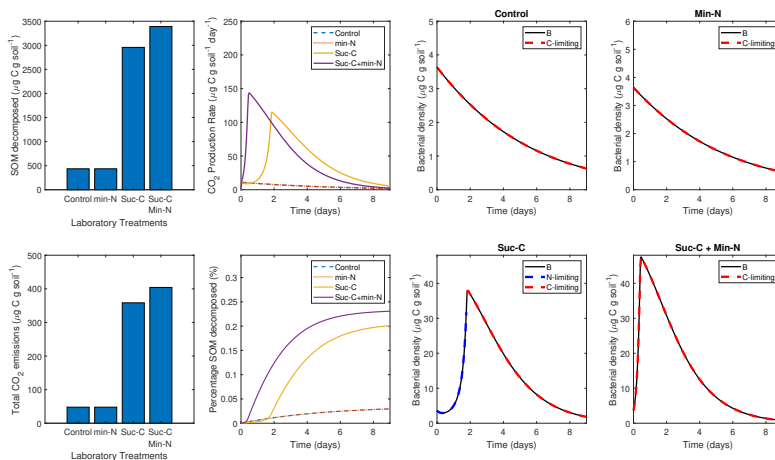


Figure 2.3: Numerical simulations of the model (2.6) and (2.9) using Tables 3.2, 2.3, and 2.1. (First column): Cumulative SOM decomposed and CO_2 emissions. (Second column): CO_2 production and percentage of SOM decomposed with respect to time. (Third and fourth column): Simulated microorganisms biomass subject to different SOM decomposition mechanisms.

2.4 Numerical simulations

We validate our model by comparing the predictions of CO_2 from the model to the adapted laboratory data set. However, the model predictions of the degradation of SOM differ somewhat from reality. The first panel in Figure 2.3 shows the cumulative decomposed SOM on the ninth day of each experiment. The numerical simulation for SOM decomposition is at least consistent with the experiment in [14], i.e., a combination of added labile substrates promotes a higher decomposition rate of SOM rather than using only N and C separately.

Our simulations show that the system is C -limited predominantly for all treatments, except when labile C is added. This is because we are not assuming other external sinks of labile nutrients, such as plants' N uptake for biomass formation. Adding only labile N will not increase the SOM decomposition, and microbial N mining mechanism strength remains weak since there is no labile C to utilize. Adding labile C increases microbial N mining mechanism strength; consequently, more nutrients from SOM are released, increasing microbial biomass production. Adding labile C and N will increase the SOM decomposition at higher rates by rapidly increasing mi-

crobial biomass and activities subject to the stoichiometric decomposition mechanism (see Figure 2.3).

Measuring the robustness of the model will provide insightful performance on the model's predictions on SOM decomposition as information on the sensitivity of the parameters used. The reliability of SOM dynamics predictions with respect to the availability of labile substrates can be measured, and we may track down those crucial parameters during the priming effect with a sensitivity analysis.

2.4.1 Sensitivity analysis

We perform a local sensitivity analysis to understand how significantly the parameters used in the model affect SOM decomposition. Each parameter sensitivity index can measure the relative importance of the parameters influencing SOM degradation. The definition of the normalized forward sensitivity index is

$$\gamma_p^u := \frac{\partial u}{\partial p} \times \frac{p}{u}, \quad (2.14)$$

where u is the variable that depends differentiably on the parameter p . A forward difference scheme is needed to compute the sensitivity index because of the absence of an explicit solution of system (2.6). The numerical sensitivity index is

$$\gamma_p^u = \frac{u(p + \Delta p) - u(p)}{\Delta p} \times \frac{p}{u(p)}, \quad (2.15)$$

where $u(p)$ refers to the variable of interest dependent on the parameter p , and Δp should be a small quantity such as 1% of the default value of p . The sensitivity index γ_p^u is a real number by which we can measure the relative importance of a parameter, and the sign of this value is the positive (or negative) relationship concerning the variable u .

We denote Γ_i^j as $C_s(9)$ with the parameters given in Table 3.2 and the initial conditions given in Table 2.3 but with $N(0) = i$ and $C(0) = j$. We consider the variable

$$u = 1 - \frac{\Gamma_i^j}{C_s(0)}, \quad (2.16)$$

to compute the sensitivity index for the percentage of SOM decomposed on the ninth day for $i = \{0, 110\}$ and $j = \{0, 500\}$ to represent the different experimental treatments. Thus, we can measure the importance of each parameter in our model for SOM

decomposition predictions. The parameter's positive (negative) relationship strength depends on each soil treatment. The sensitivity analysis reveals the model's robustness and the positive (negative) strength of SOM decomposition on the ninth day of the experiment. From Figure 2.4, it may be surprising that the parameter μ_s , associated with slow-growing bacteria but predominant in SOM degradation, is more beneficial to SOM conservation. Based on the data-fitting, the system is primarily C_s -limited, but SOM decomposition under N_s -limitation was also investigated. We computed the sensitivity index for these two circumstances, guaranteeing the model's robustness for different scenarios.

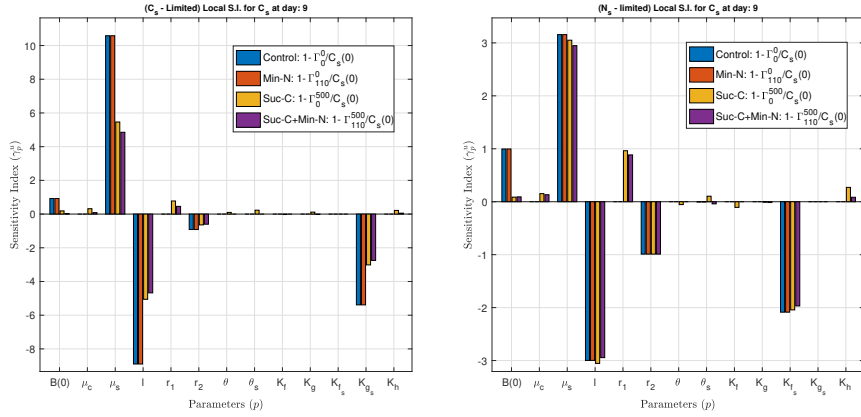


Figure 2.4: Sensitivity Index (S.I.) for $u = 1 - \Gamma_i^j / C_s(0)$ for $i = \{0, 100\}$ and $j = \{0, 500\}$ of SOM decomposition when different treatments are considered. (Left panel): S.I. using parameters in Table 3.2. In this case, the system is C_s -Limited ($K_{f_s} < K_{g_s} N_s(0) / C_s(0)$). (Right panel): S.I. when the system is N_s -Limited, i.e., we choose K_{f_s} such that $K_{f_s} > K_{g_s} N_s(0) / C_s(0)$.

2.4.2 Numerical experiment: impact of Exogenous Labile C and N in SOM decomposition

The addition of a combination of labile substrates controls the strength of the priming effect and, in consequence, increases atmospheric emissions of CO_2 from soils in short periods. The addition of only labile C increases SOM decomposition during the laboratory experiment, and the decomposition is higher when exogenous labile C and N are combined. We explore numerically how the combination of a single input of

$C(0) \in [0, 500]$ and $N(0) \in [0, 30]$ at $t = 0$ influences SOM decomposition.

From Figure 2.5 (left panel), we show the relative SOM decomposition increment when the combination of $C(0) = j$ and $N(0) = i$ is considered and compared to when only $C(0) = 500$ is added as $1 - \Gamma_i^j/\Gamma_0^{500}$ for $i \in [0, 30]$ and $j \in [0, 500]$. Furthermore, we show an optimal C:N ratio, represented by the red line in the same figure, initially required to decompose SOM efficiently, minimizing the resources of labile substrates. We also plot different curves generated by $1 - \Gamma_i^j/\Gamma_0^{500}$ on the right panel of the same figure when $i \in [0, 30]$ and $j = \{0, 100, 200, \dots, 500\}$. The red dots in each curve generate an optimal C:N ≈ 26 ratio to decompose SOM efficiently, and they are represented by maximum (i, j) such that $|\Gamma_i^j - \Gamma_{30}^j| < \varepsilon \Gamma_0^{500}$ for $\varepsilon = 0.1$. We choose the specified interval for $N(0) \in [0, 30]$ because adding larger labile N inputs does not change the results qualitatively, suggesting that low input of labile N may have the same potential to greatly impact SOM decomposition as high inputs of labile N.

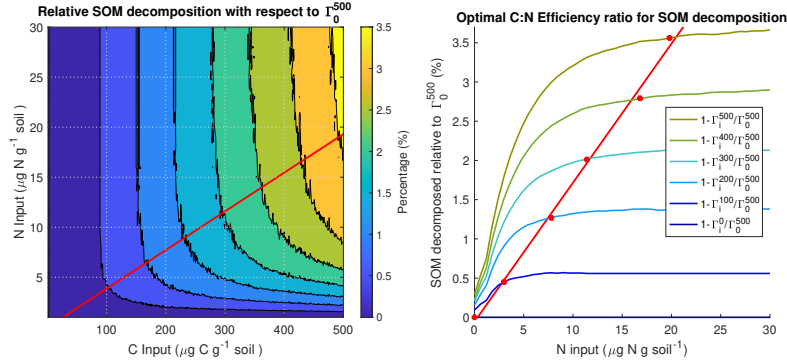


Figure 2.5: Impact of adding an initial single dose of labile N and C to soils during SOM decomposition. (Left panel): Relative SOM decomposition increment when the combination of $C(0) = j$ and $N(0) = i$ is considered and compared to when only $C(0) = 500$ is added as $1 - \Gamma_i^j/\Gamma_0^{500}$. (Right panel): Different curves generated by $1 - \Gamma_i^j/\Gamma_0^{500}$ when $i \in [0, 30]$ and $j = \{0, 100, 200, \dots, 500\}$. The red line in both panels is given by $N(C) = C/25.83$ and represents an optimal C:N initial ratio to maximize SOM decomposition in terms of efficiency and is generated by a linear regression using the points (i, j) such that $|\Gamma_i^j - \Gamma_{30}^j| < \varepsilon \Gamma_0^{500}$ for $\varepsilon = 0.1$.

We extend our results regarding the optimal C:N ratio inputs to maximize SOM by considering different SOM carbon-to-nutrient ratios ($C_s:N_s$). By fixing the total amount of carbon in SOM ($C_s(0)$), we estimate the labile C:N ratios required as initial

amendments to decompose SOM efficiently in terms of the initial nutrient richness in it ($N_s(0)$). In Figure 2.6, we can see that high (low) amounts of labile N will maximize SOM decomposition for nutrient-rich (nutrient-poor) soils. These results show that the C:N ratio to maximize SOM decomposition will depend on the dynamics that govern SOM decomposition, that is, when SOM is C_s or N_s limited. If SOM dynamics are strictly governed by C_s transients, then the optimal C:N ratio remains constant, but if N_s transients govern it, then the optimal C:N ratio will increase linearly with respect to the initial carbon-nutrient content in SOM.

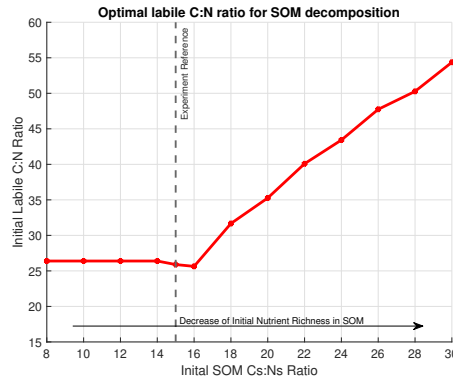


Figure 2.6: Optimal initial C:N ratio to decompose SOM efficiently with respect to the SOM nutrient-richness ratio. The experimental reference is $C_s(0) : N_s(0) = 15$, and the labile C:N ratio for labile substrates in the laboratory experiment was approximately 4.5. The optimal labile C:N ratio is constant for nutrient-rich soils, and it increases linearly for nutrient-poor soils.

The expected time required for microbial communities to decompose SOM at its highest rate (t_M) will depend on the initial amendments and initial $C_s:N_s$ ratio. We compared the predicted time t_M for two different amendments. Specifically we consider only $C(0) = 500$, $N(0) = 0$ and when $C(0) = 500$, $N(0) = 20$ as an optimized treatment. Also, we computed the percentage of SOM carbon decomposed relatively to $C_s(0) : N_s(0)$ ratios by the ninth day using the same amendments (see Figure 2.7). By adding labile C and N , the t_M is constant because the stoichiometric decomposition mechanism is immediately at its highest, independent of SOM nutrient content. In contrast, adding only labile C will increase the t_M for nutrient-poor soils and remains constant for nutrient-rich soils. The microbial N mining mechanisms will predominate

for larger periods in nutrient-poor soils until enough nutrients are released from SOM decomposition. The percentage of decomposed carbon in SOM at ninth day is constant for nutrient-rich soils and will decrease for nutrient-poor soils. These results show that the soil’s nutrient richness determines the time and strength of the priming effect.

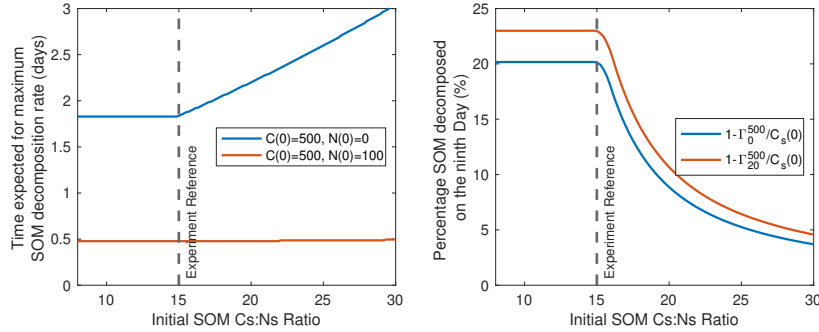


Figure 2.7: (Left panel): Time expected for the priming effect to occur, i.e., when microbial communities decompose SOM at its maximum rate. (Right panel): Percentage of decomposed SOM by different treatments by the ninth day.

2.4.3 Numerical experiment: positive and negative priming effect

The results from the laboratory experiments in [14] showed a positive priming effect when Suc-C and Suc-C+min-N were added to soil samples. However, there was not a significant statistical difference after adding min-N. Positive or negative priming effects, i.e., increase or reduction of SOM decomposition after adding labile substrates respectively, have been documented when N is added into soil samples [51]. For example, in [38] it is stated that nitrogen depositions reduce SOM decomposition in temperate forests.

In our model, the SOM degradation efficiency K_{g_s} and K_{f_s} are highly related relatively to the cumulative SOM decomposition (see Figure 2.4). SOM priming depends on the input of labile sources C and N , and microbial activities. However, microbial activities also rely on their ability to uptake resources from SOM. To understand how the SOM degradation efficiencies regulate the priming effect strength for two different soil treatments, we propose the following numerical experiment by considering K_{g_s} and

K_{f_s} as parameters.

We define $S_C = C_s(0) - \Gamma_0^{500}$ as our numerical experiment reference, and we compute the difference with $S_{CN}(K) = C_s(0) - \Gamma_{20}^{500}$ but varying only $K = K_{f_s}$ ($K = K_{g_s}$) which is the half-saturation constant for f_s (g_s). In Figure 2.8, the positive (negative) value indicates a negative (positive) priming effect concerning the different values of the half-saturation constants. We suggest that the half-saturation for recalcitrant carbon and nitrogen saturating functions in SOM should not be considered a constant but a function of other physical properties. In this way, the system will potentially show negative priming effects even if the soils are treated with a combination of labile compounds.

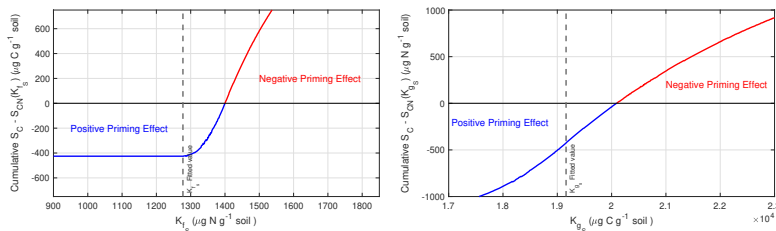


Figure 2.8: Difference of cumulative decomposed SOM between soil treated with $C(0) = 500$, $N(0) = 0$ (Γ_0^{500}), and with $C(0) = 500$, $N(0) = 20$ (Γ_{20}^{500}) varying K_{f_s} (left panel) and K_{g_s} (right panel) on the ninth day. The parameters are taken as in Table 3.2. The initial conditions for other variables are considered as in Table 2.3. The model is capable to reproduce positive (negative) priming effects depending on the value for the half-saturation constant for f_s and g_s .

2.5 Discussion

The CO_2 emissions derived from soils have been a subject of interest in the last years due to the potential effects of global warming. In particular, sudden increments of SOM decomposition rates in short periods derived from using labile substrates such as fertilizers have gained attention, and different mechanisms have been proposed to explain these increments over the last decades [51], [53]. Recently, a laboratory experiment has supported combining the ‘microbial N mining’ and ‘stoichiometric decomposition’ mechanism to explain this natural phenomenon named the priming effect

[14]. Various mathematical models successfully model the priming effect by tracking without considering both mechanisms and only tracking carbon pools. Incorporating these mechanisms, as nitrogen dynamics, is needed to increase the accordance between mathematical models and data measurements [8], [14]. Therefore, we proposed for the first time the inclusion of both mechanisms to explain the priming effect as carbon and nitrogen dynamics in a novel stoichiometric mathematical model.

The mathematical model in this work encompasses microbial utilization of different labile and recalcitrant carbon and nitrogen pools to predict the strength of the priming effect in soils with diverse SOM carbon and nutrient contents. Based on the laboratory data adapted to validate the model, we were required to estimate those parameters that were not available in the literature with 95% confidence. Our results predicted that the carbon dynamics in SOM principally governed the laboratory experiment results. Under this assumption and considering that the model is nutrient closed, simplifying the model by tracking only carbon dynamics in SOM would be possible. However, SOM degradation may be subject to nutrient content, and we considered that possibility in our model predictions.

We validated our results and showed model prediction robustness through a local sensitivity analysis. The laboratory experiment used abundant soil treatments in labile carbon and nitrogen to produce the priming effect. However, we predicted an optimized labile C:N ratio of approximately 26 would have the same results compared to C:N ratio of 4.54 used for the experiment. This prediction assumes that soil amendments based on only labile carbon are enough to produce the priming effect and increase by adding labile nitrogen. Furthermore, we found that the optimized ratio of labile substrates to decompose SOM efficiently remained constant for nutrient-rich soils and increased for nutrient-poor soils. This result is comparable with the prediction in [29], which predicted that nutrient-poor soils are more often subject to the priming effect than nutrient-rich soils. Our results showed that less labile nitrogen input is needed to maximize SOM decomposition in nutrient-poor soils. Studying how nutrient richness in soils affects the model predictions, we found that in nutrient-rich soils, the priming effect is likely to happen in short periods. Still, depending on the soil treatment, it

may be delayed and weakened in nutrient-poor soils. Finally, given the sensitivity analysis, we determined that the SOM degradation efficiency determines the increase or reduction of the priming effect on this model, which can be correlated with other physical properties like temperature [22], for example.

This model still has limitations. First, the assumption for the function that modulates SOM decomposition mechanisms is heuristic, and predictions could improve by using mechanistic fundamentals. Second, the CO₂ emissions, when only carbon is used as a soil treatment, still present inaccuracies at the beginning of the simulation. The heuristic function that modulates both mechanisms may still be improved to produce better results without compromising its use to modulate the mechanisms behind the priming effect. The model also suggests that the SOM degradation efficiencies should be considered parameters, not constants, for general situations. Otherwise, the model may not accurately represent the negative priming effect. Another limitation is that the model is robust for short periods and is based on the assumption that it is nutrient closed. However, these issues will open more research directions, for example, considering the nutrient uptake by plants, SOM decomposition for larger periods and continuous or periodic inputs of labile substrates.

Chapter 3

Rhizosphere dynamics under simplified soil health indicators

3.1 Introduction

Excessive use of fertilizers in terrestrial systems directly impacts the soil, water and air quality through nitrate leaching, eutrophication of lakes and potentially increasing cyanobacteria blooms, and emitting greenhouse gases such as N_2O emissions [60], [100]. Reducing its use and ensuring increased crop yields are major global challenges in which understanding the beneficial interactions between plants and the rhizosphere microbiome is required [68], [87]. These interactions are derived through plant rhizodeposits when the scarcity of nutrients in soil limits plants' development, and it encompasses a dynamic relationship between terrestrial carbon and nitrogen cycles, which can result in plant health promotion and fitness [16], [58]. However, current laboratory methodologies to study the rhizosphere and microbial interactions with soils involve destructive sampling, difficulting its understanding [33]. Thus, developing new tools, including mechanistic mathematical models, are necessary to provide more or possibly new insights into terrestrial processes.

In terrestrial processes, mineral nutrients usually limit plant growth in terrestrial ecosystems, and specific microbial communities can increase their bioavailability in soils by mineralizing soil organic matter (SOM) [63], [68]. Under nutrient limitation conditions, plants can supply microbes with rich labile substrates in the rhizosphere, promoting their growth and activities [26], [40]. In exchange, microbes are expected

to increase the nutrient bioavailability by mineralizing SOM, especially nitrogen (N), the principal limiting nutrient in soils [9], [84]. The root exudates, or rhizodeposits, are part of plants' mechanisms that may promote their development [60]. However, it may also increase the competition between plants and soil microorganisms for nutrient availability [50]. Microbes immobilize labile substrates in soils to satisfy their stoichiometric constraints for growth, decreasing nutrients required for plant growth [56], [83]. Still, under certain soil conditions, they might also promote nutrient bioavailability by degrading SOM at an increased rate [49], [68].

Rhizodeposits are a mixture of labile substrates that include carbon, nitrogen, phosphorous, etc., which plants exude through their roots depending on different environmental features and soil health indicators [50], [60]. Soil health is defined by the National Resources Conservation Services features (NRCS) as "The capacity of the soil to function as a vital living ecosystem that supports plants, animals and humans." It is a broader term containing soil quality, which is used to establish soil N availability, soil structural stability, SOM carbon-to-nitrogen contents and microbial activities, to mention a few, as soil health indicators [84]. The importance of connecting soil health indicators to plant rhizodeposition relies on a better understanding of the symbiotic relationship between plants and microbes, providing knowledge and guidance on how fertilizers impact soils [9], [15], [32].

Plants can contribute to microbial growth, and uncertainties arise regarding increasing or immobilizing nutrient bioavailability under different soil features, which are still to be explored [60], [68]. Diverse soil microorganisms exist in the rhizosphere, including principal slow-growth SOM decomposers microorganisms (oligotrophs) and fast-growth and labile substrate decomposers microorganisms (copiotrophs) [65]. Oligotrophs are more suitable to survive in low soil nutrient bioavailability due to their capability to decompose SOM in such harsh conditions. On the contrary, copiotroph bacteria are rapid-growth microorganisms highly dependent on labile substrate availability but inefficient SOM decomposers [33]. These microbial communities are essential for plant survival in temperate forests, for example, in which plants release root exudates to promote their growth and retrieve essential nutrients derived from microbial SOM de-

composition [14], [16], [60]. However, plant growth may be affected if the microbial stoichiometry growth demands are satisfied and the soil health has deteriorated [43], [56], [83].

Experimentally tracking rhizodeposition’s indirect influence on SOM mineralization is challenging due to destructive laboratory methods to obtain data samples from soil-root-microbes systems or because of instrument limitations to measure microbial biomass and its dynamics [33]. Now, soil health indicators, a broader term that includes soil quality, characterizes the environmental functioning between plants and microbes, and its features depend on soil physicochemical properties, including carbon and nitrogen storage, soil infiltration and nutrients cycle [31], [84]. More than two hundred SOM models have been published since 1930, and the CENTURY model and its different versions are the most cited since 1980 [12]. These models vary in different timescales or hypotheses and may include macronutrient pools like carbon, nitrogen, and phosphorous dynamics and soil features like temperature, infiltration, etc. However, their approach is mostly based on statistical or empirical dynamics that may include several first-order equations to be handled [10], [39], [45], [64], [66], [67], [90]. Including mechanistic processes could benefit these models when specific soil fractions and dynamics based on dynamical microbial activities under stoichiometric restrictions are available [14], [83], [96]. Furthermore, given their importance in the agricultural sector, these models focus principally on carbon pools, and incorporating rhizodeposits’ interactions with microbial communities under soil health indicators will provide valuable missing insights [8], [34], [56].

This work proposes a stoichiometric mathematical model to understand rhizosphere interactions between the plants and soil microbes’ symbiotic relationship in a simplified terrestrial system. To substantially contribute to current SOM model efforts, the mechanisms in this model are related to labile nitrogen bioavailability as a limiting nutrient and simplified soil health indicators. The mechanistic model in this work considers soil infiltration rate, related to soil structural stability, SOM carbon-to-nitrogen content as the major pool of recalcitrant nutrients, and general microbial activities which degrade SOM to release and increase nutrients bioavailability. The model core is

based on a previous data-validated mathematical model [96]. However, in this model, we simplify SOM dynamics to incorporate soil health indicators, reducing the model complexity and allowing a mathematical analysis that establishes a new background to determine how soil features directly affect plants' use of rhizodeposition for their health promotion and fitness through numerical experiments.

3.2 Mathematical model

We propose the following mathematical model to study rhizodeposition impacts on soils, considering some crucial soil health indicators in a soil-plant-microbial system, such as microbial activities, soil infiltration and SOM C/N content [84]. However, we assume a continuously replenishing undecayed organic material to keep the model simple, which may be reasonable for short or even long periods in different scenarios, including in some actively agricultural soil [44]. In this context, our model assumes the SOM carbon-to-nutrient ratio remains unchanged, allowing us to measure the rhizodeposition effects on microorganisms' SOM mineralization directly.

The microbial biomass rate of change depends on the bioavailability of labile compounds and their capacity to mineralize recalcitrant nutrients found in SOM [7], [14]. This limitation is given stoichiometrically using Liebig's law and the ability of microbes to use part of the labile C to mineralize SOM, satisfying their growth requirements [83]. Then,

$$B' = \underbrace{(\mu_c \min\{f(N), g(C)\} + \mu^\Gamma \Gamma(C_s, N_s) H(C)) B}_{\text{intrinsic simplified growth}} - \underbrace{\epsilon B}_{\text{death}} - \underbrace{lB}_{\text{respiration}}, \quad (3.1)$$

where $C_s \geq 0$ and $N_s \geq 0$ are SOM carbon and nitrogen pools. We consider $0 \leq \Gamma(C_s, N_s) \leq 1$ as a constant since we assume unchanged SOM content in soil for this model. The first two terms on the right-hand side correspond to the intrinsic growth rate of copiotrophs and oligotrophs microorganisms, respectively [33], [96]. The parameter μ_c is the maximum growth rate when labile C are N are abundant, allowing fast-growth bacteria to proliferate. The maximum growth rate of slow-growth

bacteria, capable of decomposing SOM more efficiently, is given by μ^F [96]. However, since we assume unchanged SOM content for simplification, we will rewrite part of the second term as $\mu_s = \mu^F \Gamma(C_s, N_s)$, allowing us to study soil-plant-microbes dynamics by a free parameter that represents part of soil health indicators, determining the microbial SOM degradation rate implicitly [61]. Since we are differentiating slow- and fast-growing bacteria, the bacterial maximum growth rate is assumed to satisfy $\mu_s < \mu_c$ [14], [49]. The last two terms represent microbial communities' natural death and respiration rate. It is considered that the microbial respiration rate is greater than the microbial death rate ($l > \epsilon$), and the maximum growth rate for rapid-growth bacteria is higher than the respiration rate and death rate ($\mu_c > l + \epsilon$). Otherwise, microbial communities' survival would be compromised independently of the amount of available sources.

The dynamics of the labile carbon pool will consider both organic carbon available for microorganisms from external sources, such as manure, and plant's derived labile carbon from rhizodeposition. In this way,

$$C' = - \underbrace{\frac{\mu_c}{r} \min\{f(N), g(C)\} B}_{\text{labile carbon decomposition}} + \underbrace{\epsilon B}_{\text{carbon recycling}} + \underbrace{P^{in}(N)}_{\text{C-rhizodeposition}} - \underbrace{d_1 C}_{\text{carbon loss}}, \quad (3.2)$$

where $0 < r < 1$ determines the yield conversion of C to the microbial biomass and $\epsilon > 0$ represents the immediate labile carbon recycling to the system by natural microorganisms death rate [97]. In the third term, we include the labile carbon input from the plant's roots to the soil or carbon rhizodeposit. Note that plants use rhizodeposits as a trade-off to promote microbial growth, thus increasing the SOM mineralization and the release of available nutrients (N) for their benefit [9], [68]. The rhizodeposits amount depends on different soil and atmospheric features, such as light intensity, temperature, pH, moisture, etc. [33]. For simplicity, we consider only the available labile N as the plant driver to input rhizodeposits and promote microbial activities [43], [71]. The last term represents the labile C loss rate determined by soil infiltration as a soil health indicator [56], [84].

The nitrogen soil cycle complexity is simplified as labile N , easily uptaken by microbial communities and plants. In this model, nitrogen dynamics are given by

$$\begin{aligned}
N' = & - \underbrace{\theta \mu_c \min\{f(N), g(C)\} B}_{\text{nutrient immobilization}} + \underbrace{\theta(\epsilon + l) B}_{\text{nutrient recycling}} + \\
& \underbrace{(\theta_s - \theta) \mu_s^\Gamma \Gamma(C_s, N_s) H(C) \min\{f_s(N_s), g_s(C_s)\} B}_{\text{nutrient exudation from SOM mineralization}} + \\
& \underbrace{\theta_p P^{in}(N)}_{N\text{-rhizodeposition}} - \underbrace{(P^{out}(N) + d_1 N)}_{N\text{-plant uptake and -infiltration}}, \text{ where } \theta_s > \theta.
\end{aligned} \tag{3.3}$$

The first term tracks the nutrient uptake from microbial communities to satisfy their stoichiometric requirements to growth, and θ represents the nitrogen-to-carbon conversion ratio and is assumed constant since strict homeostasis for microbes is assumed [83], [98], [99]. This term refers to nutrient immobilization since microbes use and hold labile N to produce biomass, making it unavailable for plants [33]. The second term assumes the nutrient recycling to be immediately available due to mass-specific death and respiration rates [2], [46]. The third term tracks the microbial nutrient exudation due to SOM mineralization, which is enhanced by the available labile C and directly relates to the priming effect if it is considered, especially possible when C_s and N_s pools are tracked [96]. We also consider θ_s as a constant parameter to keep the model simple [28], [85]. The last terms correspond to plant rhizodeposition, given by the nitrogen-to-carbon ratio parameter θ_p , labile N plant uptake and nutrients leaching to underground water [16], [60], [68]. For this model, it is assumed that the rhizodeposit function satisfies that $0 \leq P^{in}(N)$, and $P^{in}(N)' < 0$.

Therefore, our model to study the rhizodeposition effects to microbial communities with simplified SOM mineralization dynamics is proposed as

$$\begin{aligned}
B' &= (\mu_c \min\{f(N), g(C)\} + \mu_s H(C)) B - (\epsilon + l) B, \\
C' &= -\frac{\mu_c}{r} \min\{f(N), g(C)\} B + \epsilon B + P^{in}(N) - d_1 C, \\
N' &= -\theta \mu_c \min\{f(N), g(C)\} B + \theta(\epsilon + l) B + (\theta_s - \theta) \mu_s H(C) B + \\
& \quad \theta_p P^{in}(N) - (P^{out}(N) + d_1 N),
\end{aligned} \tag{3.4}$$

where the functions $f(N)$, $g(C)$ and $P^{out}(N)$ follows the Monod form,

$$f(N) = \frac{N}{K_f + N}, \quad g(C) = \frac{C}{K_g + C}, \quad P^{out}(N) = \alpha^{out} \frac{N}{\beta_N + N}, \tag{3.5}$$

and α^{out} is the plant maximum nutrient uptake rate and K_f , K_g and β_N are half saturation constants (H.S.C) for their respective functions [82], [97]. The function $H(C)$, which modulates the microbial SOM mineralization mechanism [96], takes the form as

$$H(C) = 1 - \frac{C}{K_h + C}. \quad (3.6)$$

Finally, plant rhizodeposits exponentially decay with respect to the root length, and it may be diffused over the soil matrix, which plants have no control over. However, the net input of labile compounds close to the rhizosphere is higher in order of magnitude than its diffusion [26], [40]. Therefore, the plant rhizodeposition, which depends on nutrient N availability in soils, we propose it as

$$P^{in}(N) = \alpha^{in} e^{-\beta_c N}, \quad (3.7)$$

to remain consistent with the literature, where $\alpha^{in} > 0$ is the maximum labile C input rate and β_c is a unidimensional parameter that modulates the rhizodeposit rate.

3.3 Model analysis

Our model simplifies the soil-plant-microbial carbon and nitrogen dynamics, and in this section, we rigorously investigate its mathematical behaviour. Feasible biological interpretations can be achieved by first demonstrating the model's well-posedness through its positivity and soundness. Also, the model's long-term behaviour is assessed by exploring all potential steady states and their local stability. Furthermore, we establish criteria for the extinction and persistence of rhizosphere microbiomes, allowing us to study our model prediction outcomes.

For our mathematical analysis, we define

$$\begin{aligned} L_1 &= 2(\mu_s + \epsilon r - \epsilon - l) + d_1, \\ L_2 &= 2\theta_s(\epsilon + l) - d_1(\theta_s - \theta). \end{aligned}$$

3.3.1 Positivity and boundedness

Consider the following region Ω as

$$\Omega = \{(B, C, N) : B > 0, C > 0, N > 0\}$$

Theorem 1. *Solutions of (3.4) with initial conditions in the Ω remain there for all forward time. Furthermore,*

if $L_1 \leq 0$, then $\Omega \cap \{(B, C, N) : \frac{1}{r}B(t) + C(t) < \frac{2\alpha^{in}}{d_1}\}$ is invariant for system (3.4);

if $L_2 \leq 0$, then $\Omega \cap \{(B, C, N) : (\theta - \theta_s)B(t) + N(t) < \theta_p \frac{2\alpha^{in}}{d_1}\}$ is invariant for system (3.4);

if $\frac{1}{r}L_1 + L_2 \leq 0$, then $\Omega \cap \{(B, C, N) : (\frac{1}{r} - (\theta_s - \theta))B(t) + C(t) + N(t) < \frac{2\alpha^{in}(1+\theta_p)}{d_1}\}$ is bounded and invariant for system (3.4).

Proof. Assume $S(t) = (B(t), C(t), N(t))$ is a solution of system (3.4) with $S(0) \in \Omega$ and $t_1 > 0$ is the first time that $S(t)$ touches or crosses the boundary of Ω . We will prove the theorem by contradiction arguments from six cases.

Case 1. $B(t_1) = 0$.

$$\begin{aligned} \frac{dB}{dt} &= (\mu_c \min \{f(N), g(C)\} + \mu_s H(C)) B - (\epsilon + l)B \\ &\geq -(\epsilon + l)B \\ &\equiv \delta_1 B, \quad \forall t \in [0, t_1], \end{aligned}$$

where δ_1 is a constant. Thus, $B(t_1) \geq B(0)e^{\delta_1 t_1} > 0$ holds, which contradicts with $B(t_1) = 0$. Therefore, $S(t_1)$ can not reach this boundary.

Case 2. $C(t_1) = 0$. Let $\hat{B} = \max_{t \in [0, t_1]} B(t)$.

$$\begin{aligned} \frac{dC}{dt} &= -\frac{\mu_c}{r} \min \{f(N), g(C)\} B + \epsilon B + P^{in}(N) - d_1 C \\ &\geq -\frac{\mu_c}{r} g(C) B - d_1 C \\ &= -\frac{\mu_c}{r} \frac{C}{K_g + C} B - d_1 C \\ &\geq -\left(\frac{\mu_c}{r} \frac{\hat{B}}{K_g} + d_1 \right) C \\ &\equiv \delta_2 C, \quad \forall t \in [0, t_1], \end{aligned}$$

where δ_2 is a constant. Thus, $C(t_1) \geq C(0)e^{\delta_2 t_1} > 0$ holds, which contradicts with $C(t_1) = 0$. Therefore, $S(t_1)$ can not reach this boundary.

Case 3. $N(t_1) = 0$.

$$\begin{aligned} \frac{dN}{dt} &\geq -\theta\mu_c \min\{f(N), g(C)\} B - (P^{out}(N) + d_1 N) \\ &\geq -\theta\mu_c f(N) B - \left(\frac{\alpha^{out}}{\beta_N + N} + d_1 \right) N \\ &\geq - \left(\frac{\theta\mu_c \hat{B}}{K_f} + \frac{\alpha^{out}}{\beta_N} + d_1 \right) N \\ &\equiv \delta_3 N, \quad \forall t \in [0, t_1], \end{aligned}$$

where δ_3 is a constant. Thus, $N(t_1) \geq N(0)e^{\delta_3 t_1} > 0$ holds, which contradicts with $N(t_1) = 0$. Therefore, $S(t_1)$ can not reach this boundary.

Case 4. $\frac{1}{r}B(t_1) + C(t_1) = \frac{2\alpha^{in}}{d_1}$.

Let

$$y_1(t) = \frac{1}{r}B(t) + C(t). \quad (3.8)$$

Since $L_1 = 2(\mu_s + \epsilon r - \epsilon - l) + d_1 \leq 0$, then $\forall t \in [0, t_1]$,

$$\begin{aligned} \frac{d}{dt}y_1(t) &\leq \left(\frac{\mu_s}{r} + \epsilon - \frac{\epsilon + l}{r} \right) B + \alpha^{in} - d_1 C \\ &\leq -\frac{d_1}{2}y_1(t) + \alpha^{in}. \end{aligned}$$

Hence,

$$y_1(t) \leq \frac{2\alpha^{in}}{d_1} + \left(y_1(0) - \frac{2\alpha^{in}}{d_1} \right) e^{-\frac{d_1}{2}t} < \frac{2\alpha^{in}}{d_1}. \quad (3.9)$$

Therefore, $S(t_1)$ can not go across this boundary.

Case 5. $(\theta - \theta_s)B(t_1) + N(t_1) = \frac{2\alpha^{in}\theta_p}{d_1}$.

Let

$$y_2(t) = (\theta - \theta_s)B(t) + N(t).$$

Since $L_2 = 2\theta_s(\epsilon + l) - d_1(\theta_s - \theta) \leq 0$, then $\forall t \in [0, t_1]$,

$$\begin{aligned} \frac{d}{dt}y_2(t) &\leq \theta_s(\epsilon + l)B - d_1 N + \alpha^{in}\theta_p \\ &\leq -\frac{d_1}{2}y_2(t) + \alpha^{in}\theta_p. \end{aligned}$$

Hence,

$$y_2(t) \leq \frac{2\alpha^{\text{in}}\theta_p}{d_1} + \left(y_2(0) - \frac{2\alpha^{\text{in}}\theta_p}{d_1} \right) e^{-\frac{d_1}{2}t} < \frac{2\alpha^{\text{in}}\theta_p}{d_1}.$$

Therefore, $S(t_1)$ can not cross this boundary.

$$\text{Case 6. } \left(\frac{1}{r} - (\theta_s - \theta) \right) B(t_1) + C(t_1) + N(t_1) = \frac{2\alpha^{\text{in}}(1+\theta_p)}{d_1}.$$

Let

$$y_3(t) = \left(\frac{1}{r} - (\theta_s - \theta) \right) B(t) + C(t) + N(t). \quad (3.10)$$

Then,

$$\frac{d}{dt}y_3(t) \leq \left(\frac{1}{r}\mu_s + \epsilon - (\epsilon + l) \left(\frac{1}{r} - \theta_s \right) \right) B + \alpha^{\text{in}}(1 + \theta_p) - d_1(C + N).$$

Since $\frac{1}{r}L_1 + L_2 \leq 0$,

$$\frac{1}{r}\mu_s + \epsilon - (\epsilon + l) \left(\frac{1}{r} - \theta_s \right) \leq -\frac{d_1}{2} \left(\frac{1}{r} - (\theta_s - \theta) \right).$$

It follows that,

$$\begin{aligned} \frac{d}{dt}y_3(t) &\leq -\frac{d_1}{2} \left(\frac{1}{r} - (\theta_s - \theta) \right) B - \frac{d_1}{2}(C + N) + \alpha^{\text{in}}(1 + \theta_p) \\ &= -\frac{d_1}{2}y_3(t) + \alpha^{\text{in}}(1 + \theta_p). \end{aligned}$$

Then, $\forall t \in [0, t_1]$,

$$y_3(t) \leq \frac{2\alpha^{\text{in}}(1 + \theta_p)}{d_1} + \left[y_3(0) - \frac{2\alpha^{\text{in}}(1 + \theta_p)}{d_1} \right] e^{-\frac{d_1}{2}t} < \frac{2\alpha^{\text{in}}(1 + \theta_p)}{d_1}. \quad (3.11)$$

Therefore, $S(t_1)$ can not cross this boundary, completing the proof. \square

We proved the positivity of the system (3.4) by showing the set Ω is invariant in Theorem 1. This guarantees that our system is biologically meaningful. Moreover, with additional conditions, the system is invariant in even smaller sets. We now prove the dissipativity of the system, i.e. these sets can not only be invariant but also attract all solutions.

Theorem 2. *Suppose the initial value $(B(0), C(0), N(0)) \in \Omega$.*

(a) *If $L_1 \leq 0$, then $\limsup_{t \rightarrow \infty} B(t) \leq \frac{2r\alpha^{\text{in}}}{d_1}$, and $\limsup_{t \rightarrow \infty} C(t) \leq \frac{2\alpha^{\text{in}}}{d_1}$.*

(b) *If $\frac{1}{r}L_1 + L_2 \leq 0$ and $\frac{1}{r} - (\theta_s - \theta) > 0$, then the system (3.4) is dissipative. Moreover,*

$$\limsup_{t \rightarrow \infty} B(t) \leq \frac{2r\alpha^{\text{in}}(1+\theta_p)}{d_1(1-r(\theta_s-\theta))}, \quad \limsup_{t \rightarrow \infty} C(t) \leq \frac{2\alpha^{\text{in}}(1+\theta_p)}{d_1}, \quad \text{and} \quad \limsup_{t \rightarrow \infty} N(t) \leq \frac{2\alpha^{\text{in}}(1+\theta_p)}{d_1}.$$

Proof. By (3.8) and (3.9) if $L_1 \leq 0$, we have

$$\begin{aligned} y_1(t) &= \frac{B(t)}{r} + C(t) \\ &\leq \frac{2\alpha^{\text{in}}}{d_1} + \left(y_1(0) - \frac{2\alpha^{\text{in}}}{d_1} \right) e^{-\frac{d_1}{2}t} \\ &\equiv \frac{2\alpha^{\text{in}}}{d_1} + C_1 e^{-\frac{d_1}{2}t}, \end{aligned}$$

where C_1 is a constant. Hence,

$$\limsup_{t \rightarrow \infty} \frac{B(t)}{r} + C(t) \leq \frac{2\alpha^{\text{in}}}{d_1}.$$

Moreover, by Theorem 1, $\forall t \geq 0$, $B(t) > 0$, $C(t) > 0$, then

$$\begin{aligned} \limsup_{t \rightarrow \infty} B(t) &\leq \frac{2r\alpha^{\text{in}}}{d_1}, \\ \limsup_{t \rightarrow \infty} C(t) &\leq \frac{2\alpha^{\text{in}}}{d_1}. \end{aligned}$$

By (3.10) and (3.11), if $\frac{1}{r}L_1 + L_2 \leq 0$, we have

$$\begin{aligned} y_3(t) &= \left(\frac{1}{r} - (\theta_s - \theta) \right) B(t) + C(t) + N(t) \\ &\leq \frac{2\alpha^{\text{in}}(1 + \theta_p)}{d_1} + \left[y_3(0) - \frac{2\alpha^{\text{in}}(1 + \theta_p)}{d_1} \right] e^{-\frac{d_1}{2}t} \\ &\equiv \frac{2\alpha^{\text{in}}(1 + \theta_p)}{d_1} + C_2 e^{-\frac{d_1}{2}t}, \end{aligned}$$

where C_2 is a constant. Hence,

$$\limsup_{t \rightarrow \infty} \left(\frac{1}{r} - (\theta_s - \theta) \right) B(t) + C(t) + N(t) \leq \frac{2\alpha^{\text{in}}(1 + \theta_p)}{d_1}.$$

Similarly, since $\forall t \geq 0$, $B(t) > 0$, $C(t) > 0$, $N(t) > 0$, and $\frac{1}{r} - (\theta_s - \theta) > 0$, then

$$\begin{aligned} \limsup_{t \rightarrow \infty} B(t) &\leq \frac{2r\alpha^{\text{in}}(1 + \theta_p)}{d_1(1 - r(\theta_s - \theta))}, \\ \limsup_{t \rightarrow \infty} C(t) &\leq \frac{2\alpha^{\text{in}}(1 + \theta_p)}{d_1}, \\ \limsup_{t \rightarrow \infty} N(t) &\leq \frac{2\alpha^{\text{in}}(1 + \theta_p)}{d_1}. \end{aligned}$$

This completes the proof. □

3.3.2 Equilibria

After determining the invariant set of our model (3.4), we can study how different soil health indicators and rhizodeposition affect simplified soil systems from a mathematical point of view. First, we start examining the model steady-states and their stability. Consider the system

$$0 = (\mu_c \min^* + \mu_s H(C^*)) B^* - (\epsilon + l) B^*, \quad (3.12a)$$

$$0 = -\frac{\mu_c}{r} \min^* B^* + \epsilon B^* + P^{in}(N^*) - d_1 C^*, \quad (3.12b)$$

$$0 = -\theta \mu_c \min^* B^* + \theta(\epsilon + l) B^* + (\theta_s - \theta) \mu_s H(C^*) B^* + \theta_p P^{in}(N^*) - (P^{out}(N^*) + d_1 N^*). \quad (3.12c)$$

with positive parameters, and we denote $\min^* := \min\{f(N^*), g(C^*)\}$, where the superscript (*) indicates the generic steady state of each variable. We discuss the possible equilibrium points as follows:

- (a) Let $B^* = 0$, and denote $E_0 = (0, C_0^*, N_0^*)$ the boundary steady state. From equation(3.12c), it is possible to compute N_0^* as

$$d_1 N_0^* = \theta_p P^{in}(N_0^*) - P^{out}(N_0^*), \quad (3.13)$$

where $N_0^* > 0$ if $\theta_p P^{in}(N_0^*) > P^{out}(N_0^*)$. Given last condition is satisfied, then C_0^* is directly computed by equation (3.12b),

$$C_0^* = \frac{P^{in}(N_0^*)}{d_1}, \quad (3.14)$$

which is positive.

- (b) Denote the first internal equilibrium as $E_1 = (B_1^*, C_1^*, N_1^*)$ where $B_1^*, C_1^*, N_1^* > 0$ and assume $g(C_1^*) \leq f(N_1^*)$, i.e. $\min^* = g(C^*)$. Consider C_1^* the unique solution of (3.12a), which exists and is unique since it is assumed that $\mu_c > \epsilon + l$, and using equation (3.12b) we describe B_1^* in terms of N_1^* as

$$B_1^*(N_1^*) = \frac{d_1 C_1^* - P^{in}(N_1^*)}{\epsilon - \frac{1}{r} \mu_c g(C_1^*)}, \quad (3.15)$$

where $\epsilon - \frac{1}{r}\mu_c g(C_1^*) > 0$ ($\epsilon - \frac{1}{r}\mu_c g(C_1^*) < 0$) and $d_1 C_1^* - P^{in}(N_1^*) > 0$ ($d_1 C_1^* - P^{in}(N_1^*) < 0$). Note that if we consider C_u^* such that $\epsilon - \frac{1}{r}\mu_c g(C_u^*) = 0$, then $H(C_u^*) = (\epsilon(1-r) + l)(\mu_s)^{-1}$ from equation (3.12a), and $g(C_u^*) = H(C_u^*)$ must be satisfied. This relationship leads to the following expression $\mu_s = (\epsilon(1-r) + l)(r\epsilon)^{-1}\mu_c$, contradicting our assumption for $\mu_s < \mu_c$ since $\epsilon(1-r)(r\epsilon)^{-1} > 0$ and $l > \epsilon > \epsilon r$. Therefore, we can determine that C_u^* is unfeasible from a biological perspective. Using equation (3.12c), N_1^* is given implicitly by

$$N_1^* = \frac{1}{d_1} \left[\theta_s \mu_s H(C_1^*) \left(\frac{d_1 C_1^* - P^{in}(N_1^*)}{\epsilon - \frac{1}{r}\mu_c g(C_1^*)} \right) + \theta_p P^{in}(N_1^*) - P^{out}(N_1^*) \right], \quad (3.16)$$

where $\theta_s \mu_s H(C_1^*) (d_1 C_1^* - P^{in}(N_1^*)) (\epsilon - \mu_c g(C_1^*))^{-1} + \theta_p^{in}(N_1^*) > P^{out}(N_1^*)$ must be satisfied to guarantee N_1^* remains positive.

- (c) Considering $f(N_2^*) \leq g(C_2^*)$, or $\min^* = f(N^*)$, and defining $E_2 = (B_2^*, C_2^*, N_2^*)$ where $B_2^*, C_2^*, N_2^* > 0$, let

$$\mu_c f(N_2^*) + \mu_s H(C_2^*) = \epsilon + l, \quad (3.17)$$

from equation (3.12a), which have a unique solution since $\mu_c > \epsilon + l$. From equation (3.12c), we can compute B_2^* in terms of N_2^* as

$$B_2^*(N_2^*) = \frac{P^{out}(N_2^*) + d_1 N_2^* - \theta_p P^{in}(N_2^*)}{\theta_s (\epsilon + l - \mu_c f(N_2^*))}, \quad (3.18)$$

where $P^{out}(N_2^*) + d_1 N_2^* - \theta_p P^{in}(N_2^*) > 0$ ($P^{out}(N_2^*) + d_1 N_2^* - \theta_p P^{in}(N_2^*) < 0$) and $\theta_s (\epsilon + l - \mu_c f(N_2^*)) > 0$ ($\theta_s (\epsilon + l - \mu_c f(N_2^*)) < 0$). Note that if $\epsilon + l = \mu_c f(N_u^*)$ for some N_u^* , then $\mu_s H(C_u^*) = 0$, which leads to $C_u^* \rightarrow \infty$, which is biologically unfeasible. Then C_2^* can be calculated in terms of N_2^* from (3.12b) as

$$C_2^*(N_2^*) = \frac{1}{r d_1} \left[(-\mu_c f(N_2^*) + r\epsilon) \left(\frac{P^{out}(N_2^*) + d_1 N_2^* - \theta_p P^{in}(N_2^*)}{\theta_s (\epsilon + l - \mu_c f(N_2^*))} \right) + r P^{in}(N_2^*) \right], \quad (3.19)$$

where $-\mu_c f(N_2^*) + r\epsilon > 0$ or $r P^{in}(N_2^*) > (\mu_c f(N_2^*) - \epsilon r) B_2^*(N_2^*)$. In this way, N_2^* can be calculated implicitly by equation (3.12a), or

$$\mu_c f(N_2^*) + \mu_s H(C_2^*(N_2^*)) = \epsilon + l. \quad (3.20)$$

Remark. It is possible to find a parameter set such that both internal equilibria coexist, satisfying $f(N^*) = g(C^*)$ simultaneously (see Figures 3.4a, 3.5). Also, we assume positive parameters, which leads to $C^* > 0$ or $N^* > 0$.

Our model suggests that two internal equilibria may coexist, determined by the availability of labile compounds in the system and the ability of microbes to mineralize SOM to extract required nutrients. These internal steady states represent the symbiotic relationship between plants and microbial communities, whereas the boundary equilibrium represents the inability of soils to sustain microorganisms actively.

3.3.3 Stability analysis

We analyzed the existence of a boundary steady state and two possible internal steady states of (3.4) in the last section. The existence is related to diverse model parameters, including the soil health indicators (μ_s and d_1) and the nitrogen-carbon rhizodeposition ratio (θ_p) [56]. In this section, we study the stability of these steady states.

The Jacobian matrix of (3.4) at E_0 is given by

$$J \Big|_{E_0} = \begin{pmatrix} \mu_c \min^* + \mu_s H(C_0^*) - (\epsilon + l) & 0 & 0 \\ -\frac{1}{r} \mu_c \min^* + \epsilon & -d_1 & P^{in}(N_0^*)' \\ -\theta \mu_c \min^* + (\theta_s - \theta) \mu_s H(C_0^*) + \theta(\epsilon + l) & 0 & \theta_p P^{in}(N_0^*)' - (P^{out}(N_0^*)' + d_1) \end{pmatrix}.$$

Its characteristic polynomial follows as

$$0 = (-d_1 - \lambda)(\mu_c \min^* + \mu_s H(C_0^*) - (\epsilon + l) - \lambda)(\theta_p P^{in}(N_0^*)' - (P^{out}(N_0^*)' + d_1) - \lambda),$$

where $P^{in}(N_0^*)' < 0$ and $P^{out}(N_0^*)' > 0$. The boundary equilibrium $E_0 = (0, C_0^*, N_0^*)$ is locally asymptotically stable (L.A.S.) if and only if

$$\mu_c \min\{f(N_0^*), g(C_0^*)\} + \mu_s H(C_0^*) - (\epsilon + l) < 0. \quad (3.21)$$

For possible internal equilibria, consider first E_1 where $g(C_1^*) < f(N_1^*)$. The Jacobian matrix evaluated at this steady state is given by

$$J \Big|_{E_1} = \begin{pmatrix} \mu_c g(C_1^*) + \mu_s H(C_1^*) - (\epsilon + l) & (\mu_c g'(C_1^*) + \mu_s H'(C_1^*)) B_1^* & 0 \\ -\frac{1}{r} \mu_c g(C_1^*) + \epsilon & -d_1 + \frac{1}{r} \mu_c g'(C_1^*) B_1^* & P^{in}(N_1^*)' \\ J_{\alpha_1} & J_{\alpha_2} & \theta_p P^{in}(N_1^*)' - (P^{out}(N_1^*)' + d_1) \end{pmatrix},$$

where $J_{\alpha_1} = -\theta\mu_c g(C_1^*) + (\theta_s - \theta)\mu_s H(C_1^*) + \theta(\epsilon + l)$, $J_{\alpha_2} = (-\theta\mu_c g'(C_1^*) + (\theta_s - \theta)\mu_s H'(C_1^*))B_1^*$. Its characteristic polynomial is

$$0 = a_0\lambda^3 + a_1\lambda^2 + a_2\lambda + a_3, \quad (3.22)$$

where,

$$a_0 = 1,$$

$$a_1 = 2d_1 + \frac{1}{r}B_1^*\mu_c g'(C_1^*) - \theta_p P^{in}(N_1^*)' + P^{out}(N_1^*)',$$

$$a_2 = \frac{1}{r} \left[B_1^*\mu_s H(C_1^*)' \left(-\epsilon r + \mu_c g(C_1^*) + r(\theta - \theta_s)P^{in}(N_1^*)' \right) + \right.$$

$$B_1^*\mu_c g'(C_1^*) \left(d_1 + l + \epsilon(1 - r) - \mu_s H(C_1^*) + (r\theta - \theta_p)P^{in}(N_1^*)' + P^{out}(N_1^*)' \right) + \left. d_1 r (d_1 - \theta_p P^{in}(N_1^*)' + P^{out}(N_1^*)') \right],$$

$$a_3 = -\frac{1}{r}B_1^* \left[\mu_c \mu_s \left\{ H(C_1^*)g'(C_1^*) - g(C_1^*)H'(C_1^*) \right\} \left(d_1 + (r\theta_s - \theta_p)P^{in}(N_1^*)' + P^{out}(N_1^*)' \right) - \right.$$

$$\mu_c (l + \epsilon(1 - r))g'(C_1^*) \left(d_1 - \theta_p P^{in}(N_1^*)' + P^{out}(N_1^*)' \right) +$$

$$\left. \mu_s r H'(C_1^*) \left(\left\{ (\epsilon + l)\theta_s - \epsilon\theta_p \right\} P^{in}(N_1^*)' + \epsilon(d_1 + P^{out}(N_1^*)') \right) \right].$$

$$(3.23)$$

Note that $g'(C_1^*) \geq 0$, $H'(C_1^*) \leq 0$, $P^{in}(N_1^*)' < 0$ and $P^{out}(N_1^*)' \geq 0$. Therefore, this internal steady state is L.A.S. if and only if $a_2, a_3 > 0$ and $a_1 a_2 > a_3$ by the Routh-Hurwitz criterion [18]. In fact, assuming $a_2, a_3 > 0$, we can reduce and denote the condition $a_1 a_2 - a_3 > 0$ equivalently as

$$\xi_0(B_1^*)^2 + \xi_1 B_1^* + \xi_2 > 0, \quad (3.24)$$

where

$$\xi_0 = \frac{\mu_c}{r^2} \left[\mu_c g'(C_1^*) (d_1 - \epsilon r + \epsilon + l + (r\theta - \theta_p) P^{in}(N_1^*)' + P^{out}(N_1^*)') + \right. \quad (3.25a)$$

$$\left. \mu_s \left(H'(C_1^*) (\mu_c g(C_1^*) - \epsilon r + r(\theta - \theta_s) P^{in}(N_1^*)') - \mu_c H(C_1^*) g'(C_1^*) \right) \right],$$

$$\xi_1 = \frac{1}{r} \left[\mu_c g'(C_1^*) \left(\mu_s H(C_1^*) (r\theta_s P^{in}(N_1^*)' - d_1) + d_1 (3d_1 - \epsilon r + \epsilon + l) + \right. \quad (3.25b)$$

$$P^{in}(N_1^*)' (r\theta - 2\theta_p) (2d_1 + P^{out}(N_1^*)') + 4d_1 P^{out}(N_1^*)' + \theta_p P^{in}(N_1^*)'^2 (\theta_p - r\theta) +$$

$$P^{out}(N_1^*)'^2 \left. \right) + \mu_s H'(C_1^*) \left\{ \mu_c g(C_1^*) (d_1 - r\theta_s P^{in}(N_1^*)') + r P^{in}(N_1^*)' \left(2d_1 (\theta - \theta_s) + \right. \right.$$

$$\left. \left. \theta_s (\epsilon + l) + \theta_p (\theta_s - \theta) P^{in}(N_1^*)' + (\theta - \theta_s) P^{out}(N_1^*)' \right) - d_1 \epsilon r \right\} \right],$$

$$\xi_2 = d_1 (d_1 - \theta_p P^{in}(N_1^*)' + P^{out}(N_1^*)') (2d_1 - \theta_p P^{in}(N_1^*)' + P^{out}(N_1^*)'). \quad (3.25c)$$

In a biological context, the inequality (3.24) can be positively related to soil infiltration rate d_1 since $\xi_2 > 0$, i.e., plant-microbial interactions will remain stable when soil infiltration is sufficient under a simplified soil system. Moreover, as a soil health indicator, the SOM degradation rate μ_s may implicitly affect these interactions, and numerical simulations are needed for further exploration.

For the internal equilibrium E_2 satisfying $f(N_2^*) < g(C_2^*)$, the jacobian matrix is

$$J \Big|_{E_2} = \begin{pmatrix} \mu_c f(N_2^*) + \mu_s H(C_2^*) - (\epsilon + l) & \mu_s H'(C_2^*) B_2^* & \mu_c f'(N_2^*) B_2^* \\ -\frac{1}{r} \mu_c f(N_2^*) + \epsilon & -d_1 & -\frac{1}{r} \mu_c f'(N_2^*) B_2^* + P^{in}(N_2^*)' \\ J_{\beta_1} & J_{\beta_2} & J_{\beta_3} \end{pmatrix},$$

where

$$J_{\beta_1} = -\theta \mu_c f(N_2^*) + \mu_s (\theta_s - \theta) H(C_2^*) + \theta (\epsilon + l),$$

$$J_{\beta_2} = \mu_s (\theta_s - \theta) H'(C_2^*) B_2^*,$$

$$J_{\beta_3} = -\theta \mu_c f'(N_2^*) B_2^* + \theta_p P^{in}(N_2^*)' - (P^{out}(N_2^*)' + d_1).$$

The characteristic polynomial evaluated at this steady state is given by

$$0 = b_0 \lambda^3 + b_1 \lambda^2 + b_2 \lambda + b_3, \quad (3.26)$$

where,

$$\begin{aligned}
b_0 &= 1, \\
b_1 &= 2d_1 + \theta\mu_c f'(N_2^*)B_2^* - \theta_p P^{in}(N_2^*)' + P^{out}(N_2^*)', \\
b_2 &= -\frac{1}{r} \left[\mu_c f'(N_2^*)B_2^* \left(-d_1 r \theta + \mu_s r \theta_s H(C_2^*) - \mu_s (\theta_s - \theta) H'(C_2^*) B_2^* \right) + \right. \\
&\quad \left. \mu_s H'(C_2^*) B_2^* \left(\epsilon r - \mu_c f(N_2^*) + r(\theta_s - \theta) P^{in}(N_2^*)' \right) \right. \\
&\quad \left. - d_1 r (d_1 - \theta_p P^{in}(N_2^*)' + P^{out}(N_2^*)') \right], \tag{3.27} \\
b_3 &= -\frac{1}{r} \mu_s B_2^* \left[d_1 \mu_c r \theta_s H(C_2^*) f'(N_2^*) + H'(C_2^*) \left(d_1 \epsilon r - d_1 \mu_c f(N_2^*) - \right. \right. \\
&\quad \left. \left. \mu_c (l + \epsilon(1-r)) \theta_s f'(N_2^*) B_2^* + \left\{ (\epsilon + l) r \theta_s - \epsilon r \theta_p + \right. \right. \right. \\
&\quad \left. \left. \left. \mu_c (-r \theta_s + \theta_p) f(N_2^*) \right\} P^{in}(N_2^*)' \right) \right].
\end{aligned}$$

Therefore, an internal equilibria $E_2 = (B_2^*, C_2^*, N_2^*)$ is L.A.S. if and only if $b_2, b_3 > 0$ and $b_1 b_2 > b_3$ by Routh-Hurwitz criterion [18]. Taking in account the condition $b_2 > 0$, assuming $b_3 > 0$ and $b_1 b_2 > b_3$, we can express it as $d_1 \eta_1 - \mu_s \eta_0 > 0$, where

$$\begin{aligned}
\eta_0 &= B_2^* \left[-H'(C_2^*) \left((\theta_s - \theta) (B_2^* \mu_c f'(N_2^*) - r P^{in}(N_2^*)') + \right. \right. \\
&\quad \left. \left. \mu_c f(N_2^*) - \epsilon r \right) + \mu_c r \theta_s H(C_2^*) f'(N_2^*) \right], \tag{3.28a}
\end{aligned}$$

$$\eta_1 = r (B_2^* \mu_c \theta f'(N_2^*) + d_1 - \theta_p P^{in}(N_2^*)' + P^{out}(N_2^*)'). \tag{3.28b}$$

Note that $\eta_1 > 0$ and $\eta_0 > 0$, assuming ϵr is small enough. Therefore, the condition $b_2 > 0$ can be framed in a biological context regarding soil health indicators μ_s and d_1 , and we found that the plant-microbial interactions may remain stable when soil infiltration is sufficient, as previously mentioned. Still, in this case, it also depends on the SOM degradation rate, which may result in unstable dynamics for this steady state, especially when soils rich in nutrients are considered. These results are summarized in Table 3.1 and in the following theorem.

Theorem 3. *The equilibria stability of model (3.4) is given as follows:*

1. *The boundary equilibrium E_0 is L.A.S. if and only if $\mu_c \min\{f(N_0^*), g(C_0^*)\} + \mu_s H(C_0^*) - (\epsilon + l) < 0$.*

Steady states and stability conditions summary			
	$E_0 = (B_0^*, C_0^*, N_0^*)$	$E_1 = (B_1^*, C_1^*, N_1^*)$	$E_2 = (B_2^*, C_2^*, N_2^*)$
B_i^*	0	$(d_1 C_1^* - P^{in}(N_1^*))(\epsilon - \frac{1}{r} \mu_c g(C_1^*))^{-1}$	$(P^{out}(N_2^*) + d_1 N_2^* - \theta_p P^{in}(N_2^*))(\theta_s(\epsilon + l - \mu_c f(N_2^*)))^{-1}$
C_i^*	$P^{in}(N_0^*)(d_1)^{-1}$	$(\mu_c g(C_1^*) + \mu_s H(C_1^*)) - (\epsilon + l) = 0$	$(rd_1)^{-1} [(-\mu_c f(N_2^*) + r\epsilon)(P^{out}(N_2^*) + d_1 N_2^* - \theta_p P^{in}(N_2^*))(\theta_s(\epsilon + l - \mu_c f(N_2^*)))^{-1} + rP^{in}(N_2^*)]$
N_i^*	$d_1 N_0^* = \theta_p P^{in}(N_0^*) - P^{out}(N_0^*)$	$\theta_s \mu_s H(C_1^*)(d_1 C_1^* - P^{in}(N_1^*))(\epsilon - \frac{1}{r} \mu_c g(C_1^*))^{-1} + \theta_p P^{in}(N_1^*) - P^{out}(N_1^*) = d_1 N_1^*$	$\mu_c f(N_2^*) + \mu_s H(C_2^*(N_2^*)) = \epsilon + l$
<i>L.A.S.</i>	$\mu_c \min\{f(N_0^*), g(C_0^*)\} + \mu_s H(C_0^*) - (\epsilon + l) < 0$	$a_2 > 0, a_3 > 0$ and $\xi_0(B_1^*)^2 + \xi_1 B_1^* + \xi_2 > 0$	$b_2 = d_1 \eta_1 - \mu_s \eta_0 > 0, b_3 > 0$ and $b_1 b_2 > b_3$

Table 3.1: Steady states and stability conditions summary. Each column represents the steady state $E_i = (B_i^*, C_i^*, N_i^*)$ and how each term is computed. If an expression is in terms of an equation, then the value must be computed implicitly. Otherwise, the value is given explicitly. The local asymptotically stable (L.A.S.) conditions are given in terms of variables defined in section 3.3.3.

2. The internal equilibrium E_1 is L.A.S. if and only if $a_2 > 0, a_3 > 0$ and $\xi_0(B_1^*)^2 + \xi_1 B_1^* + \xi_2 > 0$, where a_2, a_3 are defined in (3.23) and ξ_0, ξ_1 and ξ_2 are defined in (3.25).
3. The internal equilibrium E_2 is L.A.S. if and only if $b_2 = d_1 \eta_1 - \mu_s \eta_0 > 0, b_3 > 0$ and $b_1 b_2 > b_3$, where b_1, b_3 are defined in (3.27), and η_0, η_1 are defined in (3.28).

3.3.4 Persistence-extinction criteria

In the previous section, we analyzed the local behaviour of solutions. We now shift our focus to their global behaviour and establish criteria for the persistence and extinction of bacterial biomass.

The theorem below outlines a criterion for persistence. Theorem 3 demonstrated that when $\mu_c \min\{f(N_0^*), g(C_0^*)\} + \mu_s H(C_0^*) - (\epsilon + l) > 0$, the boundary equilibrium E_0 is unstable. Under the same condition, we now show that the boundary equilibrium is unstable and sustains a uniform lower bound, as further explained in the subsequent theorem.

Theorem 4. *If $\mu_c \min\{f(N_0^*), g(C_0^*)\} + \mu_s H(C_0^*) - (\epsilon + l) > 0$, then the bacteria are robustly uniformly persistent: there exist $\eta > 0$ such that*

$$\liminf_{t \rightarrow \infty} B(t) \geq \eta, \quad (3.29)$$

for all solutions of (3.4) with $B(0) > 0$.

Proof. Let $X_0^B = \{(B, C, N) \in \mathbb{R}^3 | B = 0\}$ and ϕ^t be the flow generated from system (3.4). Take any $u_1(t) = (B_1, C_1, N_1)$ with initial value $u_1^0 \in X_0^B$. One can show $B_1(t) = 0$ for all forward time from equations (3.4). Then the ω -limit set of $u_1^0 \in X_0^B$ is given by

$$\omega(u_1^0) = \{(B, C, N) \in X_0^B : \phi^{t_k}(u_1^0) \rightarrow (B, C, N) \text{ for some sequence } t_k \rightarrow +\infty\}.$$

It follows that

$$N_1' = \theta_p P^{\text{in}}(N_1) - (P^{\text{out}}(N_1) + d_1 N_1), \quad \forall t \geq 0.$$

Let $F(N) = \theta_p P^{\text{in}}(N) - (p^{\text{out}}(N) + d_1 N)$. Note that $F(N)$ is a decreasing function over N . Therefore, if $N(t) < N_0^*$, then $N'(t) = F(N) > F(N_0^*) = 0$. $N(t)$ will then increase. If $N(t) > N_0^*$, then $N'(t) = F(N) < F(N_0^*) = 0$. $N(t)$ will then decrease. Therefore, $\lim_{t \rightarrow +\infty} N_1(t) = N_0^*$. Hence, $\omega(u_1^0) \subset \{(B, C, N) : B = 0, N = N_0^*\}$.

Take any $u_2(t) = (B_2, C_2, N_2)$, where $u_2^0 = (B_2(0), C_2(0), N_2(0)) \in \omega(u_1^0)$. One can show $B_2(t) = 0$ and $N_2(t) = N_0^*$ for all forward time from equations (3.4). Then, we have

$$C_2' = P^{\text{in}}(N_0^*) - d_1 C_2, \quad \forall t \geq 0.$$

Then $\lim_{t \rightarrow +\infty} C_2(t) = C_0^*$. Hence, $\omega(u_2^0) \subset \{(0, C_0^*, N_0^*)\}$. Therefore, all solutions of system (3.4) with initial value $(0, C_1(0), N_1(0)) \in X_0^B$ converge to $(0, C_0^*, N_0^*)$ eventually. i.e. $\forall u_1^0 \in \bar{\Omega}_1 \cap X_0^B$, $\omega(u_1^0) = \{(0, C_0^*, N_0^*)\}$.

Let

$$R(\epsilon) = \mu_c \min\{f(N_0^*), g(C_0^*)\} + \mu_s H(C_0^*) - (\epsilon + l), \quad (3.30)$$

then $R(\epsilon) > 0$. Following Corollary 4.7 in [73], let $T = 1$, $M = \bar{\Omega} \cap X_0^B$, we have $\Omega(M) = \{(0, C_0^*, N_0^*)\}$ and $r(P(T, z)) \geq e^{R(\epsilon)} > 1$, $\forall z \in \Omega(M)$. Therefore, the Lyapunov exponent is positive. Thus, for any $B(0) > 0$, there exists a $\eta > 0$, such that $\liminf_{t \rightarrow \infty} B(t) \geq \eta$. This completes the proof. \square

Therefore, when $\mu_c \min\{f(N_0^*), g(C_0^*)\} + \mu_s H(C_0^*) - (\epsilon + l) > 0$, the bacterial biomass will never go extinct. Now, we consider the extinction criteria. The following theorem provides a sufficient condition for bacterial extinction.

Theorem 5. *If $\mu_c \min\left\{f\left(\frac{2\alpha^{\text{in}}(1+\theta_p)}{d_1}\right), g\left(\frac{2\alpha^{\text{in}}(1+\theta_p)}{d_1}\right)\right\} + \mu_s - \epsilon - l \leq 0$, $\frac{1}{r}L_1 + L_2 \leq 0$ and $\frac{1}{r} - (\theta_s - \theta) > 0$, then for all $(B(0), C(0), N(0)) \in \Omega_1$, $(B(t), C(t), N(t)) \rightarrow (0, C_0^*, N_0^*)$, as $t \rightarrow +\infty$.*

Proof. Let

$$\Omega_1 = \left\{ (B, C, N) : B > 0, C > 0, N > 0, \left(\frac{1}{r} - (\theta_s - \theta)\right) B + C + N < \frac{2\alpha^{\text{in}}(1 + \theta_p)}{d_1} \right\} \subset \mathbb{R}^3 \quad (3.31)$$

and $\bar{C} = \bar{N} = \frac{2\alpha^{\text{in}}(1+\theta_p)}{d_1}$. Let $u_1(t) = (B_1(t), C_1(t), N_1(t))$ with initial value $u_1^0 = (B_1(0), C_1(0), N_1(0)) \in \Omega_1$. By Theorem 1, if $\frac{1}{r}L_1 + L_2 \leq 0$ and $\frac{1}{r} - (\theta_s - \theta) > 0$, for each $u_1^0 \in \Omega_1$, the forward orbit $\{\phi^t(u_1^0) : t > 0\}$ is bounded and $C_1(t) < \bar{C}$ and $N_1(t) < \bar{N}$ for all $t \geq 0$. Thus,

$$B_1' \leq (\mu_c \min\{f(\bar{N}), g(\bar{C})\} + \mu_s - \epsilon - l) B_1, \quad \forall t \geq 0.$$

Since $\mu_c \min\left\{f\left(\frac{2\alpha^{\text{in}}(1+\theta_p)}{d_1}\right), g\left(\frac{2\alpha^{\text{in}}(1+\theta_p)}{d_1}\right)\right\} + \mu_s - \epsilon - l \leq 0$, we have that $B_1'(t) \leq 0$ for all $t \geq 0$. Suppose $B_1(0) > 0$, then $B_1(t)$ converges to \bar{B} . Therefore, $\omega(u_1^0) \subset \{(B, C, N) : B = \bar{B}\}$. If a equilibrium point $(B^*, C^*, N^*) \in \omega(u_1)$, then $B^* = \bar{B}$. In fact $\bar{B} = 0$, otherwise $\bar{B} > 0$, $C^* < \bar{C}$ and $N^* < \bar{N}$, it follows that

$$\begin{aligned} 0 &= (B^*)' = (\mu_c \min\{f(N^*), g(C^*)\} + \mu_s H(C^*) - \epsilon - l) B^* \\ &< (\mu_c \min\{f(\bar{N}), g(\bar{C})\} + \mu_s - \epsilon - l) B^* \leq 0, \quad \forall t \geq 0, \end{aligned}$$

which is a contradiction. Hence $\omega(u_1^0) \subset \{(B, C, N) : B = 0\}$.

By similar argument in Theorem 4, we can show that for all solution with initial value $u_2^0 \in \omega(u_1^0)$, the ω limit set $\omega(u_2^0) \subset \{(B, C, N) : B = 0, N = N_0^*\}$; and for all solution u_3 with initial value $\in \omega(u_2^0)$, the ω limit set $\omega(u_3^0) \subset \{(0, C_0^*, N_0^*)\}$. i.e. for all solution of system (3.4) with initial value in Ω_1 , the solution converges to $(0, C_0^*, N_0^*)$ eventually. \square

Note that $\mu_c \min \left\{ f \left(\frac{2\alpha^{\text{in}}(1+\theta_p)}{d_1} \right), g \left(\frac{2\alpha^{\text{in}}(1+\theta_p)}{d_1} \right) \right\} + \mu_s - \epsilon - l \leq 0$ implies that $\mu_c \min \{f(N_0^*), g(C_0^*)\} + \mu_s H(C_0^*) - (\epsilon + l) < 0$. Therefore, from the local stability results in Theorem 3 and the global attractiveness in Theorem 5, we deduce the global stability of the boundary equilibrium E_0 .

Theorem 6. *If $\mu_c \min \left\{ f \left(\frac{2\alpha^{\text{in}}(1+\theta_p)}{d_1} \right), g \left(\frac{2\alpha^{\text{in}}(1+\theta_p)}{d_1} \right) \right\} + \mu_s - \epsilon - l \leq 0$, $\frac{1}{r}L_1 + L_2 \leq 0$ and $\frac{1}{r} - (\theta_s - \theta) > 0$, $E_0(0, C_0^*, N_0^*)$ is globally stable.*

Our extensive mathematical findings cover aspects such as well-posedness, long-term behaviour, stability, microbial persistence and extinction criteria. In the following section, we apply our mathematical findings to discuss the model predictability outcomes through numerical experiments.

3.4 Numerical experiments

The rhizodeposit's dynamic influence on plant-microbial interactions can be explored through simulations, extending our theoretical results found from the model's mathematical analysis. In this section, we study the model (3.4) predictions based on soil infiltration and SOM degradation rate as simplified soil health indicators to explore bifurcations, transient dynamics, rhizodeposits influence on microbial activities and increased labile- N bioavailability outcomes. We explore how these simplified soil features determine the plant's approximate use of rhizodeposits and SOM mineralization trade-offs. The parameters used for the following simulations are listed in Table 3.2, which remained fixed unless stated otherwise. Our numerical results were performed using a combination of XPP/XPPAut (mainly for bifurcation diagrams) and MATLAB.

3.4.1 Soil health

To understand plants' use of energy and resources as rhizodeposits to promote their growth through enhancing microbial activities and uptaking released nutrients from SOM mineralization, we consider biodegradation soil mechanisms and soil quality indicators, or in more general terms, soil health indicators [31]. These indicators include

Param.	Definition	Value [Range]	Unit	Ref.
μ_c	Max. growth rate for labile C	8.31	day^{-1}	[96]
μ_s	Oligotroph SOM degradation rate	2.526	day^{-1}	Free Parameter (S.H.I.)
l	Respiration rate	3.05	day^{-1}	[96]
ϵ	Microbial death rate	0.1	day^{-1}	[62]
r	Yield constant	0.104	-	[96]
θ	Microorganisms N:C ratio	0.2	-	[83]
θ_s	SOM decomposition N:C ratio	0.3946	-	[96]
K_f	N -dependent H.S.C. for microorganisms growth	2.9	$\mu\text{g N g soil}^{-1}$	[62]
K_g	C -dependent H.S.C. for microorganisms growth	30	$\mu\text{g C g soil}^{-1}$	[57], [62]
K_h	C -dependent H.S.C. for microorganisms strategy	474.78	$\mu\text{g C g soil}^{-1}$	[96]
α^{in}	Rhizodeposition	3.6	$\mu\text{g C g soil}^{-1} \text{day}^{-1}$	Free parameter (fixed)
α_{out}	Plant maximum N uptake rate	2 [1.36 - 5.75]	$\mu\text{g N g soil}^{-1} \text{day}^{-1}$	[82]
β_C	Rhizodeposition threshold	10	$(\mu\text{g N g soil}^{-1})^{-1}$	Free parameter (fixed)
β_N	Plant uptake N -dependent H.S.C.	25 [5 - 63]	$\mu\text{g N g soil}^{-1}$	[82]
d_1	Soil infiltration rate	0.0222 [> 0]	day^{-1}	Free parameter (S.H.I.)
θ_p	Rhizodeposition N:C ratio	0.1 [0,0.1]	-	[50]

Table 3.2: List of parameters used for the numerical simulation. H.S.C. (S.H.I.) stands for half-saturation constant (soil health indicator). The plant's rhizodeposits depend on different soil features, including soil nutrients bioavailability, pH, temperature, moisture, etc. These delimiting rhizodeposits features are simplified in terms of free parameters but remain fixed through the simulations unless stated otherwise.

the organic matter stratification in soils, soil infiltration, conservation and flow of nutrients. For example, in Figure 3.1, we plot different solutions using equations (3.4) with initial conditions $(B(0), C(0), N(0)) = (0.033, 2.603, 0.498)$, varying the soil infiltration and SOM degradation rate as simplified soil health indicators.

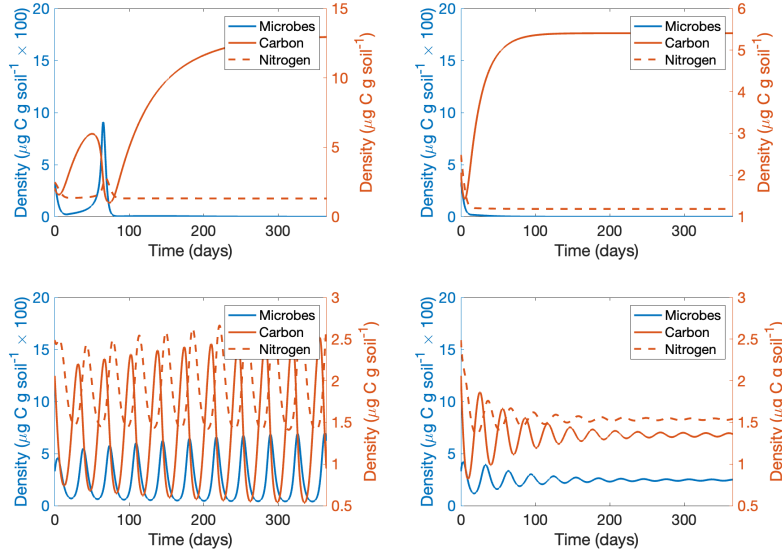


Figure 3.1: Numerical simulations from equation (3.4) with initial condition $(B(0), C(0), N(0)) = (0.033, 2.603, 0.498)$. The soil infiltration (d_1) and the SOM degradation rate (μ_s) are varied as indicators for soil quality status, and other parameters are fixed as in Table 3.2. (Top panels): Simulation reached the boundary steady state with $d_1 = 0.02$ top-left ($d_1 = 0.062$ top-right) and $\mu_s = 2.5$. (Bottom panels): Simulation reached a periodic solution and to an internal steady state with $d_1 = 0.02$ bottom left ($d_1 = 0.062$ bottom right) and $\mu_s = 2.8$. Note: The nitrogen transients are shown as $\theta^{-1}N(t)$ for comparison with $B(t)$ and $C(t)$ only in this case.

The numerical results from Figure 3.1 show that the rhizodeposits and soil health indicators are related intrinsically in this model, which will be explored more in detail in the following subsections. Varying only the soil infiltration and oligotroph SOM degradation rate, implicitly containing information on fixed SOM C/N stoichiometric ratio, we can measure how plants (and microbes) benefit given on different simplified soil health indicators. A periodic solution may arise given that the persistence criterion is satisfied (see section 3.3.4), and Figure 3.2 assists in visualizing this result. From these simulations, we can observe that the bioavailability of C and N in this simpli-

fied soil system may guarantee the survival of microbes. Furthermore, depending on soil health indicators, rhizodeposits may enhance SOM mineralization by sustaining microbes' activities, increasing N soil bioavailability, and indirectly improving plant growth.

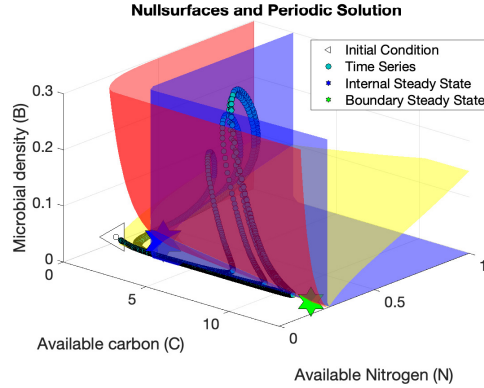


Figure 3.2: Three-dimensional transient dynamics. The parameters and initial condition (white triangle) are used as in Figure 3.1 (bottom-left panel). The nullsurfaces are represented in blue (B -nullsurface), red (C -nullsurface) and yellow (N -nullsurface). The time series is represented in blue dots, and the internal and boundary steady states are in stars (blue and green, respectively). The solution $(B(t), C(t), N(t))$ for $t > 0$ reaches close to E_0 at the beginning of the simulation, goes away from it and finalizes orbiting around E_1 .

3.4.2 Bifurcation analysis

Understanding soil health indicators under numerical experiments may provide insights into soil research experiments. The simulations in Figure 3.1 (bottom-right) show that periodic solutions can be stabilized for different soil indicator ranges, suggesting that soil nitrogen bioavailability may occur periodically or constantly, delimiting the need for plant use of rhizodeposits for microbial growth promotion and SOM mineralization. The following bifurcation diagrams extend our numerical results and allow us to study in more depth model (3.4) under the parameters given in Table 3.2, varying soil health indicators and rhizodeposits N/C ratios.

Bifurcation over the SOM degradation rate

For the following bifurcation diagrams, we use the soil infiltration and the SOM degradation rate as soil health indicators. First, fixing the soil infiltration rate and rhizodeposit N/C ratio (see Table 3.2), we vary μ_s , which implicitly measures the SOM carbon-to-nitrogen content as the microbial SOM degradation rate [96]. In Figure 3.3, we show the one-dimensional bifurcation diagram for the variables B , C and N in terms of μ_s .

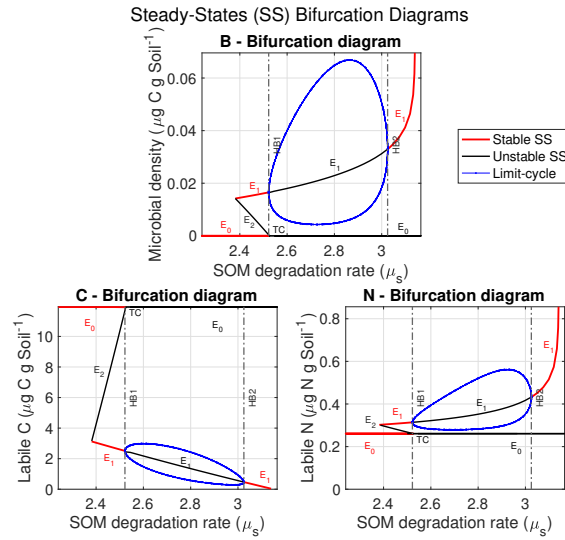


Figure 3.3: Bifurcation diagram for model (3.4), fixing the parameters as in Table 3.2 and varying μ_s a soil health indicator. Three panels represent the bifurcation diagram for microbial communities (B), labile carbon in soil (C), and labile nitrogen in soil (N), and E_i for $i = 0, 1, 2$ denotes the stable (red) or unstable (black) system equilibria. A transcritical bifurcation occurs (TC) and corresponds to the boundary steady state E_0 at $\mu_s = 2.525$. The emergence of internal steady states occurs around $\mu_s = 2.381$ and a bistability region with it between E_0 and E_1 . Furthermore, a Hopf-Bifurcation (HB1 for the left branch and HB2 for the right branch) also emerges on the interval $\mu_s = [2.522, 3.02]$ and the maximum and minimum of the orbits are represented in blue.

When the infiltration rate and rhizodeposits N/C ratio remain fixed and positive, we can observe from Figure 3.3 that the survival of microorganisms does not depend only on the plant's rhizodeposits but also on soil quality. A threshold was found using the set of parameters in Table 3.2 and delimits a transcritical bifurcation that indicates

the minimum requirement for the SOM C/N ratio content (implicitly measured by μ_s) that may guarantee microbial persistence. Furthermore, we found a range where oscillations occur, suggesting a periodic input of plant rhizodeposits due to a periodic increase and decrease in N bioavailability mineralized by soil microbial communities. However, for soils rich in SOM C/N content, the model (3.4) suggests a stabilized and constant symbiotic relationship between plants and microbes.

Bifurcation over multiple parameters

Soil degradation rate and soil infiltration can be used as an indicator to determine immobilization/mineralization of soil nutrients, where rhizodeposits C/N content may vary depending on the type of plant and soil conditions [31], [61], [95]. This section uses two-parameter bifurcation diagrams to investigate the relationship between SOM mineralization with soil infiltration rates and N/C rhizodeposition ratios. In Figure 3.4, we plot a two-parameter bifurcation diagram to show how the infiltration and the SOM degradation rates influence the transient dynamics of model (3.4).

The two-parameter bifurcation diagram for soil infiltration and SOM degradation rate as soil health indicators reveals the coexistence of both internal steady states. The stability of the internal steady state E_1 is partitioned into two regions (blue for stable and red for unstable); meanwhile, E_2 remains unstable and approximated by a two-dimensional scattered region in yellow to avoid colours overlapping (see Figure 3.4). The transcritical bifurcation (green line) for the boundary equilibrium persists over the two-dimensional plot, dividing the microbial extinction (left of the partitioned region) and persistence (right of the partitioned region), delimiting the model's bistability and limit cycle regions.

In Figure 3.4, we have used the two simplified soil health indicators, and we found that soil infiltration rate can stabilize microbial growth when the SOM C/N ratio content is suitable for microbial proliferation. To study the impact of rhizodeposition N/C ratio on the stability of steady states, we use Figure 3.5, a two-parameter bifurcation diagram in terms of θ_p and μ_s by fixing d_1 , which shows a similar qualitative behaviour compared to Figure 3.4a, modifying only the unstable region for E_1 . The transcritical

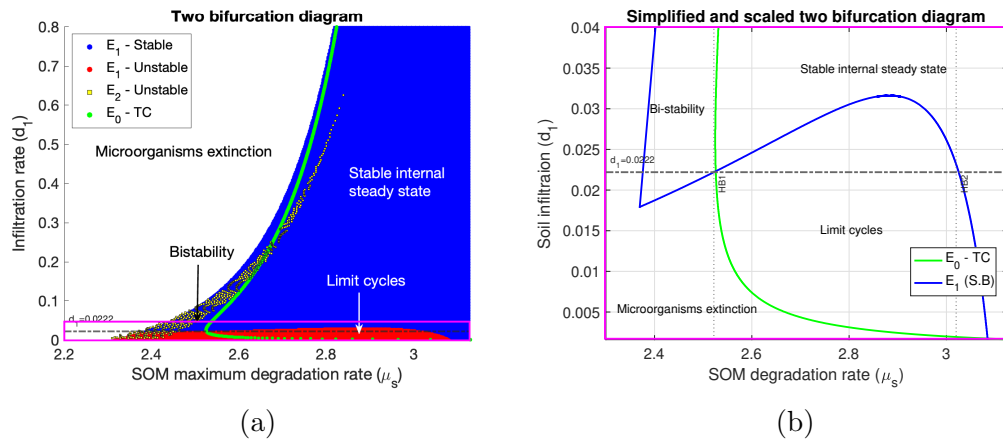


Figure 3.4: Two-parameter bifurcation diagram for d_1 and μ_s as soil health indicators, where TC (S.B) stands for Transcritical (Stable Boundary). In Figure 3.4a, the stability of internal steady-state E_1 is represented in blue (stable) and red (unstable). The E_0 TC bifurcation divides the region into a stable (left) and unstable (right) steady state. The steady-state E_2 remains unstable, and a scatter plot in yellow approximately represents its region, avoiding a complete colour overlap. Figure 3.4b simplifies and rescales the magenta region in Figure 3.4a, representing only the contour of the stable steady-state E_1 and the TC bifurcation for reference to other numerical experiments. The dashed line $d_1 = 0.022$ indicates the fixed parameter during some of our simulations.

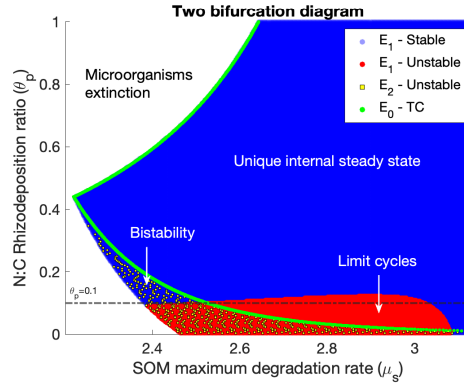


Figure 3.5: Two-parameter Bifurcation diagram for θ_p and μ_s , representing the N/C rhizodeposition ratio and a soil health indicator, respectively. The qualitative behaviour of steady states is similar and fully described in Figure 3.4a. However, the unstable steady state region for E_2 (a scatter plot in yellow represents the region and avoids colour overlap) is now contained in the bistability and the intersection of the unstable E_1 and microbial extinction region. The dashed line $\theta_p = 0.1$ indicates the fixed parameter for other simulations as reference. Note that high values used for θ_p ratios may be unrealistic regarding rhizodeposits but can be assumed if fertilizers input is also considered and is only used for numerical prediction purposes.

bifurcation for the boundary steady-state E_0 delimits the microbial extinction (left region) and persistence (right region). The internal steady states may coexist, but E_2 remains unstable (a scattered plot in yellow avoids approximates and highlights this region) as in Figure 3.4a, overlapping the region where microbes extinction is stable, and E_1 can be stable or unstable.

3.4.3 Rhizodeposition, mineralization and immobilization

Soil health indicators gauge soil's capacity to sustain plant growth [61]. However, N bioavailability moderates the interconnection between soil, plants and microbes through the plant rhizodeposition, promoting microorganisms' SOM mineralization and, thus, increasing labile N availability [9], [68]. Figures 3.4, 3.5 show the existence of different regions where microbial communities may persist and their growth fluctuation can be stabilized due to increased soil infiltration capacity or high N/C rhizodeposition ratios. Assuming a fixed soil infiltration rate and N/C plant's rhizodeposition, in this section, we study the plant's trade-off of investing energy and resources to microbes through

rhizodeposits with the increased N -bioavailability due to SOM mineralization. First, we define the cumulative trade-off of the plant's labile substrates deposited to the rhizosphere (λ_{μ_s}) as

$$\lambda_{\mu_s} = \int_0^{\tau} (\theta_s - \theta)\mu_s H(C)B - \theta_p P^{in}(N) dt, \quad (3.32)$$

where the subscript μ_s denotes the corresponding SOM degradation rate value and τ is the time for which the cumulative nutrients trade-off is measured. For example, if the soil health indicators are related to the limit cycle, we denote τ as its period. The sign of λ_{μ_s} value represents the positive (negative) feedback, i.e., how much labile N becomes bioavailable comparing plant exudates through its roots with microbial SOM mineralization. If $\lambda_{\mu_s} > 0$ ($\lambda_{\mu_s} < 0$), then the increased N -bioavailability comes mainly from SOM mineralization (rhizodepositions) sources. In Figure 3.6, we plot different values of λ_{μ_s} using Table 3.2, and fixing the integration interval τ as the correspondent limit cycle period, or by the lower (upper) limit cycle period if μ_s is before (after) the Hopf-bifurcation for consistency purposes.

By using λ_{μ_s} to quantify the plants' rhizodeposition trade-off with microbial SOM increased mineralization, we can determine when the plants' investment of nutrients and energy may pay off or account for resource losses depending on the two soil health indicators. In Figure 3.6, we denote a positive N feedback in blue colour when the $\lambda_{\mu_s} > 0$, indicating that plants' rhizodeposits will increase microbial biomass, SOM mineralization and N bioavailability. Otherwise, negative feedback (red) indicates that plants' rhizodeposits will not be able to promote microbial SOM mineralization, leading to resource waste. Part of the nutrient dynamics also depends on microbial labile N -immobilization, and Figure 3.6 shows the amount of cumulative N uptaken by microbes by integrating absolutely the first term of equation (3.3) ($\theta\mu_c \min\{f(N), g(C)\}B$). From this simulation, it can be pointed out a threshold given by the SOM degradation rate ($\mu_s \approx 2.8$) as a soil health indicator that separates the rhizodeposition positive and negative feedback, and which the microbes would immobilize all available labile N from rhizodeposits and SOM mineralization sources. On the one hand, if the soil quality is less than this threshold, only microbial communities benefit from rhizodeposition. On

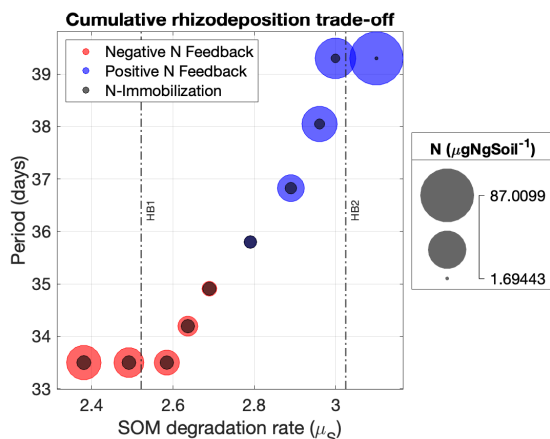


Figure 3.6: Plants rhizodeposits may increase overall N bioavailability by promoting microbial biomass and SOM mineralization depending on soil health indicators. The positive (negative) feedback denotes a cumulative increase of bioavailable N surplus from SOM mineralization (rhizodeposits) as the main source. The time interval to quantify such measurements is taken by the periodic limit cycles correspondent to the Hopf-bifurcation in Figure 3.3. The radius of each bubble denotes $|\lambda_{\mu_s}|$, where λ_{μ_s} is defined in equation (3.32), representing the absolute cumulative rhizodeposition trade-off and its scale is given by the panel on the right. The cumulative microbial N -immobilization is represented in black and is given by integrating the N uptake rate by microbes over the specified period.

the other hand, if the soil quality exceeds this threshold, the plants will benefit by using part of their resources to increase microbial activities that mineralize SOM. In particular, if the SOM quality exceeds the right Hopf-bifurcation (HB2), N -bioavailability is comparatively greater than microbial immobilization. This phenomenon can be related to the priming effect, i.e., a rapid increase of SOM mineralization by inputting labile substrates into soil [14], [49], [60], [96].

The numerical experiment for the positive and negative rhizodeposition plant' trade-off to promote microbial SOM mineralization highlights a threshold that delimits plants' benefits after investing in rhizodeposits over a period in relation to soil health indicators (see Figure 3.6). It also measures the immobilized microbial labile N amount, which is comparatively lower for greater-quality soils, where their growth and SOM mineralization are substantially increased along with N bioavailability. To quantify this trade-off, in Figure 3.7, we measure the cumulative N -rhizodeposition versus

the SOM-derived N due to increased microbial activities over a period τ separately, providing clearer information regarding plants' investment against N return from SOM mineralization in different regions defined by soil health indicators.

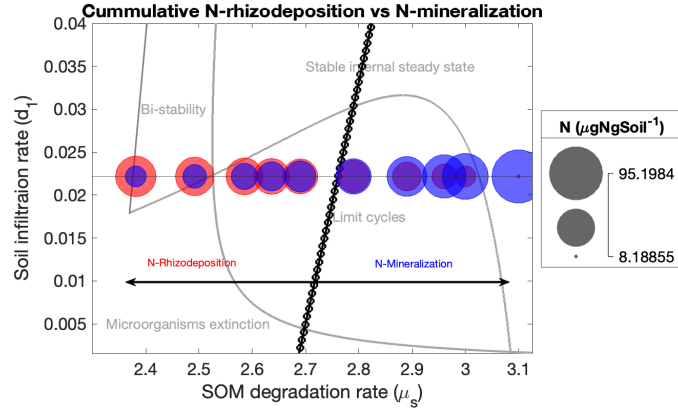


Figure 3.7: Comparison between N -rhizodeposition (red) versus N -mineralization (blue) subject to soil quality indicators d_1 and μ_s . The two-parameter bifurcation diagram from Figure 3.4b (grey) is on the background to show the cumulative N surplus given different stability regions. The threshold by which N -rhizodeposition equals N -mineralization over a period τ (see Figure 3.6) is plotted as a line with black circles in terms of the soil quality indicators. This threshold separates the region where the cumulative N -mineralization (right region) and N -rhizodeposition (left region) increases with respect μ_s . The panel on the right represents the N scales for each mechanism.

In Figure 3.7, we separately compute the cumulative release of labile N from SOM mineralization (blue) and rhizodeposition input (red) over the period τ (see Figure 3.6), varying the soil health indicator (μ_s) to distinguish cumulative N -mineralization versus N -rhizodeposition amounts. Considering the SOM quality threshold implicitly given by μ_s as in Figure 3.6, it is possible to compare the amount of N -rhizodeposits invested against N -released from SOM mineralization. This numerical experiment shows that the soil quality is inversely proportional to the rhizodeposit amount required to increase N bioavailability and directly proportional to microbial capacity to mineralize SOM. The higher the soil quality, the fewer rhizodeposits are required to promote SOM mineralization and plant growth, i.e., plants can promote the priming effect using low amounts of rhizodeposits in rich soils. However, the threshold represented in black circles (extended over the infiltration value d_1) indicates when the plants'

rhizodeposits are insufficient to promote sufficient SOM mineralization, reducing the cost-benefit of investing their resources to grow. Our results show this threshold to be linearly dependent on soil health indicators, suggesting that greater soil infiltration rates would proportionally require higher soil quality to benefit plant growth.

3.5 Discussion

The agricultural sector’s increased interest in developing suitable tools to promote rural sustainability, such as food security with reduced input of anthropogenic fertilizers and no-tillage strategies, has led soil quality experts to establish and create different soil health indicators and laboratory methods [19], [20]. Soil health, defined as “The capacity of the soil to function as a vital living ecosystem that supports plants, animals and humans.” by the NRCS, provides a background to define soil quality features and delimits current critical indicators that are mainly related to soil structural stability (soil infiltration), SOM carbon-to-nitrogen contents (providing potential bioavailability of labile N), and general microbial activities (which are principal SOM decomposers) [61], [84]. Also, by studying the rhizosphere, a spatial and temporarily heterogeneous zone where the interactions between plants and microbes occur, as a key component of the soil N cycle, strategies that reduce the input of fertilizers could be developed [9], [68]. The relationship between soil health indicators and plant use of rhizodeposits is inherently correlated. Still, current methodologies to quantify plants’ root exudates involve destructive sampling, making it challenging to quantify and understand the symbiotic relationship between plants and microbes in the rhizosphere [33], [61], [63].

Mechanistic mathematical models provide a non-invasive conceptual tool that can contribute to the rhizosphere complex dynamics understanding [12], [33]. In this work, we presented a stoichiometric mathematical model that is based on a previously validated one that incorporates experimental laboratory data that shows SOM-increased mineralization by adding different labile substrates mediated by different microbial communities [96]. Our model simplifies the complexity of soil plant-microbial dynamics through rhizodeposits by incorporating soil health indicators such as an implicit measurement of the SOM quality content and soil infiltration rates. In this way, we

identified how these indicators may affect the interactions between soil, plants and microorganisms, contributing to a further understanding of soil nutrient cycles when considering different soil features.

Through a series of different bifurcation diagrams and numerical experiments, we described how the soil health indicators play a role in the rhizosphere. Sufficient soil infiltration rates can mitigate the periodic necessity of plants' exudates to indirectly increase N -bioavailability by promoting microorganism growth and SOM mineralization. This result can be related to the soil structural stability, specifically soil aggregates that mediate hydrologic and biological processes by infiltrating and draining beneficial amounts of water, strengthening the importance of no-tillage strategies [84]. Our model also highlights a linear relation between soil infiltration and quality that can be used to determine the impact of rhizodeposits in SOM mineralization. This relation predicts when microorganisms immobilize the available labile N entirely from different sources (root exudates and soil), distinguishing regions in which plants' use of energy and resources will benefit themselves by indirectly increasing soil nutrient availability derived from SOM mineralization. We also found that higher-quality soils require less N -rhizodeposits over time to increase SOM mineralization with the possibility of promoting the priming effect, and low-quality soils require more frequent input of rhizodeposits, in which fertilizers use may be a suitable option in this case.

The model predictions mentioned above are mathematically and numerically justified. Still, different limitations are present, which have to be addressed in future research. For example, we consider nitrogen the main limiting nutrient, but in some specific scenarios, phosphorus can be limiting instead [60], [83]. SOM mineralization dynamics were simplified by using a fixed soil health indicator, which, in reality, the SOM carbon-to-nitrogen ratio may vary at different rates over time and can dramatically decrease when priming effects are present. Incorporating SOM degradation dynamics in the model with different soil features, including soil temperature, pH, irrigation, nutrient cycling from protozoa grazing, etc., can improve the understanding of rhizodeposition effects on soil. However, our model may provide a basis to open new research directions toward the benefit of agricultural management.

Chapter 4

Temperature-dependent mechanistic model to predict methane biogenesis from an oil sands tailings settling basin

4.1 Introduction

The world's third-largest identified oil reservoir belongs to Canada's oil sands reserve in Alberta, representing about 166.3 billion barrels (<https://natural-resources.canada.ca/>). Oil sands are a natural mixture of sand, minerals, bitumen and water, and in Alberta, 20% of the reserve is suitable for open-pit mining operations (<https://www.alberta.ca/oil-sands-overview>). As with many oil-operating mining sites, the tailings produced after mining and separating the bitumen from oil sands are stored in large basins or oil sands tailing ponds (OSTPs) [37]. An increase in mining waste has adverse effects on the environment, and in particular, Alberta's OSTPs have continuously produced methane derived from hydrocarbon biodegradation processes since 1990 [69], [88]. There are no current estimations for when it will cease or how much would be expected over the years [27], [35], and the federal government of Canada recently announced the 2030 Emissions Reduction Plan, which partially aims to reduce 40% of Canada's current methane emissions compared to 2005 levels by 2030 and reach net-zero emissions by 2050 (<https://www.canada.ca>). Consequently, developing accurate tools, including data-validated mathematical models, is crucial to estimating methane emissions from

oil sand mining activities over time and assessing ongoing efforts to fulfill methane-reducing strategies as needed.

Alberta's principal anthropogenic methane emissions mainly originate from the oil and gas industry, a sustained portion of which is from OSTP and end-pit lakes (EPL) in oil sand territories (<https://www.aer.ca/>). Bitumen extraction from oil sands produces continuous input of fluid fine tailings (FFT) into OSTP, which may actively support methane emissions over time [27]. FFTs are a byproduct of a mixture of sands, clays, and unrecovered hydrocarbon residuals during the bitumen extraction process from oil sands, which are suitable to support methane biogenesis [69], [77]. Compared to OSTPs, EPLs are controlled in-field water-capped ponds containing a fixed amount of wet FFTs, and their use is to recover water previously used, reducing fresh water usage during bitumen separation [27]. EPLs are ongoing land reclamation technologies to reincorporate mined lands to their natural state [41]. Now, an unrecovered fraction of hydrocarbons, including naphtha and paraffinic diluents used during bitumen extraction, in OSTPs and EPLs are now a primary source of methane biogenesis and constitute a long-term process, difficulting the ongoing goals of creating suitable land reclamation scenarios and methane mitigation [27], [80], [81]. Still, tailing's methanogenesis processes are beneficial for reducing acute toxicity in ponds and accelerating water pore recovery [27]. Providing insights on this process, such as the methane expected and the longevity of the process under *in situ* features, could be essential for tailings management control and, consequently, methane emissions mitigation.

Diluents such as naphtha, petroleum distillate containing short-chain n-alkanes, BTEX (benzene, toluene, ethylbenzene and xylene isomers), and light paraffinic diluents, comprising mainly C5-C6 alkanes, are used during the bitumen separation from oil sands [11]. Laboratory research has consistently shown that the biodegradation of short-chain n-alkanes [74], [75], [91], [92], iso- and cyclo-alkanes [1], [78], [80], [92] and some BTEX compounds [76] under temperature-fixed environments can sustain microbial growth and methane biogenesis [27]. Now, different OSTPs, including the Mildred Lake Settle Basin (MLSB), are continuously storing diluents, resulting in a constant organic material supply to support methane production over the years [35],

[37]. Methane emissions are also present in EPL, such as at the Base Mine Lake (BML). The particular reason for methane emissions in BML is because mature fine tailings, which presumably contained active methanogens, were transferred from MLSB to the BML between 1995 and 2012 [27]. Although OSTPs and EPL technologies may share common FFT material, they differ in other features, such as temperature gradient profiles [30], [77], [94]. Then, it is crucial to incorporate OSTPs and EPLs features, such as temperature gradients, into mathematical models for *in-situ* accurate predictions.

Current mathematical models, such as a phenomenological zero- and first-order kinetic model and a second-generation stoichiometric model, accurately predict methane production from FFT samples under fixed-temperature laboratory settings [47], [77]. These models could be extended and resourceful for in-situ predictions and future estimations. However, the justification of phenomenological models, based on basic principles relatable to more complex processes without proper mechanisms, is required to validate their meaningful predictions. Also, microbial-biomass-based stoichiometric models may increase prediction potentials by incorporating limiting factors, such as nitrogen bioavailability for microbes growth, with the trade-off of simulating microbial biomass dynamics [47]. Therefore, a data-validated mechanistic mathematical model is essential to support phenomenological models and overcome the infeasible track of biomass data. Furthermore, current models have been developed and tested under laboratory circumstances with temperature-fixed experiments, and including temperature variation may be crucial for methane predictions in OSTPs and EPLs.

In this work we investigate how temperature variations contribute to hydrocarbon degradation kinetics in OSTPs and EPLs through a new mechanistic and data-validated model. For this, we set up laboratory experiments to measure methane production and hydrocarbon kinetics commonly found in FFT under 5°C, 20°C, and 30°C. Such temperatures were selected to reproduce a broad spectrum of hydrocarbon (HC) temperature-dependent biodegradation rates. However, since our 5°C experiment is ongoing, we incorporated 10°C experiments from the literature into our data set for our model. Our mechanistic model encompasses known biological methane formation path flows, in which a DNA analysis determines the microbial communities and weight

of such path flows during methane generation. We compared our proposed mechanistic model predictions against the outputs of phenomenological models and verified the accuracy of simpler models. This way, we provide a solid basis for using more straightforward tools, which could be resourceful for rapid in-situ methane prediction scenarios. Finally, we investigated how our model predictions differ from governmental reported data containing diluent loss and methane emissions from different oil sands industries.

4.2 Material and methods

This section describes the laboratory experiment used to measure different temperature-dependent hydrocarbon degradation rates. We divided our experiment into three hydrocarbon groups, each containing a sample of short-chain n-alkanes, BTEX, and isoalkanes that served as carbon sources. Triplicates of each group were initially incubated at 5°C, 20°C, and 30°C to determine temperature effects on hydrocarbon degradation. Over 800 days, we collected data from microcosm headspace samples, and the original data remains confidential until published.

4.2.1 Fluid fine tailings source

Fluid fine tailings were collected in bulk in September 2019 from the Swan Base Mine Lake 12 (Platform 2) at a depth of 10.9 metres below the surface and stored in air-tight pails in the dark at a temperature of 4°C. After removal from the refrigerator, samples were immediately used in the culture setup in 158 mL sealed serum bottles.

4.2.2 Experiment set up

The anaerobic microcosms were prepared using 50 mL each of methanogenic medium and FFT in 158-mL serum bottles with a headspace of 30% CO₂ balance N₂ as previously described [75]. The methanogenic medium contained inorganic salts (NaCl, CaCl, NH₄Cl, MgCl₂, (NH₄)₆Mo₇O₂₄, ZnSO₄, H₃BO₃, FeCl₂, CoCl₂, MnCl₂, NiCl₂, AlK(SO₄)₂, NaHCO₃), vitamins (pyridoxine, thiamine, nicotinic acid, pantothenic

acid, cyanocobalamin, p-aminobenzoic acid), sodium sulfide (reducing agent) and resazurin (redox indicator) as described by [25]. The microcosms were pre-incubated at room temperature in the dark for two weeks for microbial acclimation and consumption of residual hydrocarbons and any alternative electron acceptors in MFT [75]. Prior to amending the microcosms with selected hydrocarbons, the headspace of all microcosms was flushed with 30% CO₂ balance N₂ to remove any CH₄ produced during pre-incubation. Each treatment was prepared in triplicate with different microcosm groups. Three different groups of hydrocarbons were used as a source of carbon: short-chain n-alkane (pentane, C₅; hexane, C₆; heptane, C₇; octane, C₈; decane, C₁₀), monoaromatic BTEX compounds (benzene, toluene, ethylbenzene, m,p-xylene, and o-xylene), iso-alkanes (2-methylpentane, 2-MC₅; 2-methylhexane, 2-MC₆; 3-methylhexane, 3-MC₆; 2-methylheptane, 2-MC₇; 4-methylheptane, 4MC₇; 2-methylnonane, 2-MC₉). As the internal standards for quantification of hydrocarbon degradation we used 1,1,3-trimethylcyclohexane (CAS#3073-66-3; ChemSampCo, Inc.). Triplicate abiotic controls (heat-killed microcosm) were prepared in parallel by autoclaving (121 °C, 20 psi, 60 min) for four consecutive days before hydrocarbon amendment to account for abiotic degradation. Triplicate baseline controls (unamended microcosms) were also prepared to account for CH₄ production from any residual endogenous substrates in the FFT. Immediately after the amendment, samples were collected from all the microcosms to determine FFT's initial (day 0) status for hydrocarbons and microbial community structure. The microcosms were incubated statically in the dark at room temperature, and headspace analysis was performed periodically (bi-weekly) to monitor CH₄ production and hydrocarbon degradation (monthly) in the microcosms. Culture samples were also taken periodically from the microcosms for microbial community characterization.

4.2.3 Analytical measurements

Methane was measured by taking out 0.1 mL headspace with an insulin syringe (28g, 0.5 mL) and injecting it into a gas chromatograph equipped with a flame ionization detector (GC-FID; Thermo Fisher Scientific, Trace 1300) with TG-Bond Q capillary column (30m, 0.32mm). Analyses were performed at an oven temperature of 40°C using He as

a carrier gas with a 40 mL/min flow rate. Percentages of methane in the headspace were calculated using external standards and then converted to molar basis using the Gas Law equation: $pV = nRT$. All microcosms were monitored for labile hydrocarbons and 1,1,3-trimethylcyclohexane (internal standard) by direct manual injection of 100 μ L of headspace using a gas chromatograph equipped with a mass spectrometer (GC-MS, Thermo Fisher Scientific, Trace 1300 - ISQ). Hydrocarbon concentration in the headspace was obtained by calculating the peak ratio of HC/internal standards from each measurement and comparing it with the ratio of Day 0 (establishing date), which was considered as 100%.

4.2.4 Microbial analyses

The microbial community structure was studied by sequencing 16S rRNA genes. One mL sample from each microcosm was taken with a 1 mL sterile syringe at the specific time point. Samples were stored at -20°C before DNA extraction. Total genomic DNA in the sample was extracted using the Fast DNA SPIN Kit for Soil (MP Biomedicals, USA). The extracted DNA was quantified using a Qubit 4 model fluorometer (Thermo Fisher, USA) immediately after extraction and was stored at -20°C before subsequent analyses. Extracted DNA samples were sent to the Molecular Biology Facility at the University of Alberta (MBSU). The V3-V4 variable regions of the 16S rRNA gene were amplified via PCR using universal primers 926Fi5 (5'- AAA CTY AAA KGA ATW GRC GG -3') and 1392Ri7 (5'- AC GGG CGG TGW GTR C -3') [3]. A second round of amplification was conducted using Illumina bridge PCR-compatible primers, followed by sequencing using the Illumina MiSeq platform (Illumina, San Diego, CA, USA). Quality-verified sequences were compared against the SILVA taxonomic database (version 3.0) using MetaAmp pipeline and clustered into Operational Taxonomic Units (OTUs) at ≤ 3

4.2.5 Laboratory results

After 800 days, samples under 5°C showed no methane biogenesis for all hydrocarbon groups; meanwhile, samples at higher temperatures showed active methane biogenesis

production.

For the n-alkanes group (see Fig. 4.1), we found that degradation of short n-alkanes at 30°C started before the 20°C experiment at the first amendment spike (400 ppm). However, hydrocarbon degradation rates at 30°C were visually lower than the hydrocarbons at 20°C. These results show that microbial activity is activated faster in warmer temperatures, slowly degrading short-chain n-alkanes and producing methane. At 20°C, the microbes required more adaptation time before starting to degrade hydrocarbons. However, their hydrocarbon degradation was faster once microbes started the biodegradation process. This effect dramatically changed after the second amendment spike, where we can observe that the lag phase disappears and the degradation kinetics rates are now similar.

We found no clear indications for BTEX degradation in the BTEX group (see Fig. 4.2). At 30°C, the first hydrocarbons to be biodegraded were Toluene and o-xylene at high rates, showing comparatively reduced lag phase among other results in this hydrocarbon group. After a second spike and additional exhausted hydrocarbons, we saw the same trend for such compounds with increased m,p-xylene decaying. A third spike of the biodegraded hydrocarbons, we could observe that Ethylbenzene also started to be biodegraded. Meanwhile, 20°C BTEX experiment showed a rapid decay of Toluene and o-xylene after 200 days. We also could observe a slow biodegradation of Ethylbenzene and a drastically high decay of m,p-xylene after 500 days. Experimentally, we could observe increased degradation rates for both treatments after a second spike, with a dramatically reduced lag phase. Furthermore, methane conversion efficiency was lower at 20°C than 30°C after the second spike.

We also found a significant difference in the iso-alkane group's methane biogenesis and hydrocarbon degradation kinetics. At 20°C, a very slow decaying of 2-MC5 and 3-MC6 over 700 days and a very slow degradation of 2-MC7 was appreciated. In comparison, the experiment at 30°C showed an increase in the biodegradation rate of the first 3 spiked compounds. After exhaustion, we spiked our samples again with the same hydrocarbons previously added, plus an additional 4-MC7 and 2-MC9. After the second spike, all compounds showed no lag phase and increased degradation rate. In

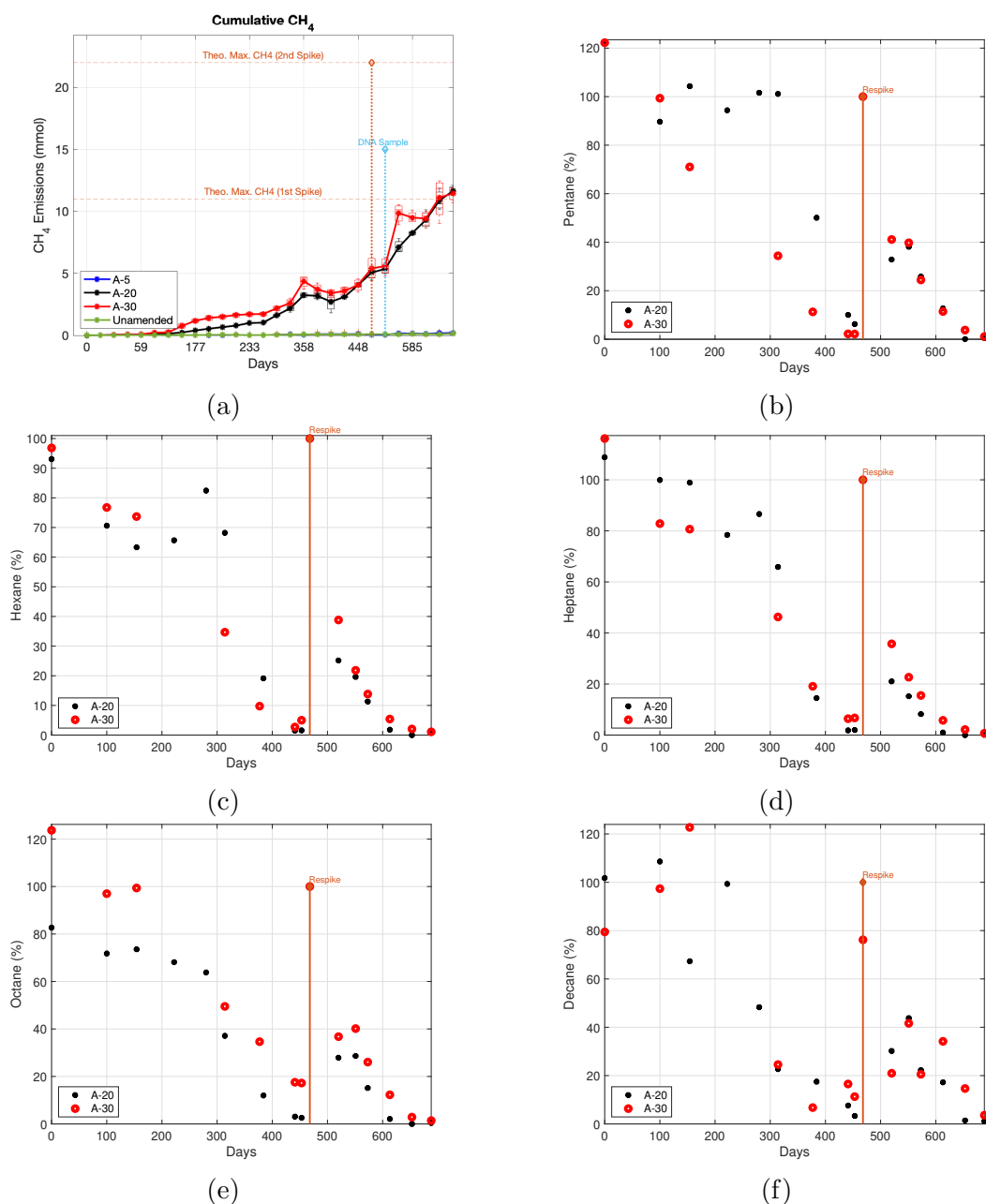


Figure 4.1: Experiment results for the short chain n-alkanes group. Red, black, blue and green colours distinguish experiment results between different temperature conditions. 5°C experiment is distinguished by the navy blue colour, black for 20°C, red for 30°C and green for the control experiment. The date of the DNA sample is shown in light blue. (a) Methane biogenesis derived from the biodegradation of short-chain n-alkane (pentane, C₅; hexane, C₆; heptane, C₇; octane, C₈; decane, C₁₀). The cumulative theoretical maximum for both spikes is shown in dotted orange lines, and dotted stems (vertical lines) represent hydrocarbon spikes. Solid lines show the mean CH₄ data trend. Panels (b) to (f) show the hydrocarbon degradation kinetics for each n-alkane compound. Simultaneous re-spikes for both temperature treatments are in orange.

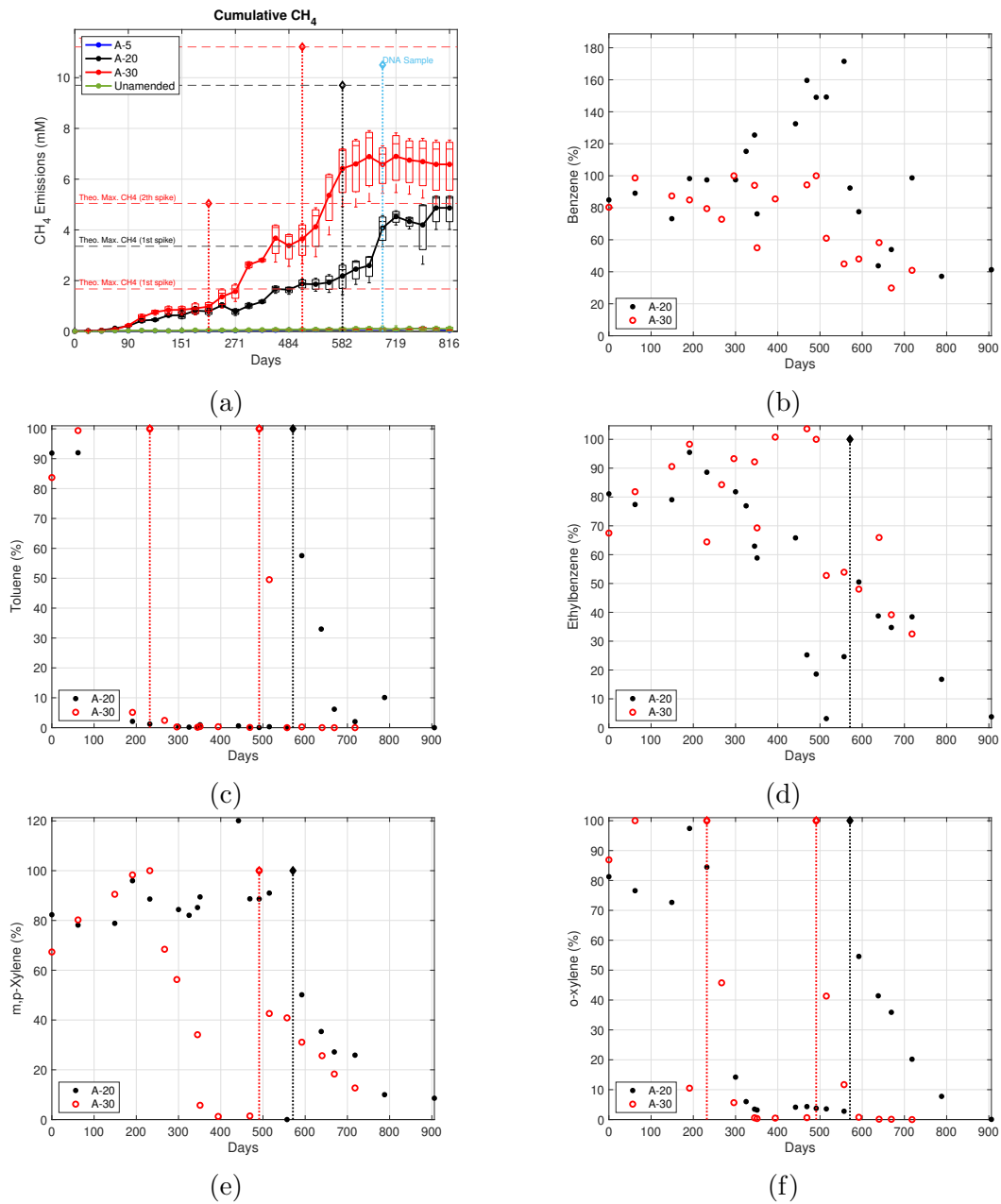


Figure 4.2: Experiment results for the BTEX group. See Fig. 4.1 caption for more figure details. (a) Methane biogenesis derived Ethylbenzene, Toluene, mp-xylene and o-xylene biodegradation. The cumulative theoretical maximum for diverse spikes is in dashed black and red lines. Solid lines show the mean CH₄ data trend and dotted stems represent hydrocarbon spikes. Panels (b) to (f) show the hydrocarbon degradation kinetics for each chemical compound labelled on the y-axis. Stems show an event such as spiking or DNA sample.

[80], a greater conversion efficiency and decay for a mix of iso-alkanes was established. Therefore, these results suggest that a more diverse compound mixture may benefit methane biogenesis. Brief summaries of these results can be found in Fig. 4.7 and Fig. 4.8.

4.3 Mechanistic methane biogenesis model

Methane mitigation in oil sands territories requires assessed strategies based on accurate quantifications of methane biogenesis production due to the biodegradation of unrecovered diluents [75]. A zero- and first-kinetics phenomenological model and stoichiometric microbial-based nutrient-limited model may provide accurate methane and hydrocarbon estimations in temperature-fixed laboratory settings with the potential to be extended to in-situ greenhouse gas estimations [47], [77]. However, modelling limitations may arise due to the absence of, for example, methane biogenesis mechanisms for the phenomenological models or access to biomass measurements, which is usually unavailable. Biomass quantification results in a laboratory challenge since FFT contains different carbon sources, including bitumen and organic diluents [75]. In this section, we propose a mechanistic model that keeps track of the carbon flow from the microbial degradation of HC to the production of acetates, hydrogen (H_2), CO_2 and methane, which are potentially measurable variables.

4.3.1 Model development

Methane biogenesis in OSTP and EPL is derived from the microbial metabolism of residual diluents used during the bitumen separation from oil sands [27]. Previous studies have shown that a range of n-alkanes, BTEX and iso-alkanes support methane biogenesis, and the biodegradation of these HC compounds produces acetates, hydrogen and carbon dioxide, essential for methane biogenesis production in anaerobic conditions [33] [75] [27], [79], [80]. For this model, we consider the two known methane biogenesis pathways given by

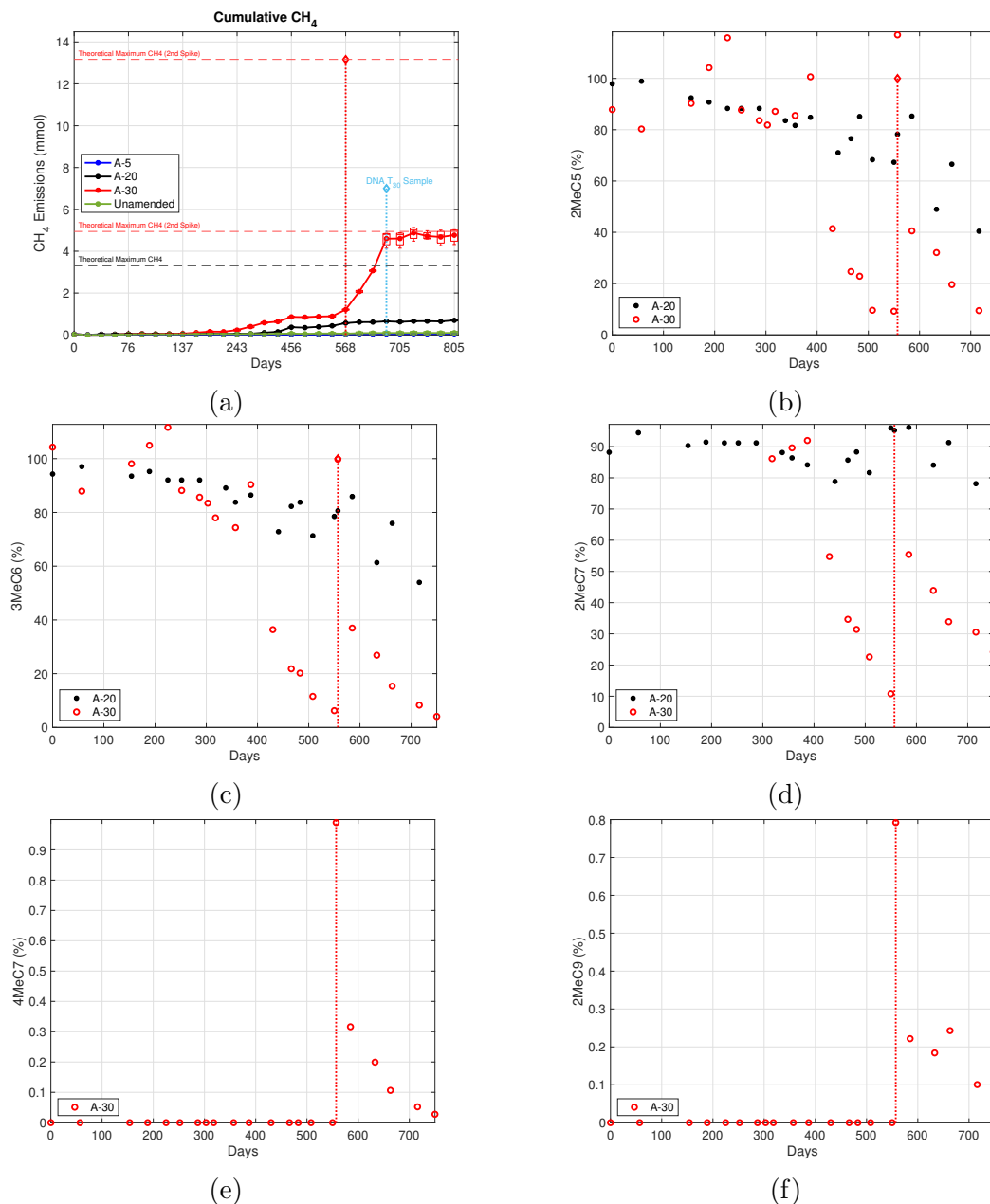
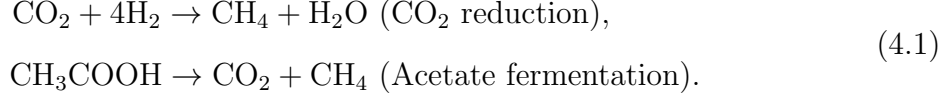


Figure 4.3: Experiment results for the iso-alkanes group. See Fig. 4.1 caption for more specific details. (a) Methane biogenesis derived from 2-MC5, 3-MC6, and 2M-C7 biodegradation for the first spike with additional 4-MC7 and 2-C9 for the second. The cumulative theoretical maximum for diverse spikes is orange (the first spike is in both treatments) and red. Solid lines show the mean CH₄ data trend. Panels (b) to (f) show the hydrocarbon degradation kinetics for each chemical compound labelled on the y-axis. Stems show an event such as spiking or DNA sample.



Nutrient limitation may play a fundamental role during methane biogenesis formation [47]. However, supported by a relatively consistent CH₄ production in flux chambers over large periods and no further microbial biomass augmentation of anaerobic enrichment cultures, we considered CH₄ methane biogenesis limitation only by hydrocarbon sources [77], [86]. Then, the hydrocarbon degradation rate of change is given by

$$C'_i = \underbrace{-k_{c_i}g(C_i)}_{\text{Hydrocarbon degradation}} + \underbrace{C_{in}^i}_{\text{Diluents input}}, \tag{4.2}$$

where k_{c_i} represents the i -th hydrocarbon degradation rate and $g(C_i) = 0$ for $0 \leq t \leq \lambda_i$, representing microbial required acclimatization lag period. Also, C_{in}^i is the specific i -th diluent input into the system and is considered a positive constant for OSTP ($i = 1$) or zero for EPL ($i = 0$) scenarios. Hydrocarbon biodegradation produces labile substrates, which we consider in terms of acetates. Then,

$$S' = r_1 \underbrace{\sum_{i=1}^n k_{c_i}g(C_i)}_{\text{Acetate production}} - \underbrace{r_2f(S)}_{\text{Acetate degradation}}, \tag{4.3}$$

where acetates (S) are produced proportionally to the hydrocarbon degradation rate ($r_1 \in [0, 1]$), which are further biodegraded to produce, CO₂ and CH₄ metabolites at a rate (r_2). In anaerobic conditions, hydrocarbon fermentation yields an increase of hydrogen in the system, which is microbially utilized along with CO₂ to produce methane, i.e.,

$$H' = \underbrace{h_c \sum_{i=1}^n k_{c_i}g(C_i)}_{\text{Hydrogen production}} - \underbrace{4r_3m(H, D)}_{\text{CO}_2 \text{ reduction}}, \tag{4.4}$$

where h_c is hydrogen productivity in anaerobic bacterial systems [42], and r_3 is

attained to the CO₂ reduction. Here, the function $m(H, D)$ is considered for mass action to simplify the equations. Now,

$$D' = \underbrace{(1 - r_1) \sum_{i=1}^n k_{c_i} g(C_i)}_{\text{CO}_2 \text{ production}} - \underbrace{r_3 m(H, D)}_{\text{CO}_2 \text{ reduction}} + \underbrace{(1 - r_4) r_2 f(S)}_{\text{Acetate fermentation}}, \quad (4.5)$$

represents the CO₂ rate of change during the hydrocarbon degradation and methane production. This pool increases during acetate fermentation and hydrocarbon degradation at $(1 - r_4)r_2$ and $(1 - r_1)k_{c_i}$ rates, respectively. The parameter $r_4 \in [0, 1]$ is the proportion of CH₄ produced from acetate degradation by acetoclastic methanogens. Finally, the two pathways to form methane lead us to,

$$G' = \underbrace{r_3 m(H, D) + r_4 r_2 f(S)}_{\text{Metabolites production}}, \quad (4.6)$$

where G represents the metabolite's increase rate before being utilized by hydrogenotrophic (CO₂ reduction path) and acetoclastic (acetate fermentation path) methanogens to produce CH₄. Note that our system is open, i.e. $(\sum C_i + S + H + D)' = h_c \sum k_{c_i} g(c_i) \geq 0$, which may increase the surplus of hydrogen in the system. Finally, we consider the methane production in terms of

$$\text{CH}_4^j(t) = \eta \overline{SF} G(t), \quad (4.7)$$

as proposed in [77] with $G(0) = 0$, where $0 \leq \eta \leq 1$ is the methane conversion efficiency. Since we are not explicitly measuring the stoichiometric fraction for each hydrocarbon degradation yield to methane production as in [47], [77], we use \overline{SF} as the mean stoichiometric fraction for degradable hydrocarbons. In this model, $\text{CH}_4^j(t)$ represents the methane biogenesis estimation in active OSTP ($j = 1$ and $C_{in}^i > 0$) or an EPL ($j = 0$ and $C_{in}^i = 0$). For simplicity, our mechanistic model considers functions $g(C) = C$ and $f(S) = S$. Therefore, the first-order mechanistic model (FOM - model) is given by,

$$\begin{aligned}
C'_i &= -k_{c_i}C_i + C_{in}^j, \\
S' &= r_1 \sum_{i=1}^n k_{c_i}C_i - r_2S, \\
H' &= h_c \sum_{i=1}^n k_{c_i}C_i - 4r_3HD, \\
D' &= (1 - r_1) \sum_{i=1}^n k_{c_i}C_i - r_3HD + (1 - r_4)r_2S, \\
G' &= r_3HD + r_4r_2S,
\end{aligned} \tag{4.8}$$

$$\text{CH}_4^j(t) = \eta \overline{SF} (G(t) - G(0)),$$

where the biodegradation of hydrocarbon-derived simpler compounds explicitly estimates methane biogenesis. Also, as part of the model features, we can differentiate the two methanogenesis strength paths depending on hydrogenotrophic and acetoclastic methanogens by modulating the free parameter r_4 , which DNA sequence samples can provide an accurate proportion.

4.3.2 Qualitative methane biogenesis predictors

To simplify model (4.8), if required, we assume that methane biogenesis can be determined only through acetate fermentation, i.e., $r_1, r_4 = 1$, and $r_3 = 0$ to avoid hydrogen and carbon dioxide kinetics tracking. For simplicity, we consider C as the sum of the total amount of hydrocarbons. Then, the reduced model is given by

$$\begin{aligned}
C' &= -k_cC + C_{in}^j \\
S' &= k_cC - \rho_2S \\
G' &= \rho_2S
\end{aligned} \tag{4.9}$$

$$\text{CH}_4^j(t) = \rho_2 \eta \overline{SF} (G(t) - G(0)),$$

where, ρ_2 is different parameter from (4.8). Considering the initial stage of hydrocarbon degradation i.e. $(C(0), S(0), G(0)) = (0, 0, 0)$, and a constant input of diluents $j = 1$,

we can solve (4.9) equations explicitly as follows,

$$C(t) = \frac{C_{in}^j}{k_c} (1 - e^{-k_c t}), \quad (4.10a)$$

$$S(t) = \frac{C_{in}}{\rho_2(k_c - \rho_2)} \left[k_c(1 - e^{-\rho_2 t}) - \rho_2(1 - e^{-k_c t}) \right], \quad (4.10b)$$

and,

$$G(t) = C_{in} t + \frac{C_{in}}{\rho_2 k_c (k_c - \rho_2)} \left[\rho_2^2 (1 - e^{-k_c t}) - k_c^2 (1 - e^{-\rho_2 t}) \right]. \quad (4.11)$$

Therefore, long-term methane biogenesis estimations can be expressed as

$$\text{CH}_4^1(t) \approx \eta \rho_2 \overline{SF} C_{in} \left(t - \frac{\rho_2 + k_c}{\rho_2 k_c} \right), \quad (4.12)$$

which is in the form of a zero-order kinetic model. This result highlights that in OSTP, where a constant efflux of diluents is considered, methane estimations could be linearly estimated for sufficiently large t .

For EPL scenarios, i.e., $j = 0$, and $(C(0), S(0), G(0)) = (C_0, S_0, 0)$ where $C_0, S_0 > 0$, we have the following simplified model:

$$\begin{aligned} C' &= -k_c C, \\ S' &= k_c C - \rho_2 S, \\ G' &= \rho_2 S, \end{aligned} \quad (4.13)$$

$$\text{CH}_4^0(t) = \rho_2 \eta \overline{SF} G(t).$$

Solving the system above, we have that

$$\begin{aligned} C(t) &= C_0 e^{-k_c t}, \\ S(t) &= \frac{1}{\rho_2 - k_c} \left[C_0 k_c (e^{-\rho_2 t} + e^{-k_c t}) + S_0 e^{-\rho_2 t} (\rho_2 - k_c) \right], \end{aligned} \quad (4.14)$$

and,

$$G(t) = \frac{C_0}{k_c - \rho_2} \left[k_c (1 - e^{-\rho_2 t}) - \rho_2 (1 - e^{-k_c t}) \right] + S_0 (1 - e^{-\rho_2 t}), \quad (4.15)$$

where,

Therefore, the cumulative methane biogenesis produced in an EPL may be estimated as $t \rightarrow \infty$, or

$$\text{CH}_4^0 \rightarrow \rho_2 \eta \overline{SF} (C_0 + S_0). \quad (4.16)$$

4.4 Model validation

The model (4.8) considers hydrocarbon kinetics under a fixed temperature. Some parameters may generally be temperature dependent ($^{\circ}\text{C}$), which can be determined using diluent biodegradation experiments under different temperatures. Our data set was supplemented with two extra sets extracted from the literature, enabling extended numerical results by considering other biodegradable hydrocarbons commonly present in oil sands activities at 10°C and 20°C . To estimate the required parameters and validate model (4.8), we data-fitted hydrocarbon dynamics and compared CH_4 predictions with the methane measurements. We used two numerical error estimators to quantify the dispersal of our predictions of estimated methane production under different temperature settings.

4.4.1 Data-fitting and parameter estimation

Since our experiments for 5°C (n-alkanes, BTEX, and iso-alkanes) did not show any activity for more than 800 days, and we only achieved partial degradation of iso-alkanes at 20°C , we incorporated the following data found in the literature which contains iso-alkanes degradation at 20°C (3-MC6, 2-MC7, 4-MC7 and 2-MC8) and methane production from amended FFT collected at 31m from the Mildred Lake Settle Basin [80], and only methane emissions from the degradation of a hydrocarbon mixture (n-decane, n-octane, toluene, o-xylene, 3-MC6, 2-MC5) in FFT collected from BML at 10°C [48].

To estimate model (4.8) parameters regarding each temperature experiment setting, we divided the data set into subsets according to each hydrocarbon group (n-alkanes, BTEX, iso-alkanes) and the temperature-related degradation kinetics (10°C , 20°C and 30°C). Then, we subdivided each subset into data subsamples according to the number of microcosm spikes, i.e., adding more hydrocarbons. This subsample set contains each hydrocarbon degradation kinetics group at different temperatures according to the number of hydrocarbon spikes (T_{τ}^s), where τ is the temperature ($^{\circ}\text{C}$) and s represents the spike ($s \in [1, 2, 3]$). For example, if we are working on the n-alkanes subset, and we want to fit our model to the subsample T_{30}^2 , this would mean that we will be using

the n-alkanes data at 30°C after the second spike. The model parameters calculation corresponds to each subdivided data plus the additional two data sets in the literature.

Each spike mathematically represents a dramatic change rate in our dynamical system (4.8). Therefore, we simplified our data fitting by using each data subsample separately and gluing numerical solutions. However, a mismatch in the initial conditions for each subsample arises after the first spike. We used $(C_i^1(0), S^1(0), H^1(0), D^1(0), G^1(0)) = (c_i^1, 0, 0, 0, 0)$ as the initial condition for each first subsample, where c_i^1 represents each initial hydrocarbon value at the first spike. Once the model was fitted for the first spike subsample, we used the end of this simulation as the initial condition for the contiguous subsample, which contains the second spike (and so on), i.e. $(C_i^2(0), S^2(0), H^2(0), D^2(0), G^2(0)) = (c_i^2 + C_i^1(end), S^1(end), H^1(end), D^1(end), 0)$, where c_i^2 is the HC concentration for the second spike and *end* is the last simulation point of the first spike subsample (related to MATLAB notation). We assumed that the metabolites used for methane production for the first spike were independent of those generated in the second spike. The rationale behind this assumption is that after adding new hydrocarbon sources, microbes will require some time to produce new metabolites, contributing to further methane production. The cumulative CH₄ biogenesis was calculated for the first metabolite leftovers pool until exhaustion to compensate for the mismatch between metabolites between spikes, adding it to the second methane subsample pool. All parameters were estimated for each subsample, except for the hydrogen productivity ($h_c = 2.2$) [42], the mean stoichiometric fraction (\overline{SF}) and conversion efficiency (η) (see Fig. 4.8), since we computed them directly given that biodegradable hydrocarbons and the theoretical CH₄ maximum are known.

Using the hydrocarbon subsample points, a nonlinear regression function in MATLAB (*nlinfit*), and the Normalized Mean Square Error (NMSE) defined as

$$\text{NMSE} = 1 - \frac{\|x_0 - x_1\|^2}{\|x_0 - \overline{x_0}\|^2}, \quad (4.17)$$

where $\|\cdot\|$ is the Euclidean norm, we estimated the model parameters and quantified our fitting accuracy. In the above equation, x_0 contains laboratory data, x_1 the predictions from the model as vectors and $\overline{x_0}$ is the mean of the laboratory data points. The function NMSE returns a value between $(-\infty, 1]$, where if NMSE= 1, then a perfect

fit is obtained. The NMSE summary we obtained from our subsample data fitting is represented in Fig. 4.4.

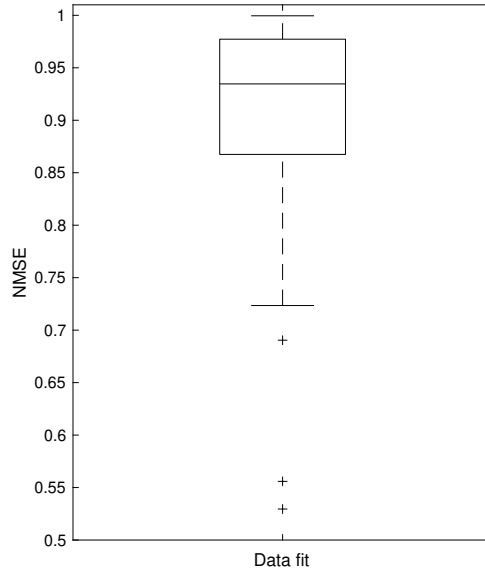


Figure 4.4: Normalized Mean Square Error (NMSE) summary from subsample data set fitting. The distribution of the NMSE calculated contains degradation kinetics accuracy of n-pentane (C_5), n-hexane (C_6), n-octane (C_8), n-decane (C_{10}), toluene, ethylbenzene, xylene isomers, 2-MC5, 3-MC6, 2-MC7, 4-MC7, 2-MC8, and 4-MC9 at different temperature (20°C and 30°C) and spikes. The NMSE quantifies the model accuracy from $(\infty, 1]$, where if $\text{NMSE} = 1$, then a perfect fit is achieved. The median NMSE value achieved is ≈ 0.9 . The three different outliers belong to $\text{NMSE}(C_7(T_{20}^1)) = 0.52$, $\text{NMSE}(2\text{-MC}_5(T_{20}^1)) = 0.55$ and $\text{NMSE}(2\text{-MC}_5(T_{30}^2)) = 0.69$.

We achieved an NMSE median value of $\approx .9$ from those subsamples that contained HC degradation kinetics, and the interquartile range was estimated between $[.86, .97]$. However, NMSE calculations showed three outliers that belong to the hydrocarbon fitting for the $C_7(T_{20}^1)$, $2\text{-MC}_5(T_{20}^1)$, $2\text{-MC}_5(T_{30}^2)$ with $\text{RMSE} = 0.52$, 0.55 and 0.59 respectively (see Fig 4.7). Still, a good accordance on the degradation kinetics trends for our simulations holds.

Once the model (4.8) was fitted regarding HC kinetics, we visually inspect the accordance between hydrocarbon degradation and methane biogenesis predictions against data in Fig 4.5, 4.6a and 4.6c. In these figures, we plot the sum of hydrocarbon predictions (we model HC kinetics for the 10°C experiment (see Fig 4.6d)) and laboratory data to represent the hydrocarbon kinetics in a simplified visual way instead of show-

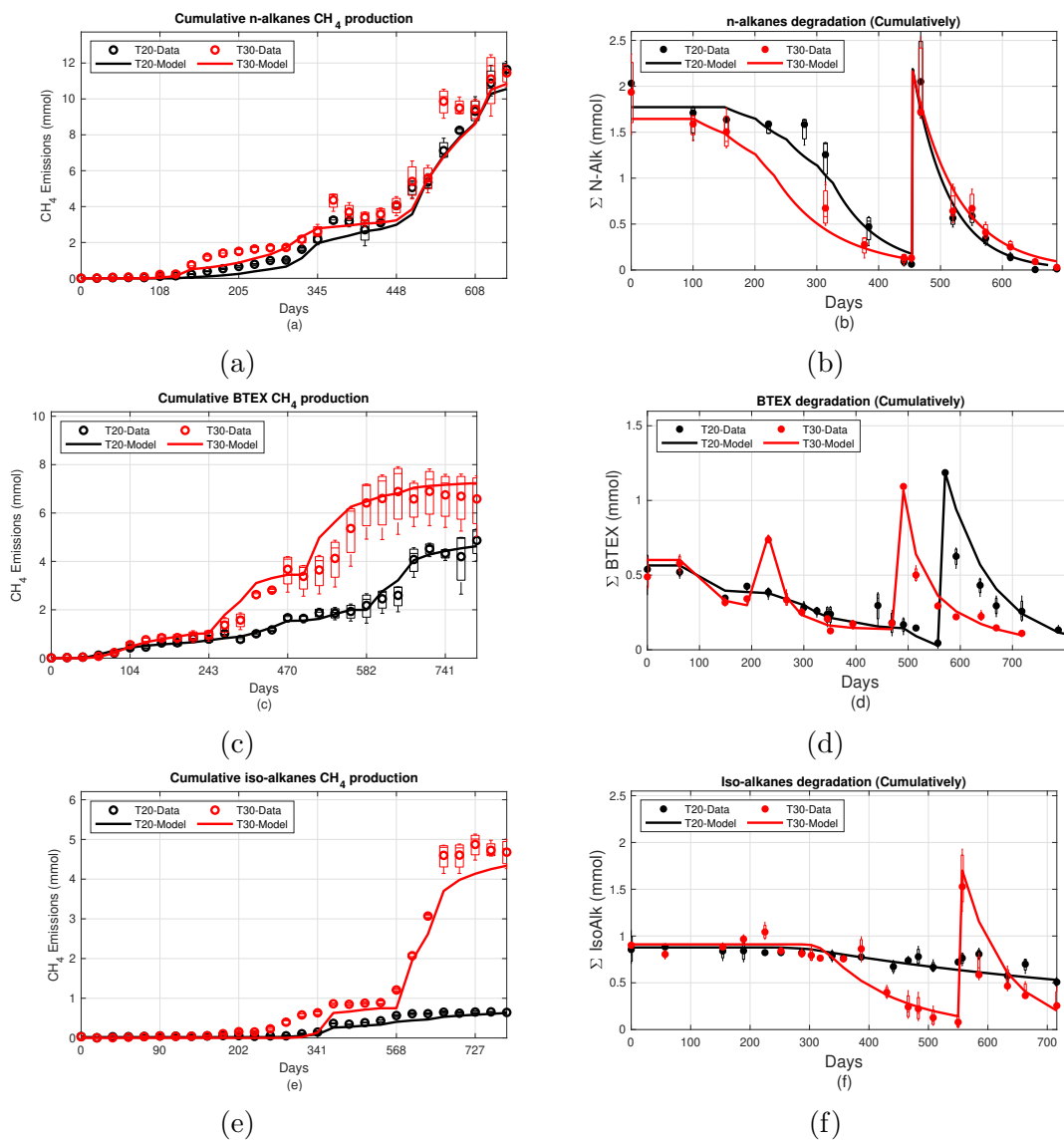


Figure 4.5: Model (4.8) methane predictions against laboratory data (first column) and the sum of hydrocarbon data fitting results (second column) against hydrocarbon degradation experiments at 20°C (30°C) coloured in black (red). For simplified visual purposes, the sum of all hydrocarbon data points is shown and compared with model fitting. Panels (a) and (b) show the cumulative CH_4 prediction compared to data and the cumulative n-pentane (C_5), n-hexane (C_6), n-heptane (C_7), n-octane (C_8) and n-decane (C_{10}) degradation fitting. Panels (c) and (d) show the results obtained for toluene, ethylbenzene, and xylene isomers experiments. Panels (e) and (f) for iso-alkanes experiments, composed of 2-MC5, and 2-MC7 for the first spike and an additional 4-MC7 and 2MC9 for the second spike for the 30°C experiment.

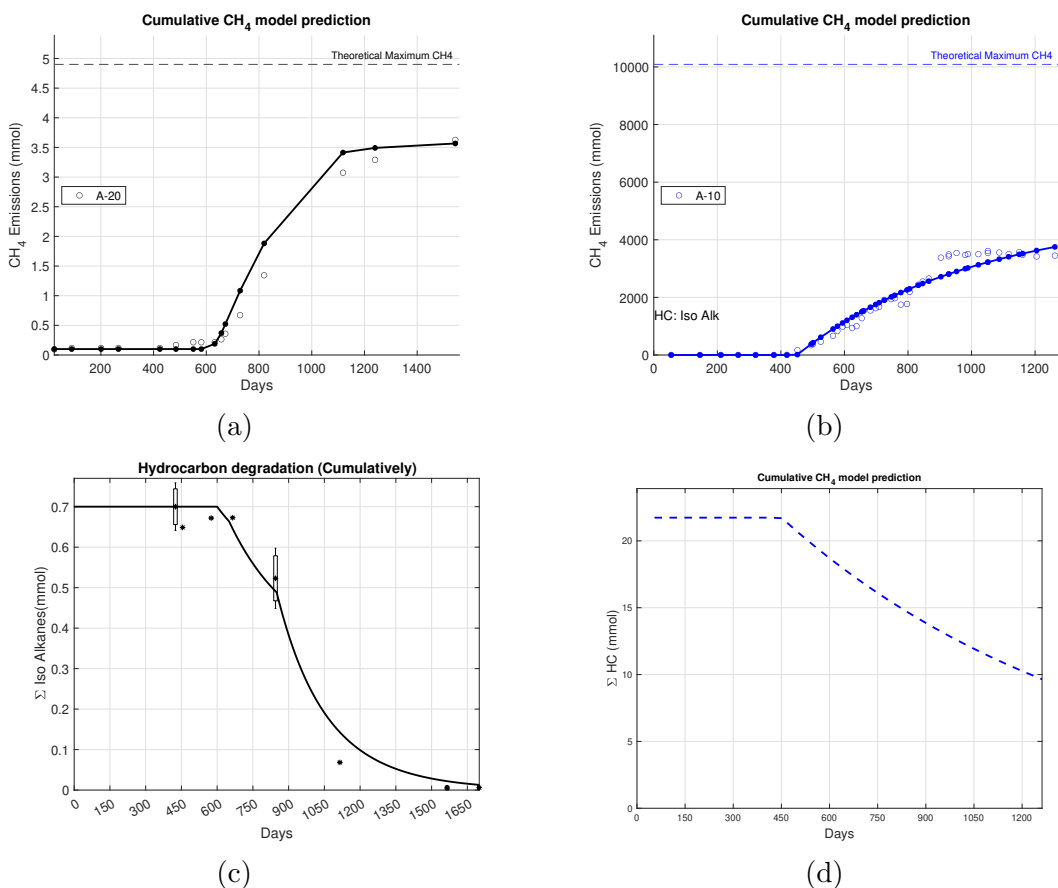


Figure 4.6: Model (4.8) predictions against laboratory data and CH₄ data fitting. Panels (a) and (c): methane prediction against laboratory data and HC degradation sum model fitting at 20°C (3-MC6, 2-MC7, 4-MC7, 2-MC8) (data adapted from [80]). We added all hydrocarbon data points and model fittings for visual purposes. Panels (b) and (d): CH₄ data fitting and sum HC degradation modelling (n-decane, n-octane, toluene, o-xylene, 3-MC6, 2-MC5) (data adapted from [48])

ing the model fitting for each hydrocarbon. In general, we found a good agreement for the qualitative CH₄ and hydrocarbon degradation kinetics behaviour, and we can estimate qualitatively the disperse of observations against predictions using the root mean square (RMS) defined as,

$$\text{RMS} = \frac{1}{\sqrt{N}} \sqrt{\sum_i^N (y_1^j - y_0^j)^2}, \quad (4.18)$$

where y_k^j represents the mean methane data as a vector (predicted methane as a

vector) for $k = 0$ ($k = 1$) and j is the $j - th$ component. Lower RMS values represent less discrepancy between predictions and observations. We achieved RMS values that varied between $[0.073, 0.88]$, and the mean was 0.435. Our iso-alkanes experiment at 20°C attained the lowest RMS value and the highest for the n-alkanes experiment at 20°C. Note that in Fig. 4.5e the model showed a slight underestimation of CH₄ despite of preserving the qualitative trend after the second spike. A reason for this, is because model 4.8 considers the mean stoichiometric fraction.

Based on the good accordance between predictions and data, we estimated the 95% confidence parameters intervals using the MATLAB function (*nlparci*), which uses the residuals and the estimated covariance matrix from *nlinfit*. From Fig. 4.7, we found a slight increase in n-alkanes degradation rates after the second spike for 20°C and 30°C, achieving the maximum at the former. Toluene, ethylbenzene and xylenes isomers (TEX) degradation rates are found to be dispersed for all the spikes but remain in the same order despite the different spiking for T_{30}^s (170 ppm for $s = 1$ and 257 ppm for $s = \{2, 3\}$). Iso-Alkanes hydrocarbons degradation rate estimates on the T_{20}^1 subsample show high dispersion. However, this feature is derived from the two experiments we consider. The highest value corresponds to the adapted data from [80], composed of an experiment with different settings and several iso-alkanes that are not present in ours. The lowest degradation kinetics for Iso-Alkanes at 20°C corresponded to our experiment, in which hydrocarbons show a slow degradation rate. This result suggests a higher degradation rate when a diverse HC mixture is present in FFT, where the microbial communities are more active. The lowest HC degradation rate values coincide with the 10°C data subgroup adapted from [48], which contains a mixture of short n-decane, n-octane, toluene, o-xylene, 3MC6 and 2MC5.

The hydrocarbon degradation rate trends generally remained in the same order for 20°C and 30°C for n-alkanes, TEX and iso-alkanes at 30°C (second spike). This result suggests a maximum HC degradation rate around 20°C and 30°C, accompanied by an evident decay for lower temperatures. We also found that FFT microbiomes no longer require an adaptation stage after adapting to the environment, degrading newly added HC immediately, at least in relatively short periods of HC scarcity. Furthermore, HC's

increased rate for n-alkanes and TEX is related to increased CH_4 conversion efficiency after the second spike (see Fig. 4.8), though TEX second spike and third ($T_{30}^{\{2,3\}}$) spike had greater HC concentrations (from 170 ppm to 257 ppm). The dispersal of the conversion efficiency on the Iso-Alkanes subsample at 20°C was explained by considering two different experiments.

The rest of the estimated parameters for model (4.8) are shown in Fig. 4.9. We found that parameters r_2 and r_3 remained unchanged during our data-fitting, and its accurate estimations can be achieved if CO_2 , H_2 or acetates data is available. The parameter $0 \leq r_1 \leq 1$ determines the CO_2 flow generated from HC degradation, whereas $0 \leq r_4 \leq 1$ determines the weight of methane biogenesis through acetate fermentation. To estimate r_4 , we used the proportions between acetoclastic and hydrogenotrophic methanogens as a starting point based on our DNA analysis.

4.5 Numerical experiments

The first-order mechanistic model (4.8) was validated using laboratory experiment data sets, and its accuracy was measured in different error metrics. The required temperature-dependent parameters were determined using iso-alkanes, short n-alkanes, and TEX biodegradation experiments in FFT samples under different temperatures in section 4.4.1. Now, model outcomes might be helpful towards land reclamation strategies in oil sands territories, such as estimating CH_4 emissions in oil sands activities and anticipating cumulative methane in EPL over the years. We numerically explore predictive potentials between model (4.8), zero- and first-order kinetic models, as described in [77], enabling us a direct comparison between models and describe in which scenarios they might be helpful.

4.5.1 Predictions on measurable variables

Before comparing model (4.8) with the zero- and first-order kinetic models, we first show the simulated kinetic behaviour of acetates, CO_2 and hydrogen. These numerical predictions may provide insights into experimental designs like estimating data sampling scheduling. Data availability for CO_2 , H_2 and acetate kinetics would increase,

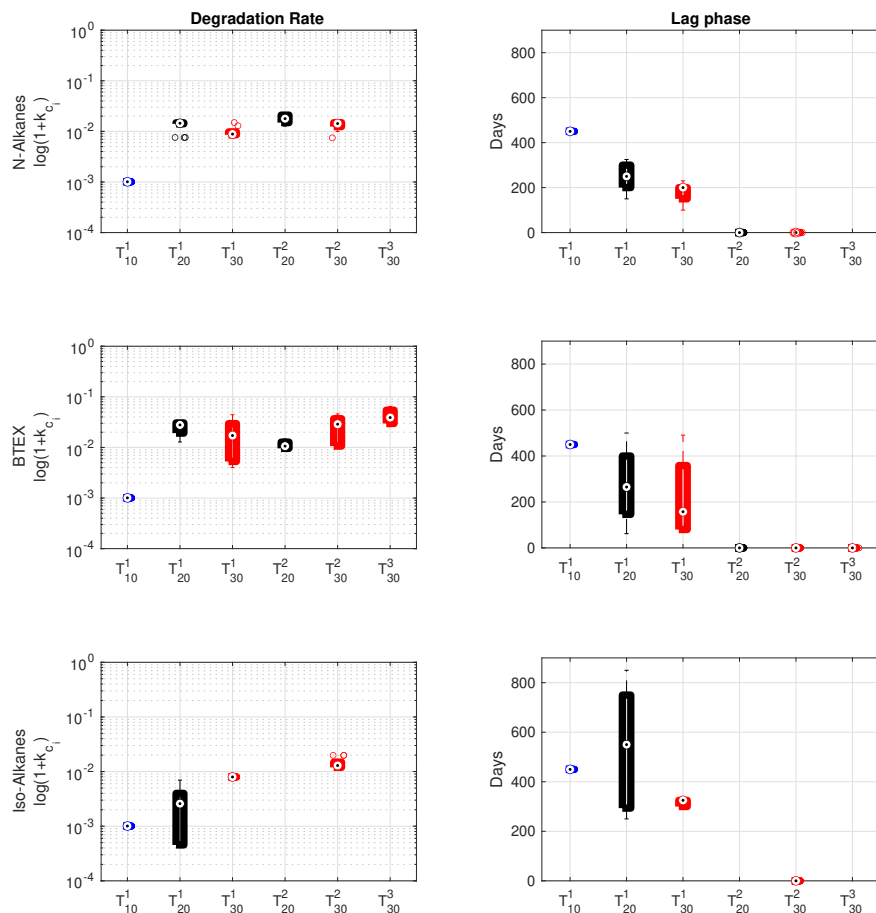


Figure 4.7: Degradation rate and lag phase estimation summary. The figure is divided into two columns, and each hydrocarbon group is arranged for each row, where the y-axis title in the first column determines the hydrocarbon group. Each column title indicates the estimated parameter. The x-axis for each panel represents the data subgroup (T_{τ}^s), where τ is the temperature ($^{\circ}\text{C}$) and $s \in \{1, 2, 3\}$ is the number of spikes in each experimental hydrocarbon group. The first panel's row shows the n-alkanes degradation kinetics and lag phase at different temperatures subject to each experimental spike. The second panel's row is for BTEX, and the third is for iso-alkanes. The degradation rate kinetics are expressed in a logarithm scale to improve its visualization, and box plots show the parameter dispersal, including outliers. The variation on T_{20}^1 experiments for iso-alkanes is derived by incorporating data from [80]

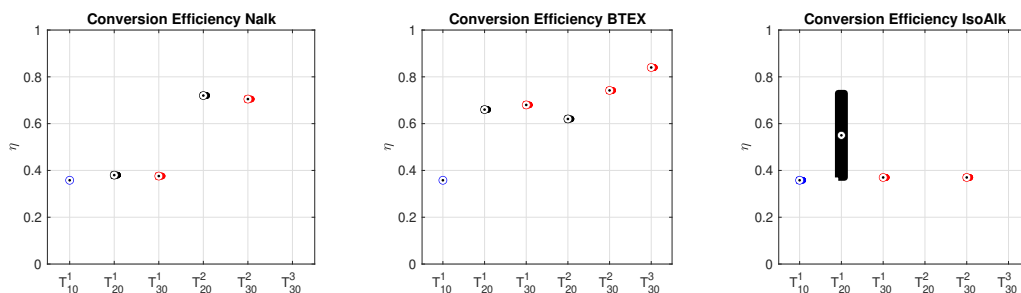


Figure 4.8: Conversion efficiency summary. Each panel title shows the calculated conversion efficiency for each HC group at different temperatures (τ) and spikes (s) T_{τ}^s . A boxplot for iso-alkanes conversion efficiency at 20°C was used to show the dispersed estimations and average related to two separated experiments for the first spike. The lowest value was attained in our experiment, and the highest was calculated from data adapted in [80].

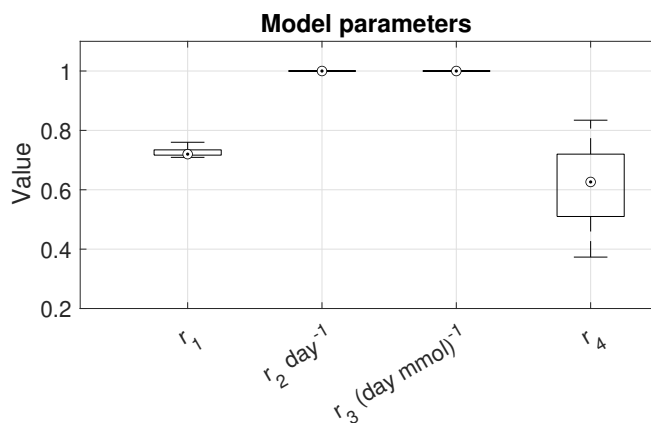


Figure 4.9: Model parameter estimation summary. The parameter $0 \leq r_1 \leq 1$ determines CO₂ flow from HC degradation, whereas $0 \leq r_4 \leq 1$ determines acetoclastic methanogen weight during CH₄ production. The acetates degradation (CO₂ reduction) rate is measured by r_2 (r_3). More accurate values for parameters r_2 and r_3 require measuring CO₂, acetates and/or hydrogen during HC degradation. Parameter dispersion for r_4 proportionally represents acetoclastic methanogens based on the DNA analysis.

although HC biodegradation kinetics and CH₄ emissions are well captured. In Fig. 4.10, we plotted the unmeasured variables predicted by the model (4.8) that play a crucial role in the two pathways for methane biogenesis.

Our numerical results predict increments on CO₂ and acetates that are qualitatively similar but in different magnitudes for the 20°C experiments. These increments correspond to when the bacteria start to decompose specific HCs. For example, in Fig. 4.10b, each sudden increase on CO₂ and acetates corresponds to start of C₇, C₁₀, C₈, C₆ and C₅ degradation in that order. One of the main differences between 20°C and 30°C numerical experiments showed that 20°C would have greater CO₂ production (for n-alkanes and BTEX), in which DNA analysis shows acetoclastic and hydrogenotrophic methanogens were proportionally close, about 45% to 55% each. Meanwhile, in the 30°C experiments, where acetoclastic methanogens were more abundant (up to 70% in the BTEX experiment), we see a decrease in CO₂ magnitude. These numerical predictions for unmeasured variables during our experiment still need to be validated. However, the hydrocarbon degradation kinetics and methane emission are well-captured.

4.5.2 Zero- and first-order kinetic model predictions revisited

Simple phenomenological models might provide useful rapid methane estimations if the prediction uncertainty or error is quantified. Using our data-validated mechanistic model, we compared the hydrocarbon degradation kinetics and methane biogenesis estimations with the zero- and first-order kinetic models. However, the zero-order kinetic model was previously adjusted, based on [77], to keep feasible positive solutions. The solution for the modified zero-order kinetic model is given by:

$$C_i(t) = \begin{cases} C_i(0)(1 - k_0^i t) & \text{if } t \leq (k_0^i)^{-1} \text{ and } t \geq \lambda_i, \\ 0 & \text{otherwise,} \end{cases} \quad (4.19)$$

and

$$\text{CH}_4(t) = \eta \sum_{i=1}^n SF_i (C_i(0) - C_i(t)), \quad (4.20)$$

for each number of biodegradable hydrocarbons i , where k_0^i is the zero-order i -th hydrocarbon degradation rate. In this way, we compared the hydrocarbon degradation

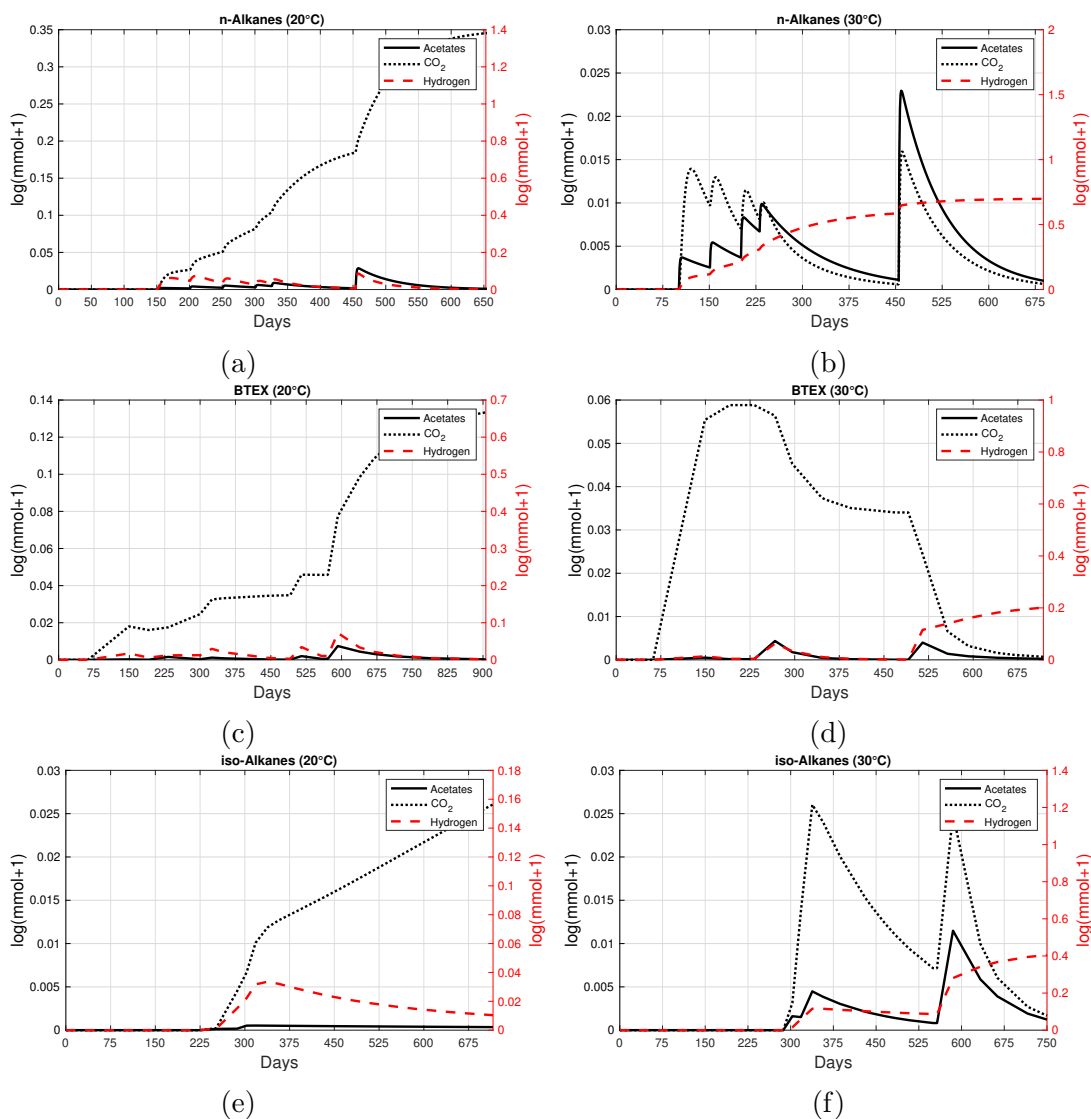


Figure 4.10: Model (4.8) predictions on acetates, CO₂, and hydrogen kinetics by degrading a group of short-chain n-alkanes, TEX, and some iso-alkanes at different temperatures during methane biogenesis. Panels (a), (c), and (e) represent predictions for distinctive HC group experiments at 20°C, whereas panels (b), (d), and (f) belong to experiments at 30 °C. The numerical predictions are shown in a logarithm scale for better visualization. Acetates and CO₂ scale are represented on the left axis, and hydrogen on the right for each panel.

rate given by the FOM and zero-order kinetic models and methane emissions RMS given by the phenomenological and FOM models (see Figure 4.11).

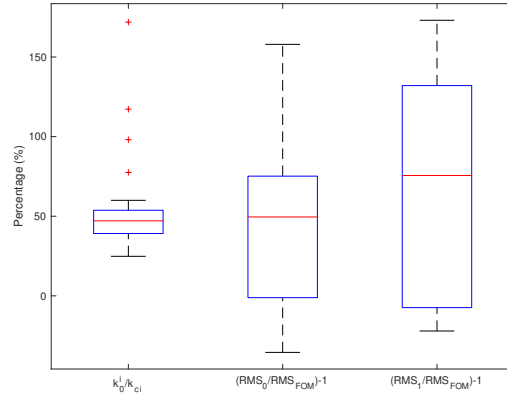


Figure 4.11: FOM and phenomenological models output comparison. k_0^i represents the zero-order hydrocarbon degradation rate. The RMS predictions for the FOM, zero- and first-order model are described as RMS_{FOM} , RMS_0 and RMS_1 , respectively.

In Figure 4.11, the zero-order kinetics rates (k_0^i) were computed individually for each hydrocarbon degradation time series at different temperatures and compared to those calculated by the FOM model. The RMS for the methane predictions using the zero- and first-order kinetic models (RMS_0 , RMS_1) are calculated and compared with the RMS methane predictions from FOM results. This figure shows that the degradation kinetic rate from the zero-order kinetic model is most likely to be half of the actual value. Furthermore, the FOM methane emissions predictions are generally better represented than the phenomenological model.

4.5.3 Methane biogenesis simulations in OSTP and EPL

According to the Mildred Lake 2019 Tailings Management Report (Synchrude Canada, April 30, 2020), the MLSB (an operating oil sands tailing pond) FFT temperature varies in depth between 6.9 - 15.7 °C (4m - 9m) and 18.4 - 20.8 °C (14m - 37m). In depths greater than 14m, the temperature is relatively constant due to a lack of mixing and thermal insulation [77]. However, the FFT temperature gradient in Base Mine Lake (end-pit lake located in Synchrude Mildred Lake facilities) varies temporally,

oscillating between approximately 5 °C and 25 °C relative to the depth (2.5m and 7.5m) [30], [94]. To compare the model’s performance in methane predictions between FOM, zero- and first-order kinetic models considering temperature features, we utilized MLSB reported diluents loss and methane emissions from 2016-2017 (data adapted from [47]) to simulate the OSTP ($C_{in}^1 \geq 0$), and assumed an immediate closure at the beginning of 2018 to simulate an EPL $C_{in}^0 = 0$ using the BML temperature fluctuations.

For our OSTP simulation, we fixed the pond temperature between 17 and 22°C, and for our EPL simulations, we interpolated the BML temperature variation at 2.5m depth over time using the 2014 data found in [94] as a representative temperature gradient using cubic splines and the MATLAB function (*spline*).

In Figure 4.12, we could observe a comparable performance of the zero- and first-order kinetic models with our mechanistic model that describes two path flows of CH₄ biogenesis. We separately computed the zero-order hydrocarbon kinetics median (see Table 4.1) since Figure 4.9 provides hydrocarbon kinetics information for the first-order and mechanistic models (see Table 4.2). Then, we fitted a quadratic polynomial or an exponential function, depending on the best parameter fit, to our data set with the highest achieved hydrocarbon kinetics median values, providing continuous temperature-dependent hydrocarbon kinetics for all models and hydrocarbon groups. Since negative kinetics are unfeasible, the quadratic polynomials were defined as zero instead of negative values during simulations. For our EPL scenario, we used cubic splines to simulate FFT temperature variations and evaluate the quadratic polynomial over time to get information about the degradation kinetics. The quadratic fit and polynomial evaluation were done using *fit* MATLAB 2024a function.

The different methane predictions for all models are consistently proportionally close to each other in the OSTP scenario, numerically validating the zero- and first-order methane biogenesis prediction potential using the first-order mechanistic model (4.8) (see Figure 4.12). All models consistently underestimated the cumulative methane reported from 2016 to 2017. In fact, for the year 2016 (2017), $46.84 \pm 7\%$ ($42.44 \pm 5\%$) was estimated by the zero-order model, $48.4 \pm 2\%$ ($48.19 \pm 2\%$) by the first-order and $45.63 \pm 2\%$ ($45.20 \pm 1\%$) by the FOM model for fixed temperatures that ranged from

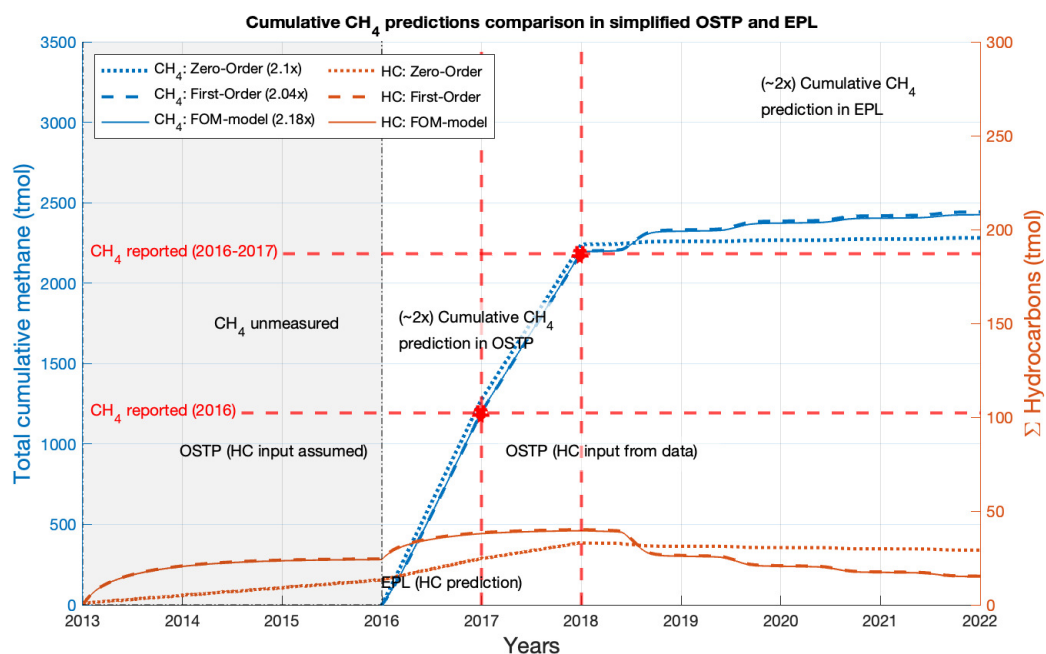


Figure 4.12: First-order mechanistic (FOM), zero- and first-order kinetic models comparison on the methane biogenesis estimation in MLSB for 2016-2017 and EPL simulation from 2018 to 2021. Methane biogenesis predictions are in blue, and HC kinetics are in brown. Dotted lines represent the zero-order kinetic model outputs, dashed lines for the first-order kinetic model and solid lines for the model (4.8). Diluent input from 2013-2015 is considered as the 60% of diluent loss reported during 2016 per assumed year, simulating a lower HC input over these years to reach a possible HC steady state. Methane was numerically unmeasured until 2016 to compare model cumulative CH_4 predictions to the reported in MLSB during 2016-2017 [47]. Red dashed lines represent reported cumulative methane. The zero-order kinetic model underestimates CH_4 reported by a factor of 2.1, 2.04 for the first-order kinetic model and 2.18 for the FOM model. After 2018, zero HC input was assumed to simulate an EPL scenario after OSTP closure. Methane emissions and HC degradation kinetics are predicted in four consecutive years of the simulation.

	K ₀ kinetics (median)			Fitting
HC group	T_{10}^1	T_{20}^2	T_{30}^2	$f(\tau)$
n-alkanes	2.3977E-05	0.003518	0.000486	$-3.2\text{E-}05\tau^2 + 0.0013\tau - 0.01$
TEX	2.3977E-05	0.00153	0.00242	$-7.5\text{E-}06\tau^2 + 0.00015\tau - 0.001$
iso-alkanes	2.3977E-05	0.00019759	0.00161635	$2.88\text{E-}06 \text{Exp}(0.21 \tau)$

Table 4.1: Zero-order HC kinetics table and function fit (Fitting). The rows below the K_0 kinetics (median) show median zero-order kinetics for different HC subsets T_τ^s , where τ is the temperature, and s is the number of HC spikes added. Zero-order HC kinetics for 10°C was estimated by modelling data adapted from [48] (see Fig.4.6). The last column contains the zero-order temperature-dependent functional representation.

	K ₁ kinetics (median)			Fitting
HC group	T_{10}^1	T_{20}^2	T_{30}^2	$f(\tau)$
n-alkanes	1.0001E-04	0.018	0.0142	$-1.\text{E-}04\tau^2 + 0.005\tau - 0.036$
TEX	1.0001E-04	0.0207	0.0387	$-7.95\text{E-}05\tau^2 - 0.0051\tau - 0.043$
iso-alkanes	1.0001E-04	0.0026	0.013	$1.84\text{E-}04\text{Exp}(0.141 \tau)$

Table 4.2: First-order HC kinetics table and function fit (Fitting). The rows below the K_1 kinetics (median) show median first-order kinetics for different HC subsets T_τ^s , where τ is the temperature, and s is the number of HC spikes added. First-order HC kinetics for 10°C was calculated as in Table 4.1.

17°C to 22°C. To produce these results, we assumed a constant HC input before 2016, estimating roughly the amount of degradable HC left after 2015 and the beginning of 2016. In this scenario, we simply assumed 60% of 2016 unrecovered diluents for each previous year, representing a smaller-scale diluent input in the MLSB. In Fig. 4.12, we show the methane biogenesis predictions during 2016-2017 for three years of assumed HC input loss from 2013 to 2015. Table 4.3 shows the percentage of predicted CH₄ for 2016 and 2017 for an n -assumed years previous to 2016, and further prediction improvements can be done if diluent mass and FFT loss rates are known.

It was found that zero-order methane estimations reached a fixed percentage of estimated methane before other models. This feature is due to zero-model linear HC decay at low HC concentrations, which rapidly increases methane estimations compared to first-order models, which show exponential HC decay and lower methane rate estimations. For this reason, zero- and first-order models estimate different HC kinetics when constant input of HC is assumed. These results show that zero- and first-order kinetic

MLSB Cumulative CH4 predictions in 2016 and 2017 at 21°C							
Period	HC input	Zero-order		First-order		FOM	
		2016	2017	2016	2017	2016	2017
2016-2017	0	48.40%	44.16%	40.05%	47.00%	38.09%	44.23%
2015-2017	1	48.87%	44.11%	47.34%	48.12%	44.73%	45.16%
2014-2017	2	48.68%	44.2%	48.56%	48.42%	45.77%	45.4%
2013-2017	3	48.86%	44.05%	48.90%	45.50%	46.02%	45.47%

Table 4.3: First-order mechanistic (FOM), zero- and first-order kinetic models cumulative methane predictions in MLSB during 2016-2017 using HC temperature-dependent kinetics and HC input assumption in previous years. The total methane reported from this period was 2182.1 t mol [47]. Each assumed year before 2016, assumes 60% of 2016 unrecovered diluent, simulating smaller-scale HC input. Methane predictions reach a fixed percentage of the cumulative methane reported by increasing the years of assumed HC input before 2016.

models can estimate in-situ methane emissions. However, Fig. 4.12 shows limitations of the zero-order-kinetics, whose estimations on HC storage in OSTP and EPL are different from the mechanistic and first-order kinetic model, including methane estimations in EPL settings. In our simulations, after 2018, the temperature variations drastically decreased hydrocarbon kinetics in colder weather and increased during warmer days. Our numerical experiment suggests that the hydrocarbon degradation rate and methane biogenesis decrease in EPL scenarios. In this simulation, the first-order kinetics estimate that it would take around 3.5 (5.5) years to degrade up to 80% (90%) of the total accumulated hydrocarbons estimation in 2018, with slight increments of cumulative methane over the years. Therefore, if EPL keeps producing methane after several years, then it is likely that methane biogenesis is supported by other organic sources that were not considered here.

4.5.4 Comparison between reported methane emissions and model predictions in Alberta’s oil sands territories.

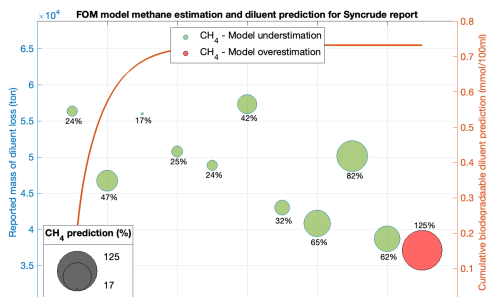
For this section, we utilized fugitive methane emissions datasets and unrecovered diluent reports from tailing ponds in Alberta oil sand mining regions. The sources of such data sets are available at (<https://open.alberta.ca/>) and (<https://www.aer.ca/>), which contain yearly reports on methane emissions and monthly reports of wasted dilu-

ent (ST-39) for different oil sands mining companies currently operating in Alberta. These reports correspond to different industry performances of cumulative methane emissions and diluent loss, in which individual oil sands tailing ponds monitoring is unavailable. To compare yearly methane emissions from the reports to those that the FOM model predicts for different companies, we assumed that unrecovered diluents are daily ditched into OSTP and immediately bioavailable for methane biogenesis, FFT's temperature is relatively constant, and hydrocarbon biodegradation is constantly active under methanogenic conditions. Also, we assumed that a fraction of the unrecovered diluents are volatilized and biodegraded by aerobic and sulphate-reducing bacteria. Therefore, for each company, only about 57% of unrecovered diluents are considered under methanogenic conditions [11], [47]. Our results are shown in Figure 4.13

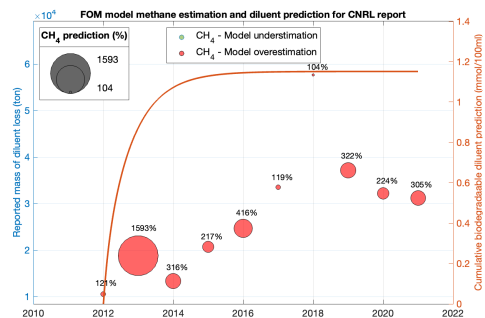
In Figure 4.13, we simulated the cumulative hydrocarbon degradation kinetics using the FOM model, assuming an evenly distributed yearly diluent loss as input of hydrocarbons into ponds day-to-day. For these results, we used a fixed temperature of 20°C and compared the methane emissions reports and predictions by the end of each year. In Figure 4.13a, our FOM model underestimates methane emissions reported from Syncrude from 2011 to 2020 and overestimates it in 2021. Also, in Figure 4.13d, our model underestimates methane emissions most of the years, but in many cases, we observed that the model relatively agrees with methane emissions reports. However, for Figures 4.13b and 4.13c, a significant discrepancy between model predictions and methane report is revealed. Our model overestimates methane emissions from CNRL and Shell companies each year, up to approximately 16 times the reported methane emissions. Also, the cumulative hydrocarbon kinetics for our simulations show that the accumulation of diluents reaches a steady state in the first years. This result suggests constant methane production in active oil sands tailing ponds if diluents are constantly replenished.

4.6 Discussion

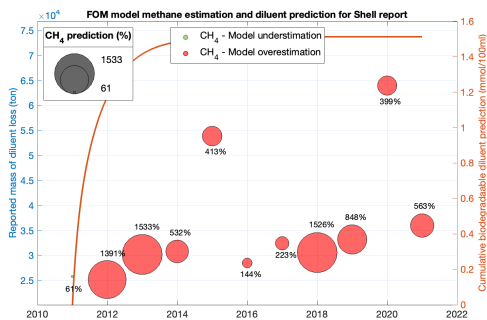
Methane contributes to 13% of GHG emissions in Canada, of which 40% comes from the oil and gas sectors (<https://www.canada.ca/>), and the Alberta government is ex-



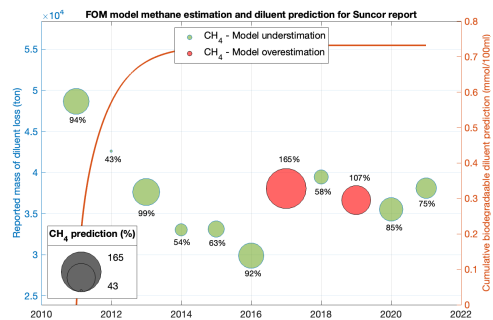
(a)



(b)



(c)



(d)

Figure 4.13: Yearly methane emissions comparison between FOM model predictions and Alberta Energy Regulator reports. Each panel represents methane emission comparison between different companies (a)-Syncrude, (b)-CNRL, (c)-Shell and (d)-Suncor reports against model predictions. Each bubble represents the ratio of methane FOM predictions and yearly reports for each company. The left axis represents the reported yearly diluent loss and localizes the center of each bubble. Green (red) bubbles represent an underestimation (overestimation) of methane predicted by the FOM model in percentage. The right axis represents the cumulative hydrocarbon kinetics over the years simulated by the FOM model.

amining produce legislation that would limit GHG emissions in oil sands territories by 2030 (<https://www.alberta.ca/climate-oilsands-emissions>). Methane emissions from oil sands wet tailings are primarily due to the biodegradation of unrecovered hydrocarbons stored in OSTP and end-pit lakes EPL [27], [35], [37]. These hydrocarbons are constituted partially from diluents used during the bitumen separation from oil sands [11], and the degradation of different compounds including n-alkanes [74], [75], [91], [92], BTEX [76], and iso-alkanes [1], [78], [80], [92], can support methane biogenesis [35], [37]. Creating accurate data-validated methane estimation mathematical models incorporating different OSTP and EPL features would be valuable for future tailing management and assessing current methane emissions industry performance.

To develop a temperature-dependent mechanistic data-validated model for methane emissions in OSPT and EPL, we investigated how temperature variations can contribute to the biodegradation of short-chain n-alkanes (C_5 , C_6 , C_7 , C_8 and C_{10}), BTEX, and iso-alkanes (2-MC5, 3-MC6, 2-MC7, 4-MC7 and 2-MC9), which are hydrocarbons found in OSTP and EPL that support methanogenesis, using FFT samples at 5°C, 20°C and 30°C. One principal objective of this experiment was to capture a broad temperature-dependent degradation kinetics spectrum. However, our 5°C experiments showed no methane activity after over 3 years, and data found in the literature with experiments running at 10°C and 20°C were used [48], [80]. Our findings for our 20°C and 30°C experiments show that the conversion efficiency from active samples may increase after adding more hydrocarbons to the samples after exhaustion. The degradation kinetics trends at these temperatures remained generally at the same scale. Also, the microbial lag phase is dramatically shortened once the microbes are adapted to degrade hydrocarbon sources. These results suggest a continuous diluent degradation with probably increased methane conversion efficiency for constantly added hydrocarbon supplies.

Current mathematical models, such as the zero- and first-order kinetic and second-generation stoichiometric models, accurately estimate methane emissions from HC degradation in laboratory settings. Their prediction potentials may be extended for in-situ methane estimations and hydrocarbon degradation [47], [77]. However, differ-

ent features still need to be included, such as the hydrocarbon temperature-dependent kinetics, mechanistic validation for the phenomenological models or incorporation of usually unavailable biomass kinetics [47]. To overcome these situations, we proposed a mechanistic model encompassing two methane biogenesis paths, allowing the recovery kinetics for measurable variables such as CO₂, acetates and hydrogen if required. Also, including these features in the mechanistic model allowed us to accurately predict methane emissions and degradation kinetics in laboratory settings, diversifying the methane path flow weights based on the microbial communities shown by DNA analysis.

Our data-validated model in laboratory settings provides a basis to extend the model predictions capacity and compare them to *in-field* reported methane emissions. Also, our mechanistic model provides a justifiable basis for using simpler phenomenological models, such as the zero- and first-order mechanistic models, in which their degree of prediction is evaluated. During our simulations, we compared our mechanistic model against diluents and methane emissions reported in [47] from MLSB during 2016 and 2017 by incorporating hydrocarbon temperature dependence. This approach reduced the still-wide gap between our model estimations and reality. According to our results, cumulative methane production linearly increases after hydrocarbons reach a saturation threshold, which is indirectly attributed to the FFT production rate, and simpler models, such as the zero- and first-order models, have the potential to estimate methane emissions *in situ*. Our methane predictions are about 7% lower than the second-generation stoichiometric model for methane biogenesis estimations [47]. However, to reach such estimations presented in [47], it would be necessary to deplete the yearly diluent loss at its totality according to stoichiometric mass-balance calculations. Our temperature-dependent model simulations reveal a surplus of diluents, stacking over the years of continuous oil sands mining. Furthermore, this accumulated surplus of elusive diluents would likely slowly degrade in EPL due to a temporal variation not present in OSTP. Temperature estimations in MLSB show they remain at a reasonably constant temperature (about 20°C) between 10-30 m depths [77], compared to a seasonal range from about 5°C to 20°C in BML between 2.5-7.5 m depths [30], [94].

Assessing methane emissions from oil sands industry activities, particularly in Alberta, is required to evaluate the performance of methane mitigation efforts. Using free data-available reports from Alberta oil sand mining regions through the Open Government Program and Alberta Energy Regulator websites, we compared the methane emission predicted from our mechanistic model with such reports. Our model predictions indicated a considerable overestimation of methane emissions compared to the reported from CNRL and Shell based on the amount of diluent loss per year. In contrast, our simulations show an underestimation of methane emissions from Syncrude reports in the last decade, except for the last year of reported data and relatively agreeable methane emissions from Suncor reports. The variation in the methane emissions estimations could be explained by the fact that OSTP and EPL in such companies' facilities are still inactive or FFT tailings are being treated differently to avoid diluents being degraded under methanogenic conditions. Compensating such discrepancies between methane predictions and methane reports will require continuous monitoring and increased data resolution from OSTP and EPL activities.

Modelling GHG emissions from oil sands tailing ponds and end-pit lakes is challenging and requires more than hydrocarbon kinetics and temperature features. For example, including different redox potentials into models to enable the possibility of microbes to form various chemical species, including H_2S , would provide a better understanding of in-situ biodegradation processes. Building holistic models would require large amounts of data collected directly from OSTP and EPL as a time series, which can increase costs and is probably unfeasible. Laboratory experiments provide a solid modelling background to anticipate in-situ methane release. Our mechanistic model allows accurate tracking of methane biogenesis, hydrocarbon degradation, and recover CO_2 , acetates, and hydrogen kinetics, if missing, under temperature-dependent features in exchange of stoichiometric calculations present in the second-generation stoichiometric model, where microbial biomass is not available. Under strict methanogenic conditions, the mechanistic model in this work also provides a basis for simple phenomenological models and quantifies their methane predictions and hydrocarbon degradation accuracy, which are easier to implement and can provide insightful information for rapid

in-situ methane biogenesis assessments. However, implementing new required features for GHG emissions, including the possibility of hydrocarbon degradation under different redox potentials, would require using a mechanistic models approach.

Chapter 5

Conclusion

5.1 Discussion of main results

The first component of this thesis was designated to create innovative tools for soil organic matter degradation processes under aerobic conditions. We have designed a stoichiometric model that could be used to understand how microbial communities utilize labile substrates rich in carbon and nitrogen. The data-validated priming effect model incorporates soil biodegradation processes by considering microbial and soil composition carbon-to-nitrogen ratios, and we extended this model to explore the symbiotic relationship between plants and microbes. Using different soil health indicators, such as SOM carbon-to-ratio content and soil infiltration, we could explore when plants must invest part of their resources into the rhizosphere to promote microbial growth and release SOM nutrients in exchange. Delimiting these scenarios could be helpful for soil management strategies, which can address better use of fertilizers.

The second component of this thesis focuses on methane production from oil sands territories, establishing the importance of incorporating temperature-dependent hydrocarbon degradation kinetics for in-situ predictions. We monitored the biodegradation of different groups of hydrocarbons, commonly used as diluents to separate bitumen from oil sands, in laboratory settings under three different temperatures. Our results point out that lower temperatures are not favourable for microbes to decompose unrecovered hydrocarbons that are stored continuously in OSTP or have been stored in EPL for years. In fact, after three years of monitoring, we didn't see methane pro-

duction in 5°C experiments, and through literature-found data, 10°C is cold enough to decrease substantially the hydrocarbon degradation rate. On the other hand, 20°C and 30°C showed increased degradation rates that remain in the same order, suggesting a plausible maximum close to such range.

A DNA analysis revealed that different microbial communities are present during the HC degradation, including hydrogenotrophic and acetoclastic methanogens. These groups of methanogens produce methane in two distinct paths, a feature we could incorporate into a new mechanistic model for estimating methane emissions in oil sands activities [27], [75]. Such a model was tested to verify its accuracy under laboratory settings and quantify the degradation kinetic rates observed through the experiments.

Once we quantified the variables and parameters, we tested our in-situ predictions considering temperature gradient profiles in OSTP and EPL. These predictions were compared against methane and diluent loss reports in MLSB from 2016 to 2017 [46]. Our numerical predictions highlight an accumulation of hydrocarbon over the years that is explicitly related to the unrecovered diluent rate. Also, given that OSTP temperature variation ranges between 17°C to 22°C [77], a constant methane emissions rate is observable, which can be reproduced by simpler models such as the zero-order kinetic model. However, the temperature may fluctuate between about 5°C to 22°C for EPL scenarios over the year [30]. This temperature variation slows down the HC degradation process in EPL in winter, and zero-order kinetic model HC estimations differ from the first-order.

Temperature variations in EPL will prolong the years microbes would take to deplete HC supplies. Our results show that, for known biodegradable HC, it would take about 10 years to degrade 90% of the HC stored in an EPL. In Chapter 4, we also showed that our mechanistic model is capable of recovering, to some degree, important measurable chemical species such as CO₂, acetates and H₂, which are part of the methane biogenesis progress.

The final remarks of this work show that phenomenological models, such as the zero- and first-order kinetic models, have the potential to predict methane emissions in situ, with the advantage of providing simple and accurate tools to stakeholders that

are rapidly required to evaluate methane emissions from oil sands activities.

5.2 Limitations and future work

Our data-validated model for SOM degradation processes is validated only through laboratory experiments, and calibration of the model by comparing it with in-field real data still has to be addressed. Our approach has been justified mathematically, providing a solid theoretical background to use such a model that potentially incorporates plant rhizodeposits and soil infiltration mechanisms. However, rhizosphere interactions between soil, plants and microbes represent an enormous challenge since several features that control rhizodeposits, microbial growth and activities, watering, pH, and mineral availability must be included. This can complicate the current model, and mathematical analysis would become more challenging for each new mechanism incorporated.

Regarding our mechanistic methane emissions model, we can highlight its possibility of including redox potentials, usually present in in-situ scenarios. Incorporating redox potentials into mechanistic models will allow us to estimate NO_x, H₂S, and other harmful gases in the long term. Our model provides a mechanism when anaerobic conditions are present, and incorporating new models for H₂S emissions will increase in-situ GHG estimations that would benefit tailing management and land reclamation scenarios. However, incorporating redox potentials into soil biodegradation processes will force the creation of holistic models, and several experiments should be done by researchers and soil experimentalists to validate and calibrate such models. Furthermore, in-situ methane estimations require monitoring services or tools that can provide substantial information for mathematical models and increase the accuracy of GHG estimations in the long term.

References

- [1] N. Abu Laban, A. Dao, K. Semple, and J. Foght, “Biodegradation of c 7 and c 8 iso-alkanes under methanogenic conditions,” *Environmental microbiology*, vol. 17, no. 12, pp. 4898–4915, 2015.
- [2] M. K. Alijani, H. Wang, and J. J. Elser, “Modeling the bacterial contribution to planktonic community respiration in the regulation of solar energy and nutrient availability,” *Ecological Complexity*, vol. 23, pp. 25–33, 2015.
- [3] D. An, S. M. Caffrey, J. Soh, *et al.*, “Metagenomics of hydrocarbon resource environments indicates aerobic taxa and genes to be unexpectedly common,” *Environmental science & technology*, vol. 47, no. 18, pp. 10 708–10 717, 2013.
- [4] F. Beeckman, H. Motte, and T. Beeckman, “Nitrification in agricultural soils: Impact, actors and mitigation,” *Current Opinion in Biotechnology*, vol. 50, pp. 166–173, 2018.
- [5] J. Bhatti and C. Tarnocai, “Influence of climate and land use change on carbon in agriculture, forest, and peatland ecosystems across canada,” *Soil carbon sequestration and the greenhouse effect*, vol. 57, pp. 47–70, 2009.
- [6] E. Blagodatskaya and Y. Kuzyakov, “Mechanisms of real and apparent priming effects and their dependence on soil microbial biomass and community structure: Critical review,” *Biology and Fertility of Soils*, vol. 45, no. 2, pp. 115–131, 2008.
- [7] E. Blagodatskaya, S. A. Blagodatsky, T.-H. Anderson, and Y. Kuzyakov, “Priming effects in chernozem induced by glucose and n in relation to microbial growth strategies,” *Applied Soil Ecology*, vol. 37, no. 1-2, pp. 95–105, 2007.
- [8] S. Blagodatsky, E. Blagodatskaya, T. Yuyukina, and Y. Kuzyakov, “Model of apparent and real priming effects: Linking microbial activity with soil organic matter decomposition,” *Soil biology and biochemistry*, vol. 42, no. 8, pp. 1275–1283, 2010.
- [9] A. W. Bowsher, S. Evans, L. K. Tiemann, and M. L. Friesen, “Effects of soil nitrogen availability on rhizodeposition in plants: A review,” *Plant soil*, vol. 423, pp. 59–85, 2018. DOI: <https://doi.org/10.1007/s11104-017-3497-1>.
- [10] M. C. Braakhekke, T. Wutzler, C. Beer, *et al.*, “Modeling the vertical soil organic matter profile using bayesian parameter estimation,” *Biogeosciences*, vol. 10, no. 1, pp. 399–420, 2013. DOI: [10.5194/bg-10-399-2013](https://doi.org/10.5194/bg-10-399-2013).

- [11] Z. Burkus, S. Pletcher, and J. Wheler, “Ghg emissions from oil sands tailings ponds: Overview and modelling based on fermentable substrates,” 2014.
- [12] E. E. Campbell and K. Paustian, “Current developments in soil organic matter modeling and the expansion of model applications: A review,” *Environmental Research Letters*, vol. 10, no. 12, p. 123 004, 2015. DOI: [10.1088/1748-9326/10/12/123004](https://doi.org/10.1088/1748-9326/10/12/123004).
- [13] I. Change, “Climate change 2007: The physical science basis,” *Agenda*, vol. 6, no. 07, p. 333, 2007.
- [14] R. Chen, M. Senbayram, S. Blagodatsky, *et al.*, “Soil C and N availability determine the priming effect: microbial N mining and stoichiometric decomposition theories,” *Global change biology*, vol. 20, no. 7, pp. 2356–2367, 2014.
- [15] J.-T. Cornelis and F. de Tombreur, “Soil controls on carboxylate-driven processes and opportunities,” *Plant and Soil*, vol. 476, no. 1-2, pp. 239–250, 2022. DOI: <https://doi.org/10.1007/s11104-022-05549-4>.
- [16] D. Coskun, D. T. Britto, W. Shi, and H. J. Kronzucker, “How plant root exudates shape the nitrogen cycle,” *Trends in Plant Science*, vol. 22, no. 8, pp. 661–673, 2017. DOI: <https://doi.org/10.1016/j.tplants.2017.05.004>.
- [17] J. M. Craine, C. Morrow, and N. Fierer, “Microbial nitrogen limitation increases decomposition,” *Ecology*, vol. 88, no. 8, pp. 2105–2113, 2007.
- [18] E. X. DeJesus and C. Kaufman, “Routh-hurwitz criterion in the examination of eigenvalues of a system of nonlinear ordinary differential equations,” *Physical Review A*, vol. 35, no. 12, p. 5288, 1987. DOI: <https://doi.org/10.1103/PhysRevA.35.5288>.
- [19] J. W. Doran and A. J. Jones, *Methods for assessing soil quality*. Soil Science Society of America Inc., 1997.
- [20] J. W. Doran and T. B. Parkin, “Defining and assessing soil quality,” *Defining soil quality for a sustainable environment*, vol. 35, pp. 1–21, 1994. DOI: <https://doi.org/10.2136/sssaspecpub35.c1>.
- [21] J. E. Drake, B. Darby, M.-A. Giasson, M. A. Kramer, R. P. Phillips, and A. C. Finzi, “Stoichiometry constrains microbial response to root exudation-insights from a model and a field experiment in a temperate forest,” *Biogeosciences*, vol. 10, no. 2, pp. 821–838, 2013.
- [22] R. W. Eppley, J. N. Rogers, and J. J. McCarthy, “Half-saturation constants for uptake of nitrate and ammonium by marine phytoplankton 1,” *Limnology and oceanography*, vol. 14, no. 6, pp. 912–920, 1969.
- [23] P. Falkowski, R. Scholes, E. Boyle, *et al.*, “The global carbon cycle: A test of our knowledge of earth as a system,” *science*, vol. 290, no. 5490, pp. 291–296, 2000.

- [24] P. M. Fedorak, D. L. Coy, M. J. Dudas, M. J. Simpson, A. J. Renneberg, and M. D. MacKinnon, “Microbially-mediated fugitive gas production from oil sands tailings and increased tailings densification rates,” *Journal of Environmental Engineering and Science*, vol. 2, no. 3, pp. 199–211, 2003.
- [25] P. M. Fedorak and S. E. Hrudey, “The effects of phenol and some alkyl phenolics on batch anaerobic methanogenesis,” *Water research*, vol. 18, no. 3, pp. 361–367, 1984.
- [26] A. C. Finzi, R. Z. Abramoff, K. S. Spiller, *et al.*, “Rhizosphere processes are quantitatively important components of terrestrial carbon and nutrient cycles,” *Global change biology*, vol. 21, no. 5, pp. 2082–2094, 2015. DOI: <https://doi.org/10.1111/gcb.12816>.
- [27] J. M. Foght, L. M. Gieg, and T. Siddique, “The microbiology of oil sands tailings: Past, present, future,” *FEMS Microbiology Ecology*, vol. 93, no. 5, 2017.
- [28] S. Fontaine, C. Hénault, A. Aamor, *et al.*, “Fungi mediate long term sequestration of carbon and nitrogen in soil through their priming effect,” *Soil Biology and Biochemistry*, vol. 43, no. 1, pp. 86–96, 2011.
- [29] S. Fontaine, A. Mariotti, and L. Abbadie, “The priming effect of organic matter: A question of microbial competition?” *Soil Biology and Biochemistry*, vol. 35, no. 6, pp. 837–843, 2003.
- [30] D. J. Francis, S. L. Barbour, and M. B. Lindsay, “Ebullition enhances chemical mass transport across the tailings-water interface of oil sands pit lakes,” *Journal of Contaminant Hydrology*, vol. 245, p. 103938, 2022.
- [31] A. Franzluebbers, “Soil organic matter stratification ratio as an indicator of soil quality,” *Soil and Tillage Research*, vol. 66, no. 2, pp. 95–106, 2002. DOI: [https://doi.org/10.1016/S0167-1987\(02\)00018-1](https://doi.org/10.1016/S0167-1987(02)00018-1).
- [32] T. Ge, B. Li, Z. Zhu, *et al.*, “Rice rhizodeposition and its utilization by microbial groups depends on n fertilization,” *Biology and Fertility of Soils*, vol. 53, pp. 37–48, 2017. DOI: <https://doi.org/10.1007/s00374-016-1155-z>.
- [33] T. Gentry, J. J. Fuhrmann, and D. A. Zuberer, *Principles and applications of soil microbiology*. Elsevier, 2021.
- [34] B. Griffiths and D. Robinson, “Root-induced nitrogen mineralisation: A nitrogen balance model,” *Plant Soil*, vol. 139, pp. 253–263, 1992. DOI: <https://doi.org/10.1007/BF00009317>.
- [35] C. Guo, “Rapid densification of the oil sands mature fine tailings (mft) by microbial activity,” 2009.
- [36] D. O. Hessen, G. I. Ågren, T. R. Anderson, J. J. Elser, and P. C. De Ruiter, “Carbon sequestration in ecosystems: The role of stoichiometry,” *Ecology*, vol. 85, no. 5, pp. 1179–1192, 2004.

- [37] F. M. Holowenko, M. D. MacKinnon, and P. M. Fedorak, "Methanogens and sulfate-reducing bacteria in oil sands fine tailings waste," *Canadian journal of microbiology*, vol. 46, no. 10, pp. 927–937, 2000.
- [38] I. Janssens, W. Dieleman, S. Luyssaert, *et al.*, "Reduction of forest soil respiration in response to nitrogen deposition," *Nature Geoscience*, vol. 3, no. 5, pp. 315–322, 2010.
- [39] D. Jenkinson and K. Coleman, "The turnover of organic carbon in subsoils. part 2. modelling carbon turnover," *European Journal of Soil Science*, vol. 59, no. 2, pp. 400–413, 2008. DOI: <https://doi.org/10.1111/j.1365-2389.2008.01026.x>.
- [40] D. L. Jones, A. Hodge, and Y. Kuzyakov, "Plant and mycorrhizal regulation of rhizodeposition," *New phytologist*, vol. 163, no. 3, pp. 459–480, 2004. DOI: <https://doi.org/10.1111/j.1469-8137.2004.01130.x>.
- [41] L. K. Kabwe, J. D. Scott, N. A. Beier, G. W. Wilson, and S. Jeeravipoolvarn, "Environmental implications of end pit lakes at oil sand mines in alberta, canada," *Environmental Geotechnics*, vol. 6, no. 2, pp. 67–74, 2019. DOI: [10.1680/jenge.17.00110](https://doi.org/10.1680/jenge.17.00110).
- [42] N. Kataoka, A. Miya, and K. Kiriya, "Studies on hydrogen production by continuous culture system of hydrogen-producing anaerobic bacteria," *Water Science and Technology*, vol. 36, no. 6-7, pp. 41–47, 1997.
- [43] A. B. Keller and R. P. Phillips, "Relationship between belowground carbon allocation and nitrogen uptake in saplings varies by plant mycorrhizal type," *Frontiers in Forests and Global Change*, vol. 2, p. 81, 2019. DOI: <https://doi.org/10.3389/ffgc.2019.00081>.
- [44] R. Kelly, W. Parton, G. Crocker, *et al.*, "Simulating trends in soil organic carbon in long-term experiments using the century model," *Geoderma*, vol. 81, no. 1-2, pp. 75–90, 1997. DOI: [https://doi.org/10.1016/S0016-7061\(97\)00082-7](https://doi.org/10.1016/S0016-7061(97)00082-7).
- [45] M. U. Kirschbaum and K. I. Paul, "Modelling c and n dynamics in forest soils with a modified version of the century model," *Soil Biology and Biochemistry*, vol. 34, no. 3, pp. 341–354, 2002, ISSN: 0038-0717. DOI: [https://doi.org/10.1016/S0038-0717\(01\)00189-4](https://doi.org/10.1016/S0038-0717(01)00189-4).
- [46] J. D. Kong, P. Salceanu, and H. Wang, "A stoichiometric organic matter decomposition model in a chemostat culture," *Journal of Mathematical Biology*, vol. 76, no. 3, pp. 609–644, 2018.
- [47] J. D. Kong, H. Wang, T. Siddique, *et al.*, "Second-generation stoichiometric mathematical model to predict methane emissions from oil sands tailings," *Science of the Total Environment*, vol. 694, p. 133645, 2019.

- [48] P. Kuznetsov, K. Wei, A. Kuznetsova, J. Foght, A. Ulrich, and T. Siddique, “Anaerobic microbial activity may affect development and sustainability of end-pit lakes: A laboratory study of biogeochemical aspects of oil sands mine tailings,” *ACS ES&T Water*, vol. 3, no. 4, pp. 1039–1049, 2023.
- [49] Y. Kuzyakov, “Priming effects: Interactions between living and dead organic matter,” *Soil Biology and Biochemistry*, vol. 42, no. 9, pp. 1363–1371, 2010.
- [50] Y. Kuzyakov and E. Blagodatskaya, “Microbial hotspots and hot moments in soil: Concept & review,” *Soil Biology and Biochemistry*, vol. 83, pp. 184–199, 2015. DOI: <https://doi.org/10.1016/j.soilbio.2015.01.025>.
- [51] Y. Kuzyakov, J. Friedel, and K. Stahr, “Review of mechanisms and quantification of priming effects,” *Soil Biology and Biochemistry*, vol. 32, no. 11-12, pp. 1485–1498, 2000.
- [52] R. Lal, “Sequestering atmospheric carbon dioxide,” *Critical Reviews in Plant Science*, vol. 28, no. 3, pp. 90–96, 2009.
- [53] R. Lal and R. F. Follett, *Soil carbon sequestration and the greenhouse effect*. ASA-CSSA-SSSA, 2009, vol. 57.
- [54] C. Le Quéré, M. R. Raupach, J. G. Canadell, *et al.*, “Trends in the sources and sinks of carbon dioxide,” *Nature geoscience*, vol. 2, no. 12, pp. 831–836, 2009.
- [55] R. J. Manlay, C. Feller, and M. Swift, “Historical evolution of soil organic matter concepts and their relationships with the fertility and sustainability of cropping systems,” *Agriculture, Ecosystems & Environment*, vol. 119, no. 3-4, pp. 217–233, 2007.
- [56] P. Marschner and Z. Rengel, *Nutrient cycling in terrestrial ecosystems*. Springer Science & Business Media, 2007, vol. 10.
- [57] J. P. Martin, “Decomposition and binding action of polysaccharides in soil,” *Soil Biology and Biochemistry*, vol. 3, no. 1, pp. 33–41, 1971.
- [58] S. McLaughlin, K. Zhalnina, S. Kosina, T. R. Northen, and J. Sasse, “The core metabolome and root exudation dynamics of three phylogenetically distinct plant species,” *Nature Communications*, vol. 14, no. 1, p. 1649, 2023. DOI: <https://doi.org/10.1038/s41467-023-37164-x>.
- [59] D. L. Moorhead and R. L. Sinsabaugh, “A theoretical model of litter decay and microbial interaction,” *Ecological Monographs*, vol. 76, no. 2, pp. 151–174, 2006.
- [60] D. Moreau, R. D. Bardgett, R. D. Finlay, D. L. Jones, and L. Philippot, “A plant perspective on nitrogen cycling in the rhizosphere,” *Functional Ecology*, vol. 33, no. 4, pp. 540–552, 2019. DOI: <https://doi.org/10.1111/1365-2435.13303>.
- [61] M. N. Nielsen, A. Winding, S. Binnerup, and B. Hansen, *Microorganisms as indicators of soil health*. Ministry of the Environment, National Environmental Research Institute, 2002.

- [62] S. O.L., *Soil microbiology: a model of decomposition and nutrient cycling*. CRC press, Inc., 1982.
- [63] S. Okumoto and G. Pilot, “Amino acid export in plants: A missing link in nitrogen cycling,” *Molecular plant*, vol. 4, no. 3, pp. 453–463, 2011. DOI: [10.1093/mp/ssr003](https://doi.org/10.1093/mp/ssr003).
- [64] M. Ota, H. Nagai, and J. Koarashi, “Root and dissolved organic carbon controls on subsurface soil carbon dynamics: A model approach,” *Journal of Geophysical Research: Biogeosciences*, vol. 118, no. 4, pp. 1646–1659, 2013. DOI: <https://doi.org/10.1002/2013JG002379>.
- [65] J. A. Parray, *Climate Change and Microbiome Dynamics: Carbon Cycle Feedbacks*. Springer Nature, 2023.
- [66] W. J. Parton, D. S. Schimel, C. V. Cole, and D. S. Ojima, “Analysis of factors controlling soil organic matter levels in great plains grasslands,” *Soil Science Society of America Journal*, vol. 51, no. 5, pp. 1173–1179, 1987. DOI: <https://doi.org/10.2136/sssaj1987.03615995005100050015x>.
- [67] W. J. Parton, J. W. Stewart, and C. V. Cole, “Dynamics of c, n, p and s in grassland soils: A model,” *Biogeochemistry*, vol. 5, pp. 109–131, 1988. DOI: <https://doi.org/10.1007/BF02180320>.
- [68] E. Paterson, “Importance of rhizodeposition in the coupling of plant and microbial productivity,” *European Journal of Soil Science*, vol. 54, no. 4, pp. 741–750, 2003. DOI: <https://doi.org/10.1046/j.1351-0754.2003.0557.x>.
- [69] T. J. Penner and J. M. Foght, “Mature fine tailings from oil sands processing harbour diverse methanogenic communities,” *Canadian journal of microbiology*, vol. 56, no. 6, pp. 459–470, 2010.
- [70] L. Perko, *Differential equations and dynamical systems*. Springer Science & Business Media, 2013, vol. 7.
- [71] C. E. Prescott, Y. Rui, M. F. Cotrufo, and S. J. Grayston, “Managing plant surplus carbon to generate soil organic matter in regenerative agriculture,” *Journal of Soil and Water Conservation*, vol. 76, no. 6, pp. 99A–104A, 2021. DOI: <https://doi.org/10.2489/jswc.2021.0920A>.
- [72] H. Rodhe, R. Charlson, and E. Crawford, “Svante arrhenius and the greenhouse effect,” *Ambio*, pp. 2–5, 1997.
- [73] P. L. Salceanu, “Robust uniform persistence in discrete and continuous dynamical systems using lyapunov exponents,” *Mathematical Biosciences and Engineering*, vol. 8, no. 3, pp. 807–825, 2011. DOI: [10.3934/mbe.2011.8.807](https://doi.org/10.3934/mbe.2011.8.807)[PreviousArticleNextArticle](#).

- [74] M. F. M. Shahimin, J. M. Foght, and T. Siddique, “Preferential methanogenic biodegradation of short-chain n-alkanes by microbial communities from two different oil sands tailings ponds,” *Science of the Total Environment*, vol. 553, pp. 250–257, 2016.
- [75] T. Siddique, P. M. Fedorak, and J. M. Foght, “Biodegradation of short-chain n-alkanes in oil sands tailings under methanogenic conditions,” *Environmental science & technology*, vol. 40, no. 17, pp. 5459–5464, 2006.
- [76] T. Siddique, P. M. Fedorak, M. D. MacKinnon, and J. M. Foght, “Metabolism of btex and naphtha compounds to methane in oil sands tailings,” *Environmental science & technology*, vol. 41, no. 7, pp. 2350–2356, 2007.
- [77] T. Siddique, R. Gupta, P. M. Fedorak, M. D. MacKinnon, and J. M. Foght, “A first approximation kinetic model to predict methane generation from an oil sands tailings settling basin,” *Chemosphere*, vol. 72, no. 10, pp. 1573–1580, 2008.
- [78] T. Siddique, M. F. Mohamad Shahimin, S. Zamir, K. Semple, C. Li, and J. M. Foght, “Long-term incubation reveals methanogenic biodegradation of c5 and c6 iso-alkanes in oil sands tailings,” *Environmental science & technology*, vol. 49, no. 24, pp. 14 732–14 739, 2015.
- [79] T. Siddique, T. Penner, J. Klassen, C. Nesbo, and J. M. Foght, “Microbial communities involved in methane production from hydrocarbons in oil sands tailings,” *Environmental science & technology*, vol. 46, no. 17, pp. 9802–9810, 2012.
- [80] T. Siddique, K. Semple, C. Li, and J. M. Foght, “Methanogenic biodegradation of iso-alkanes and cycloalkanes during long-term incubation with oil sands tailings,” *Environmental pollution*, vol. 258, p. 113 768, 2020.
- [81] T. Siddique, S. Stasik, M. Mohamad Shahimin, and K. Wendt-Potthoff, “Microbial communities in oil sands tailings: Their implications in biogeochemical processes and tailings management,” *Microbial Communities Utilizing Hydrocarbons and Lipids: Members, Metagenomics and Ecophysiology*. Springer International Publishing, pp. 1–33, 2018.
- [82] D. R. Smart and A. J. Bloom, “Kinetics of ammonium and nitrate uptake among wild and cultivated tomatoes,” *Oecologia*, vol. 76, pp. 336–340, 1988. DOI: <https://doi.org/10.1007/BF00377026>.
- [83] R. W. Sterner and J. J. Elser, *Ecological stoichiometry*. Princeton University Press, 2017.
- [84] D. Stott, “Recommended soil health indicators and associated laboratory procedures,” *Soil Health Technical Note*, no. 450-03, 2019.
- [85] G. Stotzky, *Soil Biochemistry* (Books in Soils, Plants, and the Environment). CRC Press, 200, 2000, ISBN: 9780824788346. [Online]. Available: <https://books.google.ca/books?id=VI9N7b16CRoC>.

- [86] J. M. Suffita, J. A. Robinson, and J. M. Tiedje, “Kinetics of microbial dehalogenation of haloaromatic substrates in methanogenic environments,” *Applied and Environmental Microbiology*, vol. 45, no. 5, pp. 1466–1473, 1983.
- [87] H. Sun, S. Jiang, C. Jiang, C. Wu, M. Gao, and Q. Wang, “A review of root exudates and rhizosphere microbiome for crop production,” *Environmental Science and Pollution Research*, vol. 28, pp. 54 497–54 510, 2021. DOI: <https://doi.org/10.1007/s11356-021-15838-7>.
- [88] W. Sun, B. Ji, S. A. Khoso, *et al.*, “An extensive review on restoration technologies for mining tailings,” *Environmental Science and Pollution Research*, vol. 25, pp. 33 911–33 925, 2018.
- [89] D. M. Sylvia, J. J. Fuhrmann, P. G. Hartel, and D. A. Zuberer, *Principles and Applications of Soil Microbiology*. Pearson, 2005, ISBN: 0130941174.
- [90] A. Taghizadeh-Toosi, B. T. Christensen, N. J. Hutchings, *et al.*, “C-tool: A simple model for simulating whole-profile carbon storage in temperate agricultural soils,” *Ecological Modelling*, vol. 292, pp. 11–25, 2014, ISSN: 0304-3800. DOI: <https://doi.org/10.1016/j.ecolmodel.2014.08.016>.
- [91] B. Tan, X. Dong, C. W. Sensen, and J. Foght, “Metagenomic analysis of an anaerobic alkane-degrading microbial culture: Potential hydrocarbon-activating pathways and inferred roles of community members,” *Genome*, vol. 56, no. 10, pp. 599–611, 2013.
- [92] B. Tan, K. Semple, and J. Foght, “Anaerobic alkane biodegradation by cultures enriched from oil sands tailings ponds involves multiple species capable of fumarate addition,” *FEMS Microbiology Ecology*, vol. 91, no. 5, fiv042, 2015.
- [93] R. L. Tate, “Soil microbiology,” *Wiley, New York*, 1995.
- [94] E. Tedford, G. Halferdahl, R. Pieters, and G. A. Lawrence, “Temporal variations in turbidity in an oil sands pit lake,” *Environmental Fluid Mechanics*, vol. 19, pp. 457–473, 2019.
- [95] M. Toal, C. Yeomans, K. Killham, and A. Meharg, “A review of rhizosphere carbon flow modelling,” *Plant and soil*, vol. 222, no. 1-2, pp. 263–281, 2000. DOI: <https://doi.org/10.1023/A:1004736021965>.
- [96] P. Venegas Garcia and H. Wang, “A data-validated stoichiometric model for the priming effect,” *Bulletin of Mathematical Biology*, vol. 85, no. 6, p. 53, 2023. DOI: <https://doi.org/10.1007/s11538-023-01160-5>.
- [97] H. Wang, L. Jiang, and J. S. Weitz, “Bacterivorous grazers facilitate organic matter decomposition: A stoichiometric modeling approach,” *FEMS microbiology ecology*, vol. 69, no. 2, pp. 170–179, 2009.
- [98] H. Wang, Z. Lu, and A. Raghavan, “Weak dynamical threshold for the “strict homeostasis” assumption in ecological stoichiometry,” *Ecological Modelling*, vol. 384, pp. 233–240, 2018.

- [99] H. Wang, R. W. Sterner, and J. J. Elser, “On the “strict homeostasis” assumption in ecological stoichiometry,” *Ecological Modelling*, vol. 243, pp. 81–88, 2012.
- [100] W. A. Wurtsbaugh, H. W. Paerl, and W. K. Dodds, “Nutrients, eutrophication and harmful algal blooms along the freshwater to marine continuum,” *Wiley Interdisciplinary Reviews: Water*, vol. 6, no. 5, e1373, 2019. DOI: <https://doi.org/10.1002/wat2.1373>.